Wireless Networks

Xilin Cheng
Liuqing Yang
Xiang Cheng

Cooperative OFDM Underwater Acoustic Communications

Springer

Wireless Networks

Series Editor:
Xuemin (Sherman) Shen
University of Waterloo, Waterloo, Ontario, Canada

More information about this series at http://www.springer.com/series/14180

Xilin Cheng • Liuqing Yang • Xiang Cheng

Cooperative OFDM Underwater Acoustic Communications

Springer

Xilin Cheng
Electrical and Computer Engineering
Colorado State University
Fort Collins, CO, USA

Liuqing Yang
Electrical and Computer Engineering
Colorado State University
Fort Collins, CO, USA

Xiang Cheng
School of Electronics Engineering
Peking University
Beijing, China

ISSN 2366-1186 ISSN 2366-1445 (electronic)
Wireless Networks
ISBN 978-3-319-33206-2 ISBN 978-3-319-33207-9 (eBook)
DOI 10.1007/978-3-319-33207-9

Library of Congress Control Number: 2016939985

Printed on acid-free paper

This Springer imprint is published by Springer Nature
The registered company is Springer International Publishing AG Switzerland

Preface

The Earth is a blue planet. Approximately 71 % of the Earth's surface is covered by ocean, which corresponds to an area of 361 million km^2 and a volume of 1.3 billion km^3. Most of this vastness is unexplored and remains a mystery. To explore the intriguing world undersea, the need for robust and reliable underwater wireless networks is rapidly growing. Among the various means of communications, underwater acoustic communications (UAC) is widely considered as the most feasible option at reasonable distances. The earliest UAC arises from the military need. During World War II, UAC is used for communications among submarines, and the analog single-sideband suppressed-carrier amplitude modulation is adopted. In the 1980s, the noncoherent frequency shift keying (FSK) digital modulation is widely used. However, FSK has very low data rate. In the 1990s, to achieve higher data rate, UAC research is gradually shifted to the phase-coherent communications with high receiver complexity to handle the large delay spread of underwater acoustic (UWA) channels. Over the last decade, the advance of UAC includes the implementation of the multiple-input and multiple-output (MIMO) communications which can improve the data rate and the reliability of UAC and orthogonal frequency-division multiplexing (OFDM) communications due to its low receiver complexity, capability of inter-symbol interference (ISI) removal, and robustness against large delay spread. This monograph focuses on another promising technique for the future UAC, namely, cooperative communications with the benefits of improving the transmission reliability and distances. With OFDM adopted as the physical layer transmission technique, many different aspects of cooperative UAC are covered by this monograph such as power allocation, decomposed LT (DLT) codes design, and packet transmission reliability.

The chapters of this monograph are relatively independent with each other. The readers can go directly to the chapter(s) of interest. The monograph starts with the motivation and the literature review of cooperative OFDM UAC in Chap. 1. The UWA channel modeling is introduced in Chap. 2. The adaptive system design including optimal power allocation and distribution for the short-range relay-aided (RA-)UAC is studied in Chap. 3. The medium-long-range asynchronous relay selection protocol is investigated in Chap. 4. The energy-efficient hybrid (h-)DLT

codes design for RA-UAC is presented in Chap. 5, and this chapter also includes a statistical polynomial decomposition algorithm to facilitate the h-DLT codes decomposition. The effective mirror-mapping-based ICI cancellation for OFDM transmission in RA-UAC is provided in Chap. 6.

This monograph is designed for professionals and researchers in the field of UAC. Advanced-level students in electrical engineering or computer science will also find this monograph useful.

We would like to thank Dr. Rui Cao, Dr. Fengzhong Qu, Dr. Miaowen Wen, and Dr. Dongliang Duan for their much help in the research. We also want to express our thanks to Dr. Mahmood R Azimi-Sadjadi, Dr. J. Rockey Luo, and Dr. Haonan Wang for their valuable insights and comments. Finally, we would like to thank the continued support from the National Science Foundation.

Fort Collins, CO, USA — Xilin Cheng
Fort Collins, CO, USA — Liuqing Yang
Beijing, China — Xiang Cheng

Contents

1 Introduction 1
1.1 Underwater Acoustic Communications and Its Challenges 1
1.2 Cooperative OFDM Communications over UWA Channels 2
1.2.1 Power Allocation of Short-Range RA-UAC 3
1.2.2 Power Allocation of Medium-Long-Range RA-UAC 5
1.2.3 Decomposed Fountain Codes Design for RA-UAC 6
1.2.4 Reliable OFDM Transmission in RA-UAC 8
1.3 Organization of the Monograph 9
References 10

2 Underwater Acoustic Channel Models 13
2.1 Empirical UWA Channel Model 13
2.2 Statistical Time-Varying UWA Channel Model 14
2.3 Relationship Between Coherence Time and Transmission Distances 15
References 15

3 Short-Range Adaptive RA-UAC 17
3.1 System Model 17
3.2 Optimal Power Allocation 19
3.3 Channel Prediction 24
3.3.1 Problem Statement 24
3.3.2 MSE Analysis 25
3.3.3 Prediction Advance Factor 27
3.3.4 RLS Algorithm 27
3.4 Channel Quantization 28
3.5 Performance Evaluations 28
3.5.1 Capacity Analysis for Empirical UWA Channel Model 29
3.5.2 Capacity Analysis for Statistical Time-Varying UWA Channel Model 32

3.6 Summary 37
References 38

4 Medium-Long-Range Asynchronous Relay Selection Protocol for RA-UAC 39
4.1 AsAP Protocol 39
4.1.1 Source Transmitting 39
4.1.2 Relay Amplifying and Forwarding 41
4.1.3 Destination Decoding 41
4.2 Power Allocation Based on Statistical CSI 43
4.3 SR-AsAP Protocol 47
4.3.1 Protocol Description 47
4.3.2 Asynchronous Transmission Design 48
4.3.3 Efficiency Analysis 50
4.4 Performance Evaluations 52
4.5 Summary 53
References 55

5 Energy-Efficient Hybrid Decomposed LT Codes for RA-UAC 57
5.1 Background 57
5.1.1 LT Codes 57
5.1.2 DLT Codes 58
5.1.3 Stochastic Optimization Methods 59
5.2 Nonnegative Polynomial Decomposition Algorithm 60
5.2.1 Projected Gradient Method 61
5.2.2 Multistart Method 65
5.2.3 Nonnegative Polynomial Decomposition Results 66
5.3 h-DLT Codes 69
5.3.1 h-DLT I Codes 69
5.3.2 h-DLT II Codes 70
5.3.3 Distribution Decomposition for h-DLT II Codes 71
5.3.4 h-DLT II Codes Performance 72
5.4 h-DLT II Codes Assisted Cooperative Communications Protocol 73
5.5 Performance Evaluations 75
5.5.1 h-DLT Codes Comparison and Choice of Storage Schemes 75
5.5.2 Effect of Mode Ratio 76
5.5.3 Effect of Relay Number 77
5.6 Summary 79
References 79

6 Effective ICI Cancellation for OFDM Transmission in RA-UAC 81
6.1 Properties of ICI Coefficients 81
6.2 Proposed ICI Cancellation Schemes 83
6.2.1 ICI Self-Cancellation with Mirror-Mapping 83
6.2.2 ICI Two-Path Cancellation with Mirror-Mapping 84

6.3 CIR Evaluation 86
6.3.1 Plain OFDM 86
6.3.2 MSR 86
6.3.3 MCSR 89
6.3.4 MCVT 91
6.3.5 MCJT 93
6.3.6 CIR Comparison 95
6.4 Sea Experimental Results 96
6.4.1 Experimental Settings 98
6.4.2 Time Synchronization and Resampling 100
6.4.3 Channel Estimation 100
6.4.4 Experimental Results 100
6.5 Summary 101
References 102

7 Conclusions and Future Directions 103
7.1 Conclusions 103
7.2 Future Directions 104

Acronyms

ACK	Acknowledgment
ACSR	Adjacent conjugate symbol repetition
AF	Amplify-and-forward
AsAP	Asynchronous AF relaying with precoded OFDM
ASR	Adjacent symbol repetition
AWGN	Additive white Gaussian noise
BEM	Basis expansion model
BER	Bit error rate
BP	Belief propagation
BPSK	Binary phase shift keying
CFO	Carrier frequency offset
CFR	Channel frequency response
CIR	Carrier-to-interference power ratio
CP	Cyclic prefix
CSI	Channel state information
DDP	Degree distribution polynomial
DF	Decode-and-forward
DFT	Discrete Fourier transform
DL	Direct-link
DLT	Decomposed Luby transform
FD	Frequency domain
FEC	Forward error correction
FFT	Fast Fourier transform
GLCP	Grouped linear constellation precoding
h-DLT	Hybrid decomposed LT
ICI	Intercarrier interference
IFFT	Inverse fast Fourier transform
ISD	Ideal Soliton distribution
ISI	Inter-symbol interference
KKT	Karush-Kuhn-Tucker
LT	Luby transform

MCJT	Mirror conjugate transmission
MCSR	Mirror conjugate symbol repetition
MCVT	Mirror conversion transmission
MRC	Maximum ratio combining
MSE	Mean square error
MSR	Mirror symbol repetition
OFDM	Orthogonal frequency-division multiplexing
RA-UAC	Relay-aided UAC
RF	Radio-frequency
RL	Relay-link
RLS	Recursive least squares
RMS	Root mean square
RSD	Robust Soliton distribution
SNR	Signal-to-noise ratio
SR-AsAP	AsAP protocol with selective relaying
TD	Time domain
TDM	Time division multiplexing
TDMA	Time division multiple access
UAC	Underwater acoustic communications
UWA	Underwater acoustic
UWASN	Underwater acoustic sensor networks
WF	Water-filling

Chapter 1
Introduction

Underwater acoustic sensor networks (UWASN) have been attracting growing research interests in recent decades due to the emerging applications [1, 2]. For the environmental monitoring purpose, UWASN can perform real-time pollution monitoring of streams, lakes, ocean bays, drinking water reservoirs, local ponds, etc. For the undersea and offshore oil exploration, UWASN can perform oil leakage detection, equipment monitoring, and seismic imaging. For the military application, UWASN can be used for tactical target identification and intrusion detection. In addition, UWASN can help understand biological behaviors under different water conditions. To realize UWASN, underwater acoustic communications (UAC) is one of the key communication techniques. In this chapter, we first briefly review UAC and its challenges. Then, cooperative orthogonal frequency-division multiplexing (OFDM) communications is introduced to address these challenges, and we focus on the design of the dual-hop relay-aided (RA-)UAC from three aspects, namely, power allocation, decomposed fountain codes design, and packet transmission reliability. Finally, the organization of this monograph is given at the end of this chapter.

1.1 Underwater Acoustic Communications and Its Challenges

Due to the difficulty and high cost of underwater cable deployment and the necessity of sparse network topology to monitor a massive area of ocean, wireless communications is preferable for sensor communications. Among all available wireless media, the radio-frequency (RF) waves used in terrestrial wireless communications can only propagate about several meters underwater, and the optical waves can only support underwater communications around tens of meters. In contrast, the

X. Cheng et al., *Cooperative OFDM Underwater Acoustic Communications*,
Wireless Networks, DOI 10.1007/978-3-319-33207-9_1

underwater acoustic (UWA) signals can propagate over several kilometers. This makes acoustic waves more attractive than other information carriers. Thus, UAC is one of the key communication techniques to realize UWASN.

The particular features of acoustic signal propagation and underwater environments bring formidable challenges to UAC. First, the acoustic signal is characterized by low carrier frequency and distance-dependent bandwidth. This significantly limits the capacity and increases the transmit power of UAC, especially at long transmission distances [3]. Secondly, the large delay spread resulting from the multipath nature of UWA channels causes frequency-selective fading and inter-symbol interference (ISI). Thirdly, as the propagation of UWA waves is very slow ($c \approx 1500$ m/s), the propagation delay is much longer than that of RF waves. In addition, the environmental factors such as ocean waves, water temperature, salinity, etc. induce high delay variance. Long and variant delay can hamper effective channel state information (CSI) feedback, accurate time synchronization, and well-coordinated medium access [4, 5]. Finally, large Doppler shifts caused by motion and ocean waves lead to error-prone fast time-varying UWA channels [6]. Therefore, the transmission and networking protocols designed for RF systems cannot be directly applied to UAC systems, and the redesign of UAC protocols needs to achieve reliable and energy-efficient data transmissions.

1.2 Cooperative OFDM Communications over UWA Channels

Cooperative relay communications can reduce power consumption and extend transmission distances by dividing a long transmission link into short links with much lower signal attenuation [7, 8]. Therefore, it is promising to design future UAC [9]. In literatures, there have been several research articles about its applications in UAC. In [5], the time-reversal distributed space-time block coding scheme is proposed. In [10, 11], the decode-and-forward (DF) relaying schemes are investigated. All of [5, 10, 11] validate the benefits of relay-aided system over the single-hop system. Other topics about RA-UAC include two-way relaying, and relay position and frequency optimization. In [12], the two-way relaying is considered, and the information of two sources is exchanged via a relay. The decoding algorithm at the relay is investigated through a sea trial. In [13], the relay position and the carrier frequency are jointly optimized for a multi-hop line network to improve the energy efficiency of UWASN.

In this monograph, we consider dual-hop RA-UAC and different approaches to improve its energy efficiency and reliability. OFDM is adopted as the physical-layer transmission technique due to its capability of ISI removal and robustness against large delay spread.

First, we investigate the power allocation of dual-hop relay communications, i.e., the transmit power at the source and the relay is allocated according to CSI, to

improve the system reliability or reduce the total transmission power consumption without sacrificing the overall system performance. Two transmission scenarios are considered. The first scenario we examine is the short-range communications (< 1 km). For the short-range RA-UAC, the direct-link (DL) signal is usually strong. The need of cooperative communications arises when the source cannot directly communicate with the destination due to the blocking between them, and the relay is utilized to assist communications between the source and the destination. For this scenario, an adaptive system is developed based on instantaneous CSI in Chap. 3. The second scenario we examine is the medium-long-range communications ($\gg 1$ km). For the medium-long-range RA-UAC, there could be multiple potential relays between the source and the destination, and the weak DL strength motivates the utilization of RA-UAC. For this scenario, a selective relaying protocol is designed based on statistical CSI in Chap. 4.

Secondly, we focus on the energy-efficient decomposed fountain codes design for dual-hop RA-UAC. Forward error correction (FEC) codes are commonly adopted in dual-hop relay communications, among which Luby Transform (LT) codes are favorable because of their low-complexity decoder and rate adaptability to erasure channels. Moreover, as LT codes require no or few acknowledgments (ACK) from the receiver, LT codes can reduce the end-to-end transmission latency substantially considering the slow propagation speed of the UWA signals. To alleviate the high computational cost in the primitive LT-based cooperative communications, hybrid decomposed LT (h-DLT) codes are proposed recently [14]. By dispersing the computational cost of LT codes into the source and the relay, the computational cost of both nodes can be reduced considerably. However, there are some practical limitations. First, the nonnegative decomposition algorithm developed for h-DLT codes construction has no control of decomposition accuracy. Secondly, the cooperative relay communications protocol based on the original h-DLT codes can induce high communication cost. Therefore, we present a novel stochastic nonnegative polynomial decomposition algorithm which achieves simpler implementation and higher decomposition accuracy for h-DLT codes construction in Chap. 5. Based on the new algorithm, a new type of h-DLT codes is proposed for cooperative relay communications to enable reliable communications with higher energy efficiency.

Finally, OFDM communications in UWA channels suffers from intercarrier interference (ICI) caused by the Doppler effect. To improve the reliability of packet transmission in RA-UAC, we propose four low-complexity effective mirror-mapping-based ICI cancellation schemes without explicitly estimating ICI coefficients or carrier frequency offset (CFO) in Chap. 6.

Our designs about power allocation, decomposed fountain codes, and reliable packet transmission in dual-hop RA-UAC are detailed in the following.

1.2.1 Power Allocation of Short-Range RA-UAC

In terrestrial radio channels, the adaptive power allocation has been investigated in [15, 16]. However, the unique characteristics of UWA channels hinder the direct implementation of the adaptive power allocation techniques. First, UWA channels

are fast time-varying due to large Doppler shifts, and the channel impulse response could totally change during the feedback signal propagation. This differs from the prevailing quasi-static channel assumption in terrestrial radio channels. Secondly, UWA channels have very limited bandwidth. Therefore, the full CSI transmission and exchange are impractical, e.g., it is not reasonable to assume the destination has full CSI of the source-to-relay (S-R) channel. In literatures, there are preliminary results reporting the adaptive power allocation in RA-UAC [17, 18]. However, none of them properly address the two issues above.

To overcome the adverse effect brought by UWA channels, we investigate the adaptive power allocation and propose an adaptive RA-UAC system tailored for UWA channels in Chap. 3. The amplify-and-forward (AF) mode is chosen at the relay for simplicity. First, with individual and total power constraints, we study the optimal power allocation between the source and the relay as well as the power distribution over all subcarriers for AF relaying. The Karush-Kuhn-Tucker (KKT) conditions are utilized to solve the power optimization problem, and the optimality of the derived solution is validated. Theoretical analysis reveals that the optimal power allocation ratio at a subcarrier is proportional to the reciprocal of the channel gain ratio, and numerical results confirm that RA-UAC with the optimal power allocation has better performance than RA-UAC with the uniform power allocation. It is also found that the individual power constraints restrict the power allocation for the unbalanced links. Secondly, we implement channel prediction to compensate the channel variation during the CSI signal propagation. To combat the channel variation during the feedback signal propagation, Doppler shifts are estimated and compensated at the relay and the destination to convert the fast time-varying UWA channels to the slow time-varying UWA channels, and the standard recursive least squares (RLS) adaptive filter is utilized to predict the future channel impulse response [19–22]. The effect of the channel estimation error is considered, and the mean square error (MSE) of the RLS adaptive filter under the wide-sense stationary channel assumption is derived. It is demonstrated that the MSE with channel prediction is smaller than the MSE without channel prediction. Moreover, it is found that the performance of the adaptive RA-UAC system without channel prediction degrades a lot compared with the theoretical performance of the optimal power allocation, and the adaptive RA-UAC system with channel prediction does improve the performance substantially. Finally, we design a practical adaptive RA-UAC system. In the system, the relay and the destination predict the future channel impulse response, and the channel impulse response is quantized into a few bits efficiently using the Lloyd algorithm to adapt to the band-limited UWA channels [23]. After receiving quantized CSI, the source and the relay calculate their power allocation and transmit OFDM symbols accordingly. In addition, it is demonstrated that the proposed adaptive power allocation scheme is more suitable for shorter transmission distances as the channel impulse responses are predictable. It is worth noticing that the design methodology can be directly applied to other adaptive UAC systems such as DF relaying.

1.2.2 Power Allocation of Medium-Long-Range RA-UAC

Different from the short-range RA-UAC, the long propagation delay in medium-long range RA-UAC could nullify the instantaneous CSI feedback even if the Doppler compensation is implemented at the receiver side. Thus, we assume transmitter-side instantaneous CSI is not available, and statistical CSI is utilized when calculating the power allocation of medium-long-range RA-UAC [24].

Our focus of medium-long-range RA-UAC is the protocol design. In [8], a RA-UAC protocol, i.e., asynchronous AF relaying with precoded OFDM (AsAP), is designed to combat time asynchronism and achieve reliable data communications. In this scheme, the asynchronous AF relaying solves the time synchronization difficulty and facilitates relay processing. All relays amplify and forward the received signal to the destination asynchronously without any time coordination. Additionally, precoded OFDM resolves the frequency selectivity issue of UWA channels. However, there are still two design factors in the original AsAP protocol that can degrade the system performance. First, fixed amplification is adopted at the relays, and the transmit power is uniformly allocated among the source and the relays. Although this simplifies the system implementation, the end-to-end system performance is constrained. Secondly, the processing delay at the relays is not considered. As there will be at least one OFDM symbol processing delay at the relays for the frequency domain (FD) amplification, the DL signal could cause serious interference toward the relay-link (RL) signals.

To overcome the two issues of the original AsAP protocol, we redesign the AsAP protocol for medium-long-range UAC in this monograph in Chap. 4. Different from the original AsAP protocol, adaptive amplification based on instantaneous S-R CSI in the FD is adopted, and the DL and RL signals are combined using maximum ratio combining (MRC) to collect delay diversity. The transmit power allocation of the AsAP protocol is investigated based on statistical CSI. Analytical results suggest only the relay with the maximum effective signal-to-noise ratio (SNR) transmits while other relays keep silent. This corresponds to the selective relaying scheme based on statistical CSI. According to this observation, we propose an AsAP protocol with selective relaying (SR-AsAP). Different from the traditional relay selection protocol, the SR-AsAP protocol selects the relay which has the best channel condition statistically, and the selected relay keeps on transmission, similar to the single relay system. In addition, to avoid interference between the DL signal and the RL signal, we design a new asynchronous transmission scheme for the SR-AsAP protocol, where the source first transmits a batch of OFDM symbols to the relay with a preamble and a postamble attached to facilitate the relay determining the starting and ending points of the received OFDM symbols, and then the received OFDM symbols at the relay are amplified and forwarded to the destination. In this way, the DL and RL signals are separated naturally in the time domain (TD). Analytical and simulation results reveal that the transmission efficiency of the SR-AsAP protocol could reach $1/2$. To verify the benefits of the SR-AsAP protocol, we simulate the error performance and compare it with the DL system and the AsAP

protocol with all relay transmissions. Simulation results show that the proposed SR-AsAP protocol outperforms the DL system and the AsAP protocol with all relay transmissions.

1.2.3 Decomposed Fountain Codes Design for RA-UAC

Because of the error-prone transmissions and the long propagation delay in UWA channels, fountain codes which are rate adaptable to erasure channels and require no or few ACKs are very attractive for UAC.

In the literatures, fountain codes are proposed to improve the communication reliability and reduce the end-to-end latency of dual-hop relay communications. In [25–27], independent fountain encoding is adopted at each hop to ensure the dual-hop transmission reliability. As the relays need to decode and re-encode each received packet, high computational cost is incurred at the relays. To address this issue, concatenated encoding is adopted in [28–31], where the relays simply apply a second-layer encoding to the fountain-coded data from the source without decoding. However, this can give rise to significant decoding complexity at the destination. In order to reduce the computational cost while retaining the communication reliability on both links, the concept of decomposed fountain codes has been proposed. Typically, the decomposed fountain codes consist of two-layer data encoding which can be performed collaboratively by the source and the relays. The first Decomposed Luby Transform (DLT) code is proposed in [32], which is a special case of DLT codes with the second-layer encoding degree fixed to 2 or 4. Analyses in [33] show that the asymptotic performance of DLT codes with two-layer random encoding is the same as that of the non-decomposed LT codes.

The key challenge of the DLT codes is the codes degree distribution design, i.e., how to decompose the degree distribution polynomial (DDP) of LT codes $\mu(x)$ into one DDP for the source encoder $\theta(x)$ and one DDP for the relay encoder $\omega(x)$, such that $\omega(\theta(x))$ resembles $\mu(x)$. Nonnegative polynomial decomposition is very challenging. In the literature, existing research has revealed that exact decomposition does not always exist for arbitrary degree orders [34]. The approximate polynomial decomposition algorithms could not guarantee nonnegative decomposition solutions and optimality [35]. In [32], the first nonnegative decomposition algorithm of DLT codes is proposed, where a smooth portion of Robust Soliton distribution (RSD) is decomposed using the deconvolution method and selective combination of the source packets is adopted at the relay such that the generated packets follow the RSD. However, the decomposition algorithm is designed only for the relay encoder with DDP $\omega(x) = \sum_{i=1}^{N} \omega_i x^i$, $N = 2$ or 4. In addition, the deconvolution method does not utilize high-order target DDP information, which could result in the decomposition with poor match at the high-order terms and the sum of the generated probability distribution over all degrees less than 1. In [33], the decomposition problem is simplified to find $\omega(x)$ only, which can be optimized through simple linear programming. However, $\theta(x)$ has to be a priori known.

To enable more general codes decomposition, in [14], h-DLT codes are studied with the merits of flexible computational cost allocation between the source and relay encoders. The h-DLT codes conduct the data encoding in two modes: one-layer direct LT mode and two-layer cooperative DLT mode. In the direct LT mode, the packets are generated only by the first encoder and directly forwarded to the destination once selected at the relay encoder; while in the cooperative DLT mode, each packet is encoded by both encoders. By adjusting the mode ratio, the h-DLT codes can control the encoding cost allocation between the source and relay encoders. Through two-layer encoding at the source and the relay, the received packet at the destination follows the exact DDP as the RSD, which renders the low-complexity decoding. However, the original h-DLT codes proposed in [14] have some limitations in practical implementation. First, the codes decomposition algorithm, namely, the nonnegative-range method, has no control of decomposition accuracy, and valid decomposition is not always guaranteed. Secondly, the cooperative relay communications scheme based on this h-DLT code is energy inefficient. The second-layer DDP of the original h-DLT codes has high average encoding degree. Thus, a large number of packets need to be sent from the source to assure sufficient amount of packets for the destination decoding. This induces high communication cost.

In this monograph, we design a new type of h-DLT codes for cooperative relay communications with improved energy efficiency and accuracy in Chap. 5. First, we propose a novel and general stochastic nonnegative polynomial decomposition algorithm. The proposed decomposition algorithm consists two phases to minimize the fitting error of the resultant DDP and the target DDP. The projected gradient method in the first phase aims at locating the stationary point from a given initial point, while the multistart method searches all the stationary points by means of implementing the projected gradient method at randomly selected initial points. Through the two phases, the new algorithm minimizes the decomposition error and can always obtain a valid decomposition result. Numerical results confirm that the proposed nonnegative polynomial decomposition algorithm can achieve higher decomposition accuracy compared with the nonnegative-range method [14]. Secondly, with this new algorithm, we propose a more efficient h-DLT codes [36] for cooperative relay communications. The new h-DLT codes tend to assign the DDP with lower average encoding degree to the relay encoder. This means that the packets needed from the source will be largely reduced. Thus, the communication cost can be lowered considerably. For presentation clarity, we name the original h-DLT codes in [14] as h-DLT I codes and the newly proposed h-DLT codes as h-DLT II codes. The performance of h-DLT II codes is simulated and compared with the primitive LT code and DLT codes. Then, the efficiency of the h-DLT II codes assisted cooperative communications protocol is evaluated in terms of the average number of transmissions per packet, and the benefits of h-DLT II codes assisted cooperative relay systems are illustrated through comparison with h-DLT I codes assisted cooperative relay systems. Finally, the effects of several system and design parameters are also revealed including the storage schemes and size at the relays, the hybrid mode ratio, and the number of relays.

1.2.4 Reliable OFDM Transmission in RA-UAC

OFDM has recently attracted great interests from researchers in the field of UAC due to its capability of combating ISI caused by large delay spread [37–51]. The key principle of OFDM is that the wideband time-invariant channel is converted into multiple orthogonal flat fading sub-channels, and modulated symbols transmitted over different subcarriers do not interfere with each other. However, for UWA channels, the Doppler effect is usually very severe due to the transmitter/receiver motion and ocean waves, which result in rapidly time-varying behaviors. The time-varying features of UWA channels would then destroy the orthogonality among subcarriers and lead to ICI. To ensure reliable packet transmissions in UWA channels, ICI has to be suppressed to an acceptable level.

In the literature, there are mainly three categories of ICI suppression methods. In the first category, the basis expansion model (BEM) has been considered for ICI mitigation in some work [46–48]. However, the BEM coefficient estimation introduces additional computational burden at the receiver. In the second category, the ICI is treated explicitly by first estimating the ICI coefficients followed by various ICI cancellation algorithms (see, e.g., [37, 38, 52–54]). This strategy is robust against wide Doppler spread. However, it usually requires significant modifications on the traditional OFDM transceiver and greatly increases the complexity. Therefore, in the third category, another low-complexity strategy is taken to treat ICI implicitly. In [39–45], it is believed that ICI can be eliminated by received data resampling and Doppler shift compensation. These receivers do not need to estimate the ICI coefficients and thus facilitate low-complexity channel estimation and symbol detection. However, additional null subcarrier overhead, exhaustive search, and/or iterative operations are often involved. In [55], the adjacent-mapping-based ICI cancellation method is proposed. Each data symbol is transmitted in two adjacent subcarriers. Depending on the conversion or the conjugate relation between adjacent subcarrier pairs carrying the same information, there are the adjacent symbol repetition (ASR) scheme and the adjacent conjugate symbol repetition (ACSR) scheme. These schemes can implicitly cancel ICI by combining received signals on adjacent subcarrier pairs. However, for both schemes, ICI has not been sufficiently suppressed, and there still exists residual interference from neighbor subcarriers.

In Chap. 6, we also adopt the rationale of the third category and attempt to bypass the ICI coefficient estimation during the ICI cancellation process. Inspecting the ICI coefficients of the plain OFDM systems, we find that for any particular subcarrier, there is a very interesting relationship between the interference from mirrored subcarrier around. Based on this observation, we exploit data repetition within OFDM symbols according to some carefully designed subcarrier mapping rules and operations such that after combining the subcarrier pairs carrying the same information, the carrier-to-interference power ratio (CIR) can be significantly improved. The resultant ICI cancellation schemes feature the simplicity of implementation and the effectiveness of ICI mitigation.

There are two options to implement data repetition and the desired mirror-mapping operation. One is a self-cancellation approach, where the data is repeated within one OFDM symbol by mirror-mapping, and the other one is a general two-path cancellation approach, where the data is repeated across two consecutive OFDM symbols. Compared with the self-cancellation approach, the latter one is conveniently compatible with the traditional OFDM transceiver design without any modifications. Detailed comparisons are made analytically and by numerical results and experiments. After data repetition, due to the property of the ICI coefficients, one also has two options to process the mirror-mapped data, including the conversion and conjugate operations. Combining all these options, we have four schemes in total, namely, the mirror symbol repetition (MSR) scheme, the mirror conjugate symbol repetition (MCSR) scheme, the mirror conversion transmission (MCVT) scheme, and the mirror conjugate transmission (MCJT) scheme [56–58]. For comparison purposes, we derive closed-form expressions of their CIRs. The CIR analyses and numerical results show that significant ICI cancellation can be achieved compared with the plain OFDM and the adjacent-mapping-based schemes, and the CIR expression for flat fading channels is identical to that for additive white Gaussian noise (AWGN) channels. Furthermore, we find the underlying relationship between the two options to implement the data repetition, namely, the self-cancellation schemes and the two-path cancellation schemes. In addition, the effects of channel length and CFO deviation between two consecutive OFDM symbols are investigated. It is found that the two-path cancellation schemes are sensitive to the CFO deviation and the CIR performance of the conversion-based schemes degrades with large channel length. Therefore, the scheme selection depends on the actual system requirement and the channel condition. Finally, all four schemes have been tested in a recent sea experiment conducted in Taiwan in May 2013. Decoding results confirm that all proposed schemes significantly improve the OFDM UWA system performance.

1.3 Organization of the Monograph

The organization of this monograph is as follows. The UWA channel modeling is introduced in Chap. 2. The short-range RA-UAC with the adaptive power allocation is studied in Chap. 3. The medium-long-range asynchronous relay selection protocol is investigated in Chap. 4. The energy-efficient h-DLT codes design for RA-UAC is presented in Chap. 5. The effective mirror-mapping-based ICI cancellation for OFDM transmission in RA-UAC is provided in Chap. 6. A summary and discussion of future works are presented in Chap. 7.

References

1. J. Heidemann, W. Ye, J. Wills, A. Syed, Y. Li, Research challenges and applications for underwater sensor networking, in *Proceedings of Wireless Communications and Networking Conference*, Las Vegas, 3–26 April 2006, pp. 228–235
2. I.F. Akyildiz, D. Pompili, T. Melodia, Underwater acoustic sensor networks: research challenges. Elsevier Ad Hoc Netw. J. **3**(3), 257–279 (2005)
3. M. Stojanovic, On the relationship between capacity and distance in an underwater acoustic communication channel, in *Proceedings of the 1st ACM International Workshop on Underwater Networks*, Los Angeles, 25 September 2006, pp. 41–47
4. A. Syed, J. Heidemann, Time synchronization for high latency acoustic networks, in *Proceedings of International Conference on Computer Communications*, Barcelona, 23–29 April 2006, pp. 1–12
5. M. Vajapeyam, S. Vedantam, U. Mitra, J.C. Preisig, M. Stojanovic, Distributed space–time cooperative schemes for underwater acoustic communications. IEEE J. Ocean. Eng. **33**(4), 489–501 (2008)
6. F. Qu, L. Yang, Basis expansion model for underwater acoustic channels? in *Proceedings of MTS/IEEE Oceans Conference*, Quebec, 15–18 September 2008, pp. 1–7
7. M. Stojanovic, Capacity of a relay acoustic channel, in *Proceedings of MTS/IEEE Oceans Conference*, Vancouver, 29 September–4 October 2007, pp. 1–7
8. R. Cao, F. Qu, L. Yang, On the capacity and system design of relay-aided underwater acoustic communications, in *Proceedings of Wireless Communications and Networking Conference*, Sydney, 18–21 April 2010, pp. 1–6
9. S. Al-Dharrab, M. Uysal, T.M. Duman, Cooperative underwater acoustic communications. IEEE Commun. Mag. **51**(7) (2013)
10. C. Carbonelli, S.-H. Chen, U. Mitra, Error propagation analysis for underwater cooperative multi-hop communications. Elsevier Ad Hoc Netw. J. **7**(4), 759–769 (2009)
11. W. Zhang, M. Stojanovic, U. Mitra, Analysis of a linear multihop underwater acoustic network. IEEE J. Ocean. Eng. **35**(4), 961–970 (2010)
12. Z. Wang, J. Huang, S. Zhou, Z. Wang, Iterative receiver processing for OFDM modulated physical-layer network coding in underwater acoustic channels. IEEE Trans. Commun. **61**(2), 541–553 (2013)
13. C. Kam, S. Kompella, G.D. Nguyen, A. Ephremides, Z. Jiang, Frequency selection and relay placement for energy efficiency in underwater acoustic networks. IEEE J. Ocean. Eng. **39**(2), 331–342 (2014)
14. R. Cao, L. Yang, Decomposed LT codes for cooperative relay communications. IEEE J. Select. Areas Commun. **30**(2), 407–414 (2012)
15. Y. Liu, W. Chen, X. Huang, Capacity based adaptive power allocation for the OFDM relay networks with limited feedback, in *IEEE International Conference on Communications*, Kyoto, 5–9 June 2011, pp. 1–5
16. Y. Liu, W. Chen, Limited-feedback-based adaptive power allocation and subcarrier pairing for OFDM DF relay networks with diversity. IEEE Trans. Veh. Technol. **61**(6), 2559–2571 (2012)
17. Q. Song, M. Garcia, Cooperative OFDM underwater acoustic communications with limited feedback: part I. Int. J. Comput. Appl. **54**(16), 42–46 (2012)
18. X. Huang, Y. Liu, Capacity criterion-based power allocation for OFDM cooperative underwater acoustic communications with limited feedback, in *Proceedings of MTS/IEEE Oceans Conference*, Hampton Road, 14–19 October 2012, pp. 1–4
19. A. Radosevic, R. Ahmed, T.M. Duman, J.G. Proakis, M. Stojanovic, Adaptive OFDM modulation for underwater acoustic communications: design considerations and experimental results. IEEE J. Ocean. Eng. **39**(2), 357–370 (2014)
20. S.S. Haykin, *Adaptive Filter Theory* (Pearson Education India, New Delhi, 2008)
21. E.K.P. Chong, S.H. Zak, *An Introduction to Optimization* (Wiley, New York, 2013)

22. X. Cheng, L. Yang, X. Cheng, Adaptive Relay-Aided OFDM Underwater Acoustic Communications, in *Proceedings of International Conference on Communications*, London, 8–12 June 2015, pp. 1–6
23. S. Lloyd, Least squares quantization in PCM. IEEE Trans. Inf. Theory **28**(2), 129–137 (1982)
24. X. Cheng, R. Cao, F. Qu, L. Yang, Relay-aided cooperative underwater acoustic communications: Selective relaying, in *Proceedings of MTS/IEEE Oceans Conference*, Yeosu, 21–24 May 2012, pp. 1–7
25. J. Castura, Y. Mao, Rateless coding and relay networks. IEEE Signal Process. Mag. **24**(5), 27–35 (2007)
26. X. Liu, T.J. Lim, Fountain codes over fading relay channels. IEEE Trans. Wirel. Commun. **8**(6), 3278–3287 (2009)
27. A.F. Molisch, N.B. Mehta, J.S. Yedidia, J. Zhang, Performance of fountain codes in collaborative relay networks. IEEE Trans. Wirel. Commun. **6**(11), 4108–4119 (2007)
28. R. Gummadi, R.S. Sreenivas, Relaying a fountain code across multiple nodes, in *Proceedings of IEEE Information Theory Workshop*, Porto, 5–9 May 2008, pp. 149–153
29. P. Pakzad, C. Fragouli, A. Shokrollahi, Coding schemes for line networks, in *Proceedings of IEEE International Symposium on Information Theory*, Adelaide, 4–9 September 2005, pp. 1853–1857
30. A. Tarable, I. Chatzigeorgiou, I.J. Wassell, Randomly select and forward: Erasure probability analysis of a probabilistic relay channel model, in *Proceedings of IEEE Information Theory Workshop*, Taormina, 11–16 October 2009, pp. 41–4
31. H. Wicaksana, S.H. Ting, Y.L. Guan, Spectral efficient half duplex relaying for fountain code with wireless network coding, in *Proceedings of IEEE International Conference on Communications Workshops*, Beijing, 19–23 May 2008, pp. 295–299
32. S. Puducheri, J. Kliewer, T.E. Fuja, The design and performance of distributed LT codes. IEEE Trans. Inf. Theory **53**(10), 3740–3754 (2007)
33. D. Sejdinovic, R.J. Piechocki, A. Doufexi, AND-OR tree analysis of distributed LT codes, in *Proceedings of IEEE Information Theory Workshop on Networking and Information Theory*, Volos, 10–12 June 2009, pp. 261–265
34. V.S. Alagar, M. Thanh, Fast polynomial decomposition algorithms, *EUROCAL'85. Lecture Notes in Computer Science*, (Springer, Berlin Heidelberg, 1985), vol. 204, pp. 150–153
35. R.M. Corless, M.W. Giesbrecht, D.J. Jeffrey, S.M. Watt, Approximate polynomial decomposition, in *Proceedings of the 1999 International Symposium on Symbolic and Algebraic Computation*. (ACM, New York, 1999), pp. 213–219
36. X. Cheng, R. Cao, L. Yang, Practical implementation of hybrid DLT codes for cooperative relay communications, in *Proceedings of MILCOM Conference*, Orlando, 29 October–1 November 2012, pp. 1–6
37. K. Tu, D. Fertonani, T.M. Duman, M. Stojanovic, J.G. Proakis, P. Hursky, Mitigation of intercarrier interference for OFDM over time-varying underwater acoustic channels. IEEE J. Ocean. Eng. **36**(2), 156–171 (2011)
38. J. Huang, S. Zhou, J. Huang, C.R. Berger, P. Willett, Progressive inter-carrier interference equalization for OFDM transmission over time-varying underwater acoustic channels. IEEE J. Select. Top. Signal Process. **5**(8), 1524–1536 (2011)
39. T. Kang, R.A. Iltis, Iterative carrier frequency offset and channel estimation for underwater acoustic OFDM systems. IEEE J. Select. Areas Commun. **26**(9), 1650–1661 (2008)
40. M. Stojanovic, Low complexity OFDM detector for underwater acoustic channels, in *Proceedings of MTS/IEEE Oceans Conference*, Boston, 18–21 September 2006
41. M. Stojanovic, OFDM for underwater acoustic communications: Adaptive synchronization and sparse channel estimation, in *Proceeding of International Conference on Acoustics, Speech and Signal Processing*, Las Vegas, 30 March–4 April 2008, pp. 5288–5291
42. Y. Emre, V. Kandasamy, T.M. Duman, P. Hursky, S. Roy, Multi-input multi-output OFDM for shallow-water UWA communications. J. Acoust. Soc. Am. **123**(5), 3891 (2008)
43. B. Li, S. Zhou, M. Stojanovic, L. Freitag, P. Willett, Multicarrier communication over underwater acoustic channels with nonuniform Doppler shifts. IEEE J. Ocean. Eng. **33**(2), 198–209 (2008)

44. X. Cheng, F. Qu, L. Yang, Single carrier FDMA over underwater acoustic channels, in *Proceedings of CHINACOM Conference*, Harbin, 17–19 August 2011, pp. 1052–1057
45. J. Dang, F. Qu, Z. Zhang, L. Yang, Experimental results on OFDM-IDMA communications with carrier frequency offsets, in *Proceedings of MTS/IEEE Oceans Conference*, Yeosu, 21–24 May 2012
46. F. Qu, L. Yang, On the estimation of doubly-selective fading channels, in *Proceedings of Conference on Information Sciences and Systems*, The Princeton University, Princeton,19–21 March 2008, pp. 17–24
47. G. Leus, P.A. van Walree, Multiband OFDM for covert acoustic communications. IEEE J. Select. Areas Commun. **26**(9), 1662–1673 (2008)
48. S.F. Mason, C.R. Berger, S. Zhou, K.R. Ball, L. Freitag, P. Willett, Receiver comparisons on an OFDM design for Doppler spread channels, in *Proceedings of MTS/IEEE Oceans Conference*, Bremen, 11–14 May 2009, pp. 1–7
49. X. Xu, Z. Wang, S. Zhou, L. Wan, Parameterizing both path amplitude and delay variations of underwater acoustic channels for block decoding of orthogonal frequency division multiplexing, J. Acoust. Soc. Am. **131**, 4672 (2012)
50. X. Xu, G. Qiao, J. Su, P. Hu, E. Sang, Study on turbo code for multicarrier underwater acoustic communication, in *Proceedings of 2008 International Conference on Wireless Communications, Networking and Mobile Computing*, Dalian, 12–14 October 2008, pp. 1–4
51. X. Cheng, R. Griffin, F. Qu, L. Yang, A comparison of multiband and single-band OFDM for underwater acoustic communications, in *Proceedings of Acoustics*, Hong Kong, 13–18 May 2012
52. T. Wang, J.G. Proakis, J.R. Zeidler, Techniques for suppression of intercarrier interference in OFDM systems, in *Proceedings of Wireless Communications and Networking Conference*, vol. 1, 13–17 March 2005, pp. 39–44
53. X. Huang, H.-C. Wu, Robust and efficient intercarrier interference mitigation for OFDM systems in time-varying fading channels. IEEE Trans. Veh. Technol. **56**(5), 2517–2528 (2007)
54. Z. Tang, R.C. Cannizzaro, G. Leus, P. Banelli, Pilot-assisted time-varying channels estimation for OFDM systems. IEEE Trans. Signal Process. **55**(5), 2226–2238 (2007)
55. Y. Zhao, S.-G. Haggman, Intercarrier interference self-cancellation scheme for OFDM mobile communication systems. IEEE Trans. Commun. **49**(7), 1185–1191 (2001)
56. X. Cheng, M. Wen, X. Cheng, D. Duan, L. Yang, Effective mirror-mapping-based intercarrier interference cancellation for OFDM underwater acoustic communications. Ad Hoc Netw. **34**, 5–16 (2015)
57. M. Wen, X. Cheng, X. Cheng, L. Yang, B. Jiao, Effective intercarrier interference reduction techniques for OFDM underwater acoustic communications, in *Proceedings of Asilomar Conference on Signals, Systems and Computers*, Pacific Grove, 3–6 November 2013 (invited)
58. X. Cheng, M. Wen, X. Cheng, L. Yang, Z. Xu, Effective self-cancellation of intercarrier interference for OFDM underwater acoustic communications, in *ACM International Workshop on UnderWater Networks*, Kaohsiung, 11–13 November 2013

Chapter 2
Underwater Acoustic Channel Models

In this chapter, we introduce two prevailing UWA channel models, namely, the empirical UWA channel model and the statistical time-varying UWA channel model, to capture the features of RA-UAC systems from different aspects. In addition, the relationship between the coherence time and transmission distances is also explored to reveal the fundamental difference between the short-range UAC and the medium-long range UAC.

2.1 Empirical UWA Channel Model

The empirical UWA channel model is measured through sea trials. The signal attenuation $\mathcal{A}$ of a path is dependent on both distance d and subcarrier frequency f_k:

$$\mathcal{A}(d, f_k) = d^e a(f_k)^d, \tag{2.1}$$

where e is the path loss exponent reflecting the geometry of acoustic signal propagation. We adopt $e = 1.5$ for practical spreading. The frequency dependency is captured by $a(f_k)$, which is given by Thorp's formula [1] in dB/km:

$$10 \log a(f_k) = \frac{0.11 f_k^2}{1 + f_k^2} + \frac{44 f_k^2}{4100 + f_k^2} + 2.75 \cdot 10^{-4} f_k^2 + 0.003. \tag{2.2}$$

In (2.1) and (2.2), frequency f_k is in kHz.

In addition, the noise variance is also frequency-dependent and empirically modeled as

$$10 \log \mathcal{N}(f_k) = \mathcal{N}_1 - \eta \log(f_k) + 10 \log \Delta f, \tag{2.3}$$

X. Cheng et al., *Cooperative OFDM Underwater Acoustic Communications*,
Wireless Networks, DOI 10.1007/978-3-319-33207-9_2

where $\mathcal{N}_1$ and η are constants with empirical values $\mathcal{N}_1 = 50\,\text{dB re }\mu\text{Pa per Hz}$ and $\eta = 18\,\text{dB/decade}$, respectively. Frequency f_k is in kHz, and the subcarrier spacing Δf is in Hz.

2.2 Statistical Time-Varying UWA Channel Model

Due to the slow propagation of UWA waves, signals reflected from the sea surface and bottom arrive at the receiver with distinct delays. This results in a sparse multipath channel [2, 3]. We consider the long-term path loss and the short-term random fading to model the discrete-time baseband UWA channels. The long-term pass loss is modeled as a deterministic discrete-time UWA channel $\bar{\boldsymbol{h}} = [0, \cdots, \bar{h}_{l_0}, 0, \cdots, \bar{h}_{l_1}, 0, \cdots, \bar{h}_{l_{L_{nz}-1}}]^T$, within which only L_{nz} taps are nonzero. Each nonzero tap $\bar{h}_l,\ l \in \{l_0, \cdots, l_{L_{nz}-1}\}$ corresponds to the pass loss of the lth arrival with delay $\tau_l = l\Delta t$, where $\Delta t = 1/B$ is the tap length and B is the system bandwidth. The randomness of nonzero taps is modeled as independent Rayleigh fading [4, 5]. The resultant channel coefficients are given as an $L \times 1$ vector $\boldsymbol{h} = [0, \cdots, h_{l_0}, 0, \cdots, h_{l_1}, 0, \cdots, h_{l_{L_{nz}-1}}]^T$ with each nonzero tap $h_l,\ l \in \{l_0, \cdots, l_{L_{nz}-1}\}$ following the independent complex Gaussian distribution, i.e., $h_l \sim \mathcal{CN}(0, |\bar{h}_l|^2)$. The discrete-time baseband CIRs of the time-varying UWA channels are given as

$$h(t, \tau) = \sum_{l \in \{l_0, \cdots, l_{L_{nz}-1}\}} h_l(t)\delta(\tau - l), \tau \in \{0, 1, \cdots, L-1\}. \tag{2.4}$$

Jake's model is utilized to capture the channel variation, i.e., $\mathbb{E}[h_l(t)h_{l'}^*(t')] = R_h(t-t', l)\delta(l-l')$. $R_h(t-t', l) = |\bar{h}_l|^2 J_0(2\pi f_d(t-t'))$ is the autocorrelation between time t and time t' for path l. f_d is the maximum Doppler shift, and $J_0(\cdot)$ is the zeroth-order Bessel function of the first kind. It is confirmed in [6] that as long as the motion-induced nonuniform Doppler shift is removed through received signal resampling, the Doppler scaling factor a can be very small, i.e., $a < 10^{-4}$. With carrier frequency $f_c = 17\,\text{kHz}$ as an example, the maximum Doppler shift $f_d = af_c$ is less than 1.7 Hz. After residual carrier frequency offset (CFO) compensation, f_d can be further reduced [7]. Therefore, we assume that after the major Doppler effect has been removed through received signal resampling and residual CFO compensation, f_d is very small ($f_d < 0.5\,\text{Hz}$), which means h_l changes slowly over a few seconds.

For an OFDM-based communication system, the channel response in the FD is given as $\boldsymbol{H} = \sqrt{N}\boldsymbol{F}_N\boldsymbol{P}\boldsymbol{h}$, where N is the subcarrier number, $\boldsymbol{F}_N$ is $N \times N$ discrete Fourier transform (DFT) matrix with $\boldsymbol{F}_N\boldsymbol{F}_N^H = \boldsymbol{I}_N$, and $\boldsymbol{P} = [\boldsymbol{I}_L\ \boldsymbol{0}_{L\times(N-L)}]^T$ is the zero-padding matrix. The kth element of $\boldsymbol{H}$ is $H_k = \sum_{n=0}^{L-1} e^{-j\frac{2\pi}{N}kn}h_n, k = 0, \cdots, N-1$ and is complex Gaussian distributed, i.e., $H_k \sim \mathcal{CN}(0, \eta)$ where $\eta = \sum_{n=0}^{L_{nz}-1} \mathbb{E}[|h_{l_n}|^2] = \sum_{l \in \{l_0, \cdots, l_{L_{nz}-1}\}} \left|\bar{h}_l\right|^2$. η is actually the channel power, i.e., the total energy of all nonzero channel paths, which depends on the transmitter and receiver locations as well as the sea geometry.

2.3 Relationship Between Coherence Time and Transmission Distances

According to Clarke's model [8], the coherence time is defined as

$$T_c = \sqrt{\frac{9}{16\pi f_d^2}} \approx \frac{0.423}{f_d} = \frac{0.423}{af_c}, \tag{2.5}$$

where f_d is the Doppler shift, f_c is the carrier frequency, and a is the Doppler scaling factor. Suppose the distance between the transmitter and the receiver is D. Then the round-trip delay time is $\Delta_T = 2D/c$. The quasi-static channel assumption during the feedback signal propagation holds if the coherence time is larger than the round-trip delay time, i.e.,

$$T_c > \Delta_T, \tag{2.6}$$

or

$$D < D_c = \frac{0.212c}{af_c}. \tag{2.7}$$

In an UWA channel with $c = 1500\,\text{m/s}$, $f_c = 17\,\text{kHz}$, and $a = 3 \times 10^{-5}$, the transmission distance D has to be less than $D_c = 624\,\text{m}$. This means that for short-range UAC ($0.1 \sim 1\,\text{km}$), the instantaneous CSI feedback from the receiver to the transmitter is feasible, especially with the help of channel prediction. However, for medium-long-range UAC ($\gg 1$) km, due to the slow propagation speed of UWA signal ($c \approx 1500\,\text{m/s}$), the propagation time of the feedback signal could be much larger than the coherence time and nullify the instantaneous CSI feedback. Therefore, the adoption of the instantaneous CSI feedback depends on the transmission distances and the level of channel variation after Doppler compensation.

In summary, the unique features of UWA channels have great impacts on the design of the energy-efficient and reliable RA-UAC.

References

1. L. Berkhovskikh, Y. Lysanov, *Fundamentals of Ocean Acoustics* (Springer, New York, 1982)
2. M. Stojanovic, On the relationship between capacity and distance in an underwater acoustic communication channel, in *Proceedings of the 1st ACM International Workshop on Underwater Networks*, Los Angeles, 25 September 2006, pp. 41–47
3. C.R. Berger, S. Zhou, J.C. Preisig, P. Willett, Sparse channel estimation for multicarrier underwater acoustic communication: from subspace methods to compressed sensing. IEEE Trans. Signal Process. **58**(3), 1708–1721 (2010)

4. M. Chitre, A high-frequency warm shallow water acoustic communications channel model and measurements. J. Acoust. Soc. Am. **122**(5), 2580–2586 (2007)
5. C. Choudhuri, U. Mitra, Capacity bounds and power allocation for underwater acoustic relay channels with ISI, in *Proceedings of the Fourth ACM International Workshop on UnderWater Networks*, Berkeley, 3 November 2009, p. 6
6. A. Radosevic, R. Ahmed, T.M. Duman, J.G. Proakis, M. Stojanovic, Adaptive OFDM modulation for underwater acoustic communications: Design considerations and experimental results. IEEE J. Ocean. Eng. **39**(2), 357–370 (2014)
7. B. Li, S. Zhou, M. Stojanovic, L. Freitag, P. Willett, Multicarrier communication over underwater acoustic channels with nonuniform Doppler shifts. IEEE J. Ocean. Eng. **33**(2), 198–209 (2008)
8. T.S. Rappaport, *Wireless Communications: Principles and Practice* (New Jersey:Prentice Hall PTR, Upper Saddle River, 2001)

Chapter 3
Short-Range Adaptive RA-UAC

In this chapter, we present the adaptive system design for the short-range RA-UAC to improve the communication reliability. We design the adaptive RA-UAC system in three steps. As a fundamental step, we derive the optimal power allocation and distribution between the source and the relay with individual and total power constraints. In the second step, we implement channel prediction to compensate the channel variation during CSI signal feedback using the RLS adaptive filter. In the last step, the Lloyd algorithm is adopted to quantize CSI efficiently to adapt to the band-limited UWA channels.

3.1 System Model

We consider a dual-hop RA-UAC system with the topology depicted in Fig. 3.1. The system consists of three nodes: source node S, relay node R, and destination node D. The distance between node S and node R is d_1, and the distance between node R and node D is d_2. There is no DL between the source and the destination due to the blocking between them.

The system diagram of the proposed adaptive OFDM RA-UAC system is given in Fig. 3.2. The system consists of source transmission, relay forwarding, and destination decoding, detailed as follows:

1. *Source transmission*: For each OFDM symbol to transmit, the power allocation at the source and distribution cross subcarriers is calculated based on the received *S-R* and relay-to-destination (*R-D*) CSI feedback from the relay and the destination. Then, the source transmits the OFDM symbol to the relay with the calculated power allocation.
2. *Relay forwarding*: After receiving signals from the source, the Doppler shift is compensated first at the relay. Then, for each received OFDM symbol, the relay estimates the *S-R* channel impulse response and calculates its power

X. Cheng et al., *Cooperative OFDM Underwater Acoustic Communications*,
Wireless Networks, DOI 10.1007/978-3-319-33207-9_3

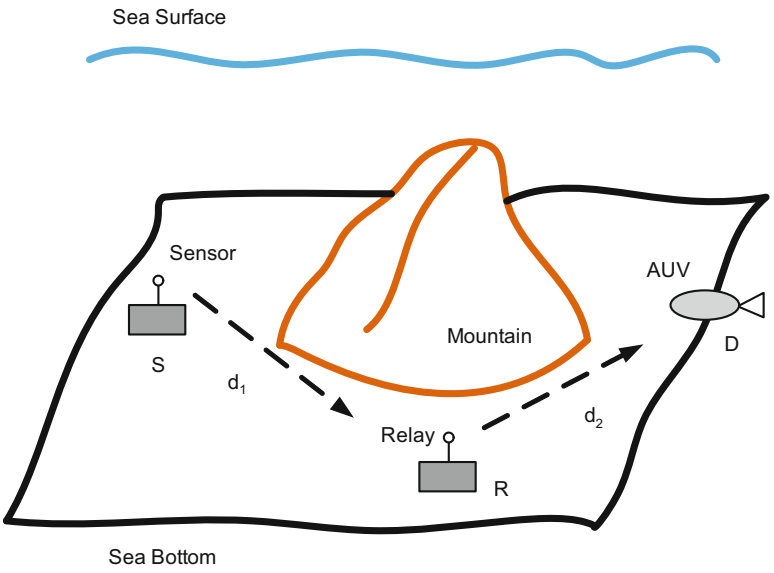

Fig. 3.1 RA-UAC system

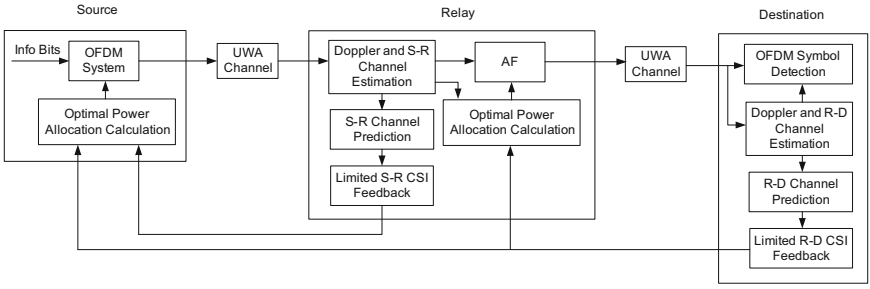

Fig. 3.2 Data transmission in the adaptive RA-UAC system

allocation and distribution at each subcarrier based on *S-R* channel impulse response and received *R-D* CSI feedback from the destination. Then the relay amplifies and forwards the received OFDM symbol to the destination according to the calculated power allocation. At the same time, the relay predicts the future *S-R* channel impulse response and quantizes it. Quantized *S-R* CSI together with received quantized *R-D* CSI for the source from the destination is fed back to the source using the limited feedback channel.

3. *Destination decoding*: At the destination, after compensating the Doppler shift and estimating the *R-D* channel impulse response, the received OFDM symbols are decoded. At the same time, the destination predicts and quantizes the future *R-D* channel impulse responses for each of the source and the relay, respectively.

Then it feeds back quantized *R-D* CSI for the source and the relay to the relay using the limited feedback channel.

In the following sections, the key components of our proposed adaptive RA-UAC system, namely, optimal power allocation and distribution, channel prediction, and channel quantization, are studied, respectively.

3.2 Optimal Power Allocation

For the transmission of an OFDM symbol in the AF-based RA-UAC system, the equivalent end-to-end SNR [1, 2] at the kth subcarrier is computed as

$$\gamma_{eq}(f_k) = \frac{\gamma_{S,R}(f_k)\gamma_{R,D}(f_k)}{\gamma_{S,R}(f_k) + \gamma_{R,D}(f_k) + 1}, \tag{3.1}$$

where

$$\gamma_{i,j}(f_k) = \frac{\mathcal{P}_i(f_k)A_{i,j}(f_k)}{N_j(f_k)} \tag{3.2}$$

represents the DL SNR from node i to node j, $i, j \in \{S,\ R,\ D\}$, f_k is the subcarrier frequency, $\mathcal{P}_i(f_k)$ is the transmit power at node i, $A_{i,j}(f_k) = |H_{i,j}(f_k)|^2$ is the signal attenuation, and $N_j(f_k)$ is the noise variance at node j. It is worth noticing that $H_{i,j}(f_k)$ is the instantaneous channel frequency response (CFR) after Doppler compensation.

The system capacity of AF-based RA-UAC is calculated as

$$\mathcal{C}_{RA} = \max_{\mathcal{P}_S(f_k),\mathcal{P}_R(f_k)} \Delta f \sum_{k=1}^{K} \log_2(1 + \gamma_{eq}(f_k)) \tag{3.3}$$

with total power constraint

$$\sum_{k=1}^{K} [\mathcal{P}_S(f_k) + \mathcal{P}_R(f_k)] = \mathcal{P}_T \tag{3.4}$$

and individual power constraints

$$\begin{aligned} \sum_{k=1}^{K} \mathcal{P}_S(f_k) &\le \mathcal{P}_{M_S} \\ \sum_{k=1}^{K} \mathcal{P}_R(f_k) &\le \mathcal{P}_{M_R}, \end{aligned} \tag{3.5}$$

where $\mathcal{P}_T \leq \mathcal{P}_{M_S} + \mathcal{P}_{M_R}$. It is worth noticing that the capacity of AF-based RA-UAC with total power constraint is studied in [2]. However, adding the individual power constraints could change the system capacity and the optimal power allocation. Therefore, it is worth investigating the system capacity of AF-based RA-UAC under both the total power constraint and the individual power constraints.

With the SNR expression in (3.1), the closed-form solution to this optimization problem is mathematically intractable. Thus, we resort to the upper and lower bounds of (3.3) to characterize its features similar to [2].

It can be readily shown that the equivalent SNR $\gamma_{eq}(f_k)$ is upper bounded by [2]

$$\gamma_u(f_k) = \frac{\mathcal{P}_S(f_k)\Gamma_{S,R}(f_k)\mathcal{P}_R(f_k)\Gamma_{R,D}(f_k)}{\mathcal{P}_S(f_k)\Gamma_{S,R}(f_k) + \mathcal{P}_R(f_k)\Gamma_{R,D}(f_k)} \tag{3.6}$$

and lower bounded by

$$\gamma_l(f_k) = \frac{\mathcal{P}_S(f_k)\Gamma_{S,R}(f_k)\mathcal{P}_R(f_k)\Gamma_{R,D}(f_k)}{\mathcal{P}_S(f_k)\Gamma_{S,R}(f_k) + \mathcal{P}_R(f_k)\Gamma_{R,D}(f_k)} - \frac{1}{4}, \tag{3.7}$$

where $\Gamma_{S,R}(f_k) = \frac{A_{S,R}(f_k)}{N_R(f_k)}$ and $\Gamma_{R,D}(f_k) = \frac{A_{R,D}(f_k)}{N_D(f_k)}$. Accordingly, the following results can be established:

Theorem 3.1. *The upper bound of the capacity of AF-based RA-UAC is*

$$\begin{aligned} \mathcal{C}^u_{RA}(\lambda_u^{(a)}, \lambda_u^{(b)}) &= \max_{\mathcal{P}_S(f_k), \mathcal{P}_R(f_k)} \Delta f \sum_{k=1}^{K} \log_2 (1 + \gamma_u(f_k)) \\ &= \Delta f \sum_{k=1}^{K} \log_2 \left[\frac{1}{\ln(2) F^2(f_k, \lambda_u^{(a)}, \lambda_u^{(b)})} \right] \end{aligned} \tag{3.8}$$

where function F is given by (3.22) *and the optimal power allocation* $\mathcal{P}_S^u$ *and* $\mathcal{P}_R^u$ *are in* (3.20) *and* (3.21)*, respectively.* $\lambda_u^{(a)}$ *and* $\lambda_u^{(b)}$ *are chosen such that the total and individual power constraints are met; the lower bound of the capacity of AF-based RA-UAC is*

$$\begin{aligned} \mathcal{C}^l_{RA}(\lambda_l^{(a)}, \lambda_l^{(b)}) &= \max_{\mathcal{P}_S(f_k), \mathcal{P}_R(f_k)} \Delta f \sum_{k=1}^{K} \log_2 (1 + \gamma_l(f_k)) \\ &= \Delta f \sum_{k=1}^{K} \log_2 \left[\frac{1}{\ln(2) F^2(f_k, \lambda_l^{(a)}, \lambda_l^{(b)})} \right] \end{aligned} \tag{3.9}$$

where the optimal power allocation $\mathcal{P}_S^l$ *and* $\mathcal{P}_R^l$ *are in* (3.29) *and* (3.30)*, respectively.* $\lambda_l^{(a)}$ *and* $\lambda_l^{(b)}$ *are chosen such that the total and individual power constraints are met.*

Proof (Upper Bound of the Capacity of AF-Based RA-UAC). The upper bound of the capacity of AF-based RA-UAC is

$$\mathcal{C}_{RA}^{u} = \max_{\mathcal{P}_S(f_k),\mathcal{P}_R(f_k)} \Delta f \sum_{k=1}^{K} \log_2\left(1+\gamma_u(f_k)\right) \tag{3.10}$$

with total and individual power constraints, i.e., (3.4) and (3.5). Since (3.10) is a concave function over a convex set, it is a convex optimization problem. The optimal transmit power $\mathcal{P}_S^u(f_k)$ and $\mathcal{P}_R^u(f_k)$ can be obtained by solving the KKT conditions [3].

Define

$$\begin{aligned}\mathcal{L} = &-\sum_{k=1}^{K} \log_2\left(1+\gamma_u(\mathcal{P}_S(f_k),\mathcal{P}_R(f_k))\right) \\ &+ \lambda_u^{(0)} \sum_{k=1}^{K} \left[\mathcal{P}_S(f_k)+\mathcal{P}_R(f_k)\right] \\ &+ \lambda_u^{(1)} \sum_{k=1}^{K} \mathcal{P}_S(f_k) + \lambda_u^{(2)} \sum_{k=1}^{K} \mathcal{P}_R(f_k).\end{aligned} \tag{3.11}$$

The KKT conditions are given as follows:

$$\frac{\partial \mathcal{L}}{\partial \mathcal{P}_S(f_k)} = \frac{\partial \mathcal{L}}{\partial \mathcal{P}_R(f_k)} = 0, \quad k = 1,\cdots,K \tag{3.12}$$

$$\lambda_u^{(1)} \left[\sum_{k=1}^{K} \mathcal{P}_S(f_k) - \mathcal{P}_{M_S}\right] = 0 \tag{3.13}$$

$$\lambda_u^{(2)} \left[\sum_{k=1}^{K} \mathcal{P}_R(f_k) - \mathcal{P}_{M_R}\right] = 0 \tag{3.14}$$

$$\mathcal{P}_S(f_k), \mathcal{P}_R(f_k), \lambda_u^{(0)}, \lambda_u^{(1)}, \lambda_u^{(2)} \geq 0. \tag{3.15}$$

Differentiating the Lagrangian with respect to $\mathcal{P}_S(f_k)$ and $\mathcal{P}_R(f_k)$, we can achieve

$$\frac{\partial \mathcal{L}}{\partial \mathcal{P}_S(f_k)} = \frac{\Gamma_{S,R}(f_k)(\Gamma_{R,D}(f_k)\mathcal{P}_R(f_k))^2/\ln(2)}{D(f_k)} - \lambda_u^{(a)} \tag{3.16}$$

$$\frac{\partial \mathcal{L}}{\partial \mathcal{P}_R(f_k)} = \frac{\Gamma_{R,D}(f_k)(\Gamma_{S,R}(f_k)\mathcal{P}_S(f_k))^2/\ln(2)}{D(f_k)} - \lambda_u^{(b)} \tag{3.17}$$

where $\lambda_u^{(a)} = \lambda_u^{(0)} + \lambda_u^{(1)}$, $\lambda_u^{(b)} = \lambda_u^{(0)} + \lambda_u^{(2)}$, and

$$\begin{aligned} D(f_k) = &\left(\mathcal{P}_S(f_k)\Gamma_{S,R}(f_k) + \mathcal{P}_R(f_k)\Gamma_{R,D}(f_k)\right)^2 \\ &+ \mathcal{P}_S^2(f_k)\Gamma_{S,R}^2(f_k)\mathcal{P}_R(f_k)\Gamma_{R,D}(f_k) \\ &+ \mathcal{P}_S(f_k)\Gamma_{S,R}(f_k)\mathcal{P}_R^2(f_k)\Gamma_{R,D}^2(f_k). \end{aligned} \tag{3.18}$$

After setting the two derivatives to zero, the relationship between $\mathcal{P}_S(f_k)$ and $\mathcal{P}_R(f_k)$ is shown as follows:

$$\frac{\mathcal{P}_S(f_k)}{\mathcal{P}_R(f_k)} = \sqrt{\frac{\lambda_u^{(b)}\Gamma_{R,D}(f_k)}{\lambda_u^{(a)}\Gamma_{S,R}(f_k)}}. \tag{3.19}$$

Equation (3.19) reveals the optimal power allocation ratio at a subcarrier is proportional to the reciprocal of the channel gain ratio. After substituting (3.19) into (3.16) and solving $\frac{\partial \mathcal{L}}{\partial \mathcal{P}_S(f_k)} = 0$ with constraints $\mathcal{P}_S(f_k) \geq 0$ and $\mathcal{P}_R(f_k) \geq 0$, we can compute the optimal $\mathcal{P}_S^u(f_k)$ and $\mathcal{P}_R^u(f_k)$ as

$$\mathcal{P}_S^u(f_k, \lambda_u^{(a)}, \lambda_u^{(b)}) = \frac{1}{\sqrt{\lambda_u^{(a)}\Gamma_{S,R}(f_k)}}\left[\frac{1}{\ln(2)F(f_k)} - F(f_k)\right]^+ \tag{3.20}$$

and

$$\mathcal{P}_R^u(f_k, \lambda_u^{(a)}, \lambda_u^{(b)}) = \frac{1}{\sqrt{\lambda_u^{(b)}\Gamma_{R,D}(f_k)}}\left[\frac{1}{\ln(2)F(f_k)} - F(f_k)\right]^+ \tag{3.21}$$

where

$$F(f_k, \lambda_u^{(a)}, \lambda_u^{(b)}) = \sqrt{\frac{\lambda_u^{(a)}}{\Gamma_{S,R}(f_k)}} + \sqrt{\frac{\lambda_u^{(b)}}{\Gamma_{R,D}(f_k)}}. \tag{3.22}$$

Then the upper bound of the system capacity, i.e., (3.8), can be obtained by substituting (3.20) and (3.21) into (3.10).

The parameters $\lambda_u^{(a)}$ and $\lambda_u^{(b)}$ should be chosen such that the total and individual power constraints are met. The following three steps are adopted to obtain $\lambda_u^{(a)}$ and $\lambda_u^{(b)}$.

Step I

Assume $\lambda_u^{(1)} = 0$ and $\lambda_u^{(2)} = 0$, which implies $\lambda_u^{(a)} = \lambda_u^{(b)} = \lambda_u^{(0)}$. Then, the KKT multiplier $\lambda_u^{(0)}$ should be chosen such that

$$\sum_{k=1}^{K}\left[\mathcal{P}_S^u(f_k, \lambda_u^{(0)}) + \mathcal{P}_R^u(f_k, \lambda_u^{(0)})\right] = \mathcal{P}_T. \tag{3.23}$$

For the obtained $\lambda_u^{(0)}$, if $\sum_{k=1}^{K} \mathcal{P}_S(f_k, \lambda_u^{(0)}) \leq \mathcal{P}_{M_S}$ and $\sum_{k=1}^{K} \mathcal{P}_R(f_k, \lambda_u^{(0)}) \leq \mathcal{P}_{M_R}$, $\lambda_u^{(a)}$ and $\lambda_u^{(b)}$ that satisfy the total and individual power constraints are found. However, if $\sum_{k=1}^{K} \mathcal{P}_S(f_k, \lambda_u^{(0)}) > \mathcal{P}_{M_S}$, which implies that the source has to transmit with full power, go to Step II. If $\sum_{k=1}^{K} \mathcal{P}_R(f_k, \lambda_u^{(0)}) > \mathcal{P}_{M_R}$, which implies the relay has to transmit with full power, go to Step III.

Step II

In this case, $\lambda_u^{(2)} = 0$. This means $\lambda_u^{(a)} = \lambda_u^{(0)} + \lambda_u^{(1)}$ and $\lambda_u^{(b)} = \lambda_u^{(0)}$. Then, the KKT multipliers $\lambda_u^{(a)}$ and $\lambda_u^{(b)}$ should be chosen such that the following power constraints are satisfied:

$$\sum_{k=1}^{K} \left[\mathcal{P}_S^u(f_k, \lambda_u^{(a)}, \lambda_u^{(b)}) + \mathcal{P}_R^u(f_k, \lambda_u^{(a)}, \lambda_u^{(b)})\right] = \mathcal{P}_T \tag{3.24}$$

$$\sum_{k=1}^{K} \mathcal{P}_S(f_k, \lambda_u^{(a)}, \lambda_u^{(b)}) = \mathcal{P}_{M_S}. \tag{3.25}$$

Step III

In this case, $\lambda_u^{(1)} = 0$. Therefore $\lambda_u^{(a)} = \lambda_u^{(0)}$ and $\lambda_u^{(b)} = \lambda_u^{(0)} + \lambda_u^{(2)}$. Then, the KKT multipliers $\lambda_u^{(a)}$ and $\lambda_u^{(b)}$ should be chosen such that the following power constraints are satisfied:

$$\sum_{k=1}^{K} \left[\mathcal{P}_S^u(f_k, \lambda_u^{(a)}, \lambda_u^{(b)}) + \mathcal{P}_R^u(f_k, \lambda_u^{(a)}, \lambda_u^{(b)})\right] = \mathcal{P}_T \tag{3.26}$$

$$\sum_{k=1}^{K} \mathcal{P}_R(f_k, \lambda_u^{(a)}, \lambda_u^{(b)}) = \mathcal{P}_{M_R}. \tag{3.27}$$

(Lower Bound of the Capacity of AF-Based RA-UAC). The lower bound of the capacity of AF-based RA-UAC is given as

$$\mathcal{C}_{RA}^{l} = \max_{\mathcal{P}_S(f_k), \mathcal{P}_R(f_k)} \Delta f \sum_{k=1}^{K} \log_2(1 + \gamma_l(f_k)) \tag{3.28}$$

with total and individual power constraints, i.e., (3.4) and (3.5).

After solving KKT conditions, the optimal $\mathcal{P}_S^l(f_k)$ and $\mathcal{P}_R^l(f_k)$ for $\mathcal{C}_{RA}^{l}$ can be obtained as

$$\mathcal{P}_S^l(f_k, \lambda_l) = \frac{1}{\sqrt{\lambda_l^{(a)} \Gamma_{S,R}(f_k)}} \left[\frac{1}{\ln(2) F(f_k)} - \frac{3}{4} F(f_k)\right]^+ \tag{3.29}$$

and

$$\mathcal{P}_R^l(f_k, \lambda_l) = \frac{1}{\sqrt{\lambda_l^{(b)} \Gamma_{R,D}(f_k)}} \left[\frac{1}{\ln(2) F(f_k)} - \frac{3}{4} F(f_k)\right]^+. \tag{3.30}$$

The resultant lower bound of the system capacity is given by (3.9). The parameters $\lambda_l^{(a)}$ and $\lambda_l^{(b)}$ are chosen such that the total and individual power constraints are met. Same as the upper bound calculation, three steps should be followed to obtain $\lambda_l^{(a)}$ and $\lambda_l^{(b)}$. □

Similar to the power optimization results in [2], for tight bounds of $\mathcal{C}_{RA}^l$ and $\mathcal{C}_{RA}^u$, the power allocation $[\mathcal{P}_S^l(f_k), \mathcal{P}_R^l(f_k)]$ in (3.29) and (3.30) could be treated as the optimal power allocation for AF-based RA-UAC with individual and total power constraints. Sect. 3.5 will verify the tightness of $\mathcal{C}_{RA}^l$ and $\mathcal{C}_{RA}^u$ numerically.

3.3 Channel Prediction

To enable the adaptive RA-UAC system, CSI needs to be fed back to the source and the relay, respectively. However, due to the slow acoustic signal propagation and the channel variation, CSI could be outdated when it arrives at the source and the relay. Therefore, the channel variation needs to be compensated by channel prediction. The channel predictability of UWA channels over several seconds which corresponds to a round-trip distance of a few kilometers is verified in [4] as long as the motion-induced nonuniform Doppler shift is removed and the residual CFO is compensated [5]. In the following, we assume that the major Doppler effect has been removed through received signal resampling and CFO compensation, and the resultant channel impulse response varies slowly over a few seconds.

3.3.1 Problem Statement

Suppose the channel impulse response at time t is given as an $L \times 1$ vector $\tilde{\boldsymbol{h}}(t) = [0, \cdots, \tilde{h}_{l_0}(t), \cdots, \tilde{h}_{l_{L_{nz}-1}}(t)]^T$ with nonzero taps $\tilde{h}_l(t)$, $l \in \{l_0, \cdots, l_{L_{nz}-1}\}$, where L_{nz} is the number of nonzero taps. The estimated channel impulse response at tap l is

$$h_l(t) = \tilde{h}_l(t) + e_l(t), \tag{3.31}$$

where $e_l(t)$ is the random error caused by channel estimation with variance σ_e^2. Then, the estimated channel impulse response in the vector form is $\boldsymbol{h}(t) = [0, \cdots, h_{l_0}(t), \cdots, h_{l_{L_{nz}-1}}(t)]^T$.

Let $T' = T_g + T$ where T_g and T are the guard time interval and the symbol duration, respectively, and OFDM symbols are received at time $t = 0, T', 2T', \cdots$. The channel is predicted for each nonzero tap separately. Then, for each newly obtained CSI $h_l(nT')$ at time nT', the vector $[h_l(nT'), h_l((n-1)T'), \cdots, h_l((n-N+1)T')]^T$ is constructed to predict $h_l((n+\Delta)T')$ where Δ is the prediction advance factor and N is the window size. In the following, T' and l are dropped for notational simplicity. The linear prediction is given as

$$\hat{h}(n+\Delta) = \boldsymbol{u}^T(n)\boldsymbol{W}(n), \tag{3.32}$$

where $\boldsymbol{u}(n) = [h(n), h(n-1), \cdots, h(n-N+1)]^T$ and $\boldsymbol{W}(n) = [W_0(n), W_1(n), \cdots, W_{N-1}(n)]^T$. Our goal is to find $\boldsymbol{W}(n)$ such that $\sum_{k=N-1+\Delta}^{n} \lambda^{n-k}|\hat{h}(k) - h(k)|^2$ is minimized. In other words,

$$\begin{aligned}\boldsymbol{W}(n) &= \arg \min_{W_0, W_1, \cdots, W_{N-1}} \sum_{k=N-1+\Delta}^{n} \lambda^{n-k}|\hat{h}(k) - h(k)|^2 \\ &= \arg \min_{W_0, W_1, \cdots, W_{N-1}} \|\boldsymbol{\Lambda}(n)\boldsymbol{A}(n)\boldsymbol{W} - \boldsymbol{\Lambda}(n)\boldsymbol{b}(n)\|^2, \end{aligned} \tag{3.33}$$

where $\boldsymbol{A}(n) = [\boldsymbol{u}(n-\Delta), \boldsymbol{u}(n-\Delta-1), \cdots, \boldsymbol{u}(N-1)]^T$, $\boldsymbol{W} = [W_0, W_1, \cdots, W_{N-1}]^T$, $\boldsymbol{b}(n) = [h(n), h(n-1), \cdots, h(N-1+\Delta)]^T$, $\boldsymbol{\Lambda}(n) = \text{diag}\{1, \lambda^{\frac{1}{2}}, \lambda, \cdots, \lambda^{\frac{n-\Delta-N+1}{2}}\}$, and $0 < \lambda \leqslant 1$ is the forgetting factor. As seen in (3.33), if $\lambda = 1$, the channel samples of all time instances are treated equally, and this is suitable when the channel statistics is stationary. However, if the channel statistics is non-stationary, the recent channel samples should be weighted heavily by choosing $\lambda < 1$.

The solution to this least square estimation problem can be readily obtained as

$$\begin{aligned}\boldsymbol{W}(n) &= \left[\boldsymbol{A}^H(n)\boldsymbol{\Lambda}^2(n)\boldsymbol{A}(n)\right]^{-1}\boldsymbol{A}^H(n)\boldsymbol{\Lambda}^2(n)\boldsymbol{b}(n) \\ &= \left(\sum_{k=N-1}^{n-\Delta} \lambda^{n-\Delta-k}\boldsymbol{u}^*(k)\boldsymbol{u}^T(k)\right)^{-1} \\ &\quad \times \sum_{k=N-1}^{n-\Delta} \lambda^{n-\Delta-k}\boldsymbol{u}^*(k)h(k+\Delta). \end{aligned} \tag{3.34}$$

3.3.2 MSE Analysis

The prediction MSE at time n is given as

$$\mathcal{E}_P(\Delta, n) = \mathbb{E}\|\tilde{h}(n+\Delta) - \boldsymbol{u}^T(n)\boldsymbol{W}(n)\|^2. \tag{3.35}$$

To analyze the prediction MSE, we consider the case that the channel is wide-sense stationary and $\lambda = 1$, and the following theorem is established.

Theorem 3.2. *When $\tilde{h}(n)$ is wide-sense stationary, i.e., $R(\tau) = \mathbb{E}\left[\tilde{h}(n+\tau)\tilde{h}^*(n)\right]$ and $\lambda = 1$, the MSE with channel prediction is given as*

$$\lim_{n\to\infty} \mathcal{E}_P(\Delta, n) = R(0) - \boldsymbol{Z}(\Delta)^H(\boldsymbol{R} + \sigma_e^2\boldsymbol{I}_N)^{-1}\boldsymbol{Z}(\Delta), \tag{3.36}$$

and the MSE without channel prediction, i.e., $\hat{h}(n+\Delta) = h(n)$, is given as

$$\mathcal{E}_{NP}(\Delta) = 2\left[R(0) - \Re\{R(\Delta)\}\right] + \sigma_e^2, \tag{3.37}$$

where $\boldsymbol{R}$ *is* $N\times N$ *correlation matrix with the* (i,j)*th entry being* $R(j-i)$ *and* $\mathbf{Z}(\Delta) = \mathbb{E}\left[\boldsymbol{u}(n)h^*(n+\Delta)\right] = [R(-\Delta),\ R(-\Delta-1),\ \cdots,\ R(-\Delta-N+1)]^T$*. Then, we have* $\mathcal{E}_{NP}(\Delta) \geqslant \lim\limits_{n\to\infty} \mathcal{E}_P(\Delta, n)$.

Proof. Since $\tilde{h}(n)$ wide-sense stationary, we have $\mathbb{E}\left[h(n+\tau)h^*(n)\right] = \mathbb{E}\{[\tilde{h}(n+\tau)+e(n+\tau)][\tilde{h}^*(n)+e^*(n)]\} = R(\tau)+\sigma_e^2\delta(\tau)$. According to the strong law of large numbers, we have the following limits:

$$\lim_{n\to\infty} \frac{1}{n-\Delta-N+2} \sum_{k=N-1}^{n-\Delta} \boldsymbol{u}^*(k)\boldsymbol{u}^T(k) = \boldsymbol{R}^* + \sigma_e^2\boldsymbol{I}_N \tag{3.38}$$

and

$$\lim_{n\to\infty} \frac{1}{n-\Delta-N+2} \sum_{k=N-1}^{n-\Delta} \boldsymbol{u}^*(k)h(k+\Delta) = \boldsymbol{Z}^*(\Delta). \tag{3.39}$$

Therefore, based on (3.38) and (3.39), we have

$$\lim_{n\to\infty} \boldsymbol{W}(n) = \overline{\boldsymbol{W}} = ((\boldsymbol{R}+\sigma_e^2\boldsymbol{I}_N)^{-1}\mathbf{Z}(\Delta))^* \tag{3.40}$$

and the prediction error is given as

$$\begin{aligned}\lim_{n\to\infty} \mathcal{E}_P(\Delta, n) &= \mathbb{E}\|\tilde{h}(n+\Delta) - \boldsymbol{u}^T(n)\overline{\boldsymbol{W}}\|^2 \\ &= R(0) - \mathbf{Z}(\Delta)^H(\boldsymbol{R}+\sigma_e^2\boldsymbol{I}_N)^{-1}\mathbf{Z}(\Delta).\end{aligned} \tag{3.41}$$

For comparison purposes, we consider the MSE without channel prediction. The corresponding error is given as

$$\begin{aligned}\mathcal{E}_{NP}(\Delta) &= \mathbb{E}\|\tilde{h}(n+\Delta) - h(n)\|^2 \\ &= 2\left[R(0) - \Re\{R(\Delta)\}\right] + \sigma_e^2.\end{aligned} \tag{3.42}$$

It can be readily verified that $\mathbb{E}[\tilde{h}(n+\Delta) - \boldsymbol{u}^T(n)\overline{\boldsymbol{W}}]\boldsymbol{u}^*(n) = 0$. Therefore,

$$\begin{aligned}\mathcal{E}_{NP}(\Delta) &= \mathbb{E}\|\tilde{h}(n+\Delta) - \boldsymbol{u}^T(n)\overline{\boldsymbol{W}} + \boldsymbol{u}^T(n)\overline{\boldsymbol{W}} - h(n)\|^2 \\ &= \mathbb{E}\|\tilde{h}(n+\Delta) - \boldsymbol{u}^T(n)\overline{\boldsymbol{W}}\|^2 + \mathbb{E}\|\boldsymbol{u}^T(n)\overline{\boldsymbol{W}} - h(n)\|^2 \\ &\geqslant \lim_{n\to\infty} \mathcal{E}_P(\Delta, n),\end{aligned} \tag{3.43}$$

where the equality holds if and only if $\Delta = 0$. □

Theorem 3.2 demonstrates that through channel prediction, the channel variation can be compensated. The effects of Δ and σ_e^2 are illustrated in Sect. 3.5.2.

3.3.3 Prediction Advance Factor

Δ is an important factor that needs to be carefully designed. Consider a DL system with transmission distance d. Then, it takes CSI d/c seconds to be fed back to the transmitter, and after power allocation according to received CSI at the source, it takes the newly generated OFDM symbol d/c seconds to arrive at the receiver. Therefore, the prediction advance time equals to the round-trip time $2d/c$ for the DL system, which implies $\Delta = \lfloor \frac{2d}{cT'} \rfloor$. For RA-UAC, as seen in Fig. 3.2, the relay has to feed back predicted *S-R* CSI to the source, and the destination has to feed back predicted *R-D* CSI to both the source and the relay. Similar to the DL system, it can be readily obtained that $\Delta = \lfloor \frac{2d_1}{cT'} \rfloor$ for channel prediction performed at the relay. At the destination, there are two cases. For predicted *R-D* CSI for the relay, $\Delta = \lfloor \frac{2d_2}{cT'} \rfloor$, and for predicted *R-D* CSI for the source, $\Delta = \left\lfloor \frac{2(d_1+d_2)+ct_p}{cT'} \right\rfloor$ where t_p is the signal processing delay at the relay.

3.3.4 RLS Algorithm

Equation (3.34) is the optimal solution for the least-squares estimation problem. However, its implementation is not practical due to the high computational cost $O(nN^2 + N^3)$ and the large storage size $O(nN)$. The RLS algorithm is the recursive version of (3.34) and facilitates implementation as it has less computational cost $O(N^3)$ and requires very small storage size $O(N^2)$. The RLS algorithm is summarized in Algorithm 1. The least square estimation, namely, (3.34), is utilized to initialize $\boldsymbol{W}(n_0)$. We choose $n_0 = 2N - 2 + \Delta$ such that $\boldsymbol{A}(n_0)$ is a square matrix. It is worth noticing that if there is a strong correlation among channel taps, joint prediction is suggested [4]. Then, to predict $h_l(nT')$ at time nT', $\boldsymbol{W}(n)$ and $\boldsymbol{u}(n)$ of (3.32) have to be modified as $\boldsymbol{W}(n) = [W_0(n), W_1(n), \cdots, W_{N\times L_{nz}-1}(n)]^T$ and $\boldsymbol{u}(n) = [\boldsymbol{u}_{l_0}^T(n), \boldsymbol{u}_{l_1}^T(n), \cdots \boldsymbol{u}_{l_{L_{nz}-1}}^T(n)]^T$ where $\boldsymbol{u}_l(n) = [h_l(nT'), h_l((n-1)T'), \cdots, h_l((n-N+1)T')]^T, l \in \{l_0, \cdots, l_{L_{nz}-1}\}$.

Algorithm 1: RLS algorithm

Initialization: $n_0 = 2N - 2 + \Delta$, $\boldsymbol{P}_{n_0} = \left[\boldsymbol{A}^H(n_0)\boldsymbol{\Lambda}^2(n_0)\boldsymbol{A}(n_0)\right]^{-1}$ and $\boldsymbol{W}(n_0) = \boldsymbol{A}(n_0)^{-1}\boldsymbol{b}(n_0)$;
for $n = n_0 + 1, n_0 + 2, \cdots$ **do**
  For each newly obtained CSI $h(n)$, $\boldsymbol{P}_n$ and $\boldsymbol{W}(n)$ are updated as follows:
  Step 1: $\boldsymbol{a}_n = \boldsymbol{u}^*(n - \Delta)$;
  Step 2: $\boldsymbol{P}_n = \frac{1}{\lambda}\boldsymbol{P}_{n-1} - \frac{\boldsymbol{P}_{n-1}\boldsymbol{a}_n\boldsymbol{a}_n^H\boldsymbol{P}_{n-1}}{\lambda^2+\lambda\boldsymbol{a}_n^H\boldsymbol{P}_{n-1}\boldsymbol{a}_n}$;
  Step 3: $\boldsymbol{W}(n) = \boldsymbol{W}(n-1) + \boldsymbol{P}_n\boldsymbol{a}_n(h(n) - \boldsymbol{a}_n^H\boldsymbol{W}(n-1))$;
  Step 4: Channel prediction $\hat{h}(n + \Delta) = \boldsymbol{h}^T(n)\boldsymbol{W}(n)$;
end

Algorithm 2: Lloyd algorithm

Input: Channel distribution $Pr(\cdot)$;
Initialization: Given the number of quantization bits b, randomly draw $M = 2^b$ independent channel impulse response samples, i.e., $\boldsymbol{h}_i, i \in \{1, 2, \cdots, M\}$;
Step 1: Partition $\mathbb{C}^L$ into M regions, with region $i, i \in \{1, 2, \cdots, M\}$ defined as $R_i = \{\boldsymbol{h} : \|\boldsymbol{h} - \boldsymbol{h}_i\| \leqslant \|\boldsymbol{h} - \boldsymbol{h}_j\|, \boldsymbol{h} \in \mathbb{C}^L, \forall j \neq i\}$;
Step 2: Update the centroid of each region:

$$\boldsymbol{h}_i' = \frac{\int_{R_i} \boldsymbol{h} Pr(\boldsymbol{h}) d\boldsymbol{h}}{\int_{R_i} Pr(\boldsymbol{h}) d\boldsymbol{h}}, i \in \{1, 2, \cdots, M\}; \tag{3.44}$$

Step 3: Go back to Step 1 and assign $\boldsymbol{h}_i = \boldsymbol{h}_i'$ until $\|\boldsymbol{h}_i' - \boldsymbol{h}_i\| < \varepsilon, i \in \{1, 2, \cdots, M\}$ holds for some predefined tolerance ε;
Step 4: The Lloyd quantizer is given as

$$\mathcal{Q}(\boldsymbol{h}) = \arg \min_{i \in \{1,2,\cdots,M\}} \|\boldsymbol{h} - \boldsymbol{h}_i'\|. \tag{3.45}$$

3.4 Channel Quantization

Due to the limited bandwidth of UWA channels, full CSI feedback would consume a substantial amount of channel resources and degrade the overall system performance substantially. Therefore, we consider low-rate limited feedback. We adopt the Lloyd's algorithm for CSI quantization as it is beneficial when the signal distribution is nonuniform [6].

The Lloyd algorithm is given in Algorithm 2, where the channel impulse response in the TD is quantized. The practical implementation of the Lloyd algorithm requires the relay and the destination to collect a sufficient number of *S-R* and *R-D* channel samples, respectively, and Step 2 can be realized by calculating the average of all channel samples assigned to a region as its centroid. After obtaining the Lloyd quantizer, the relay sends its codebook $\boldsymbol{h}_{i,R}', i \in \{1, 2, \cdots, M\}$ to the source, and the destination sends its codebook $\boldsymbol{h}_{i,D}', i \in \{1, 2, \cdots, M\}$ to both the source and the relay. One assumption about the Lloyd algorithm is that node positions are fixed such that the channel distribution $Pr(\cdot)$ is unchanged. If the channel distribution changes substantially, the Lloyd algorithm needs to be rerun, and the codebook at relevant nodes should also be updated.

3.5 Performance Evaluations

In the following, the empirical UWA channel model and the statistical time-varying UWA channel model in Chap. 2 are utilized to evaluate the performance of the adaptive RA-UAC system.

3.5.1 Capacity Analysis for Empirical UWA Channel Model

In this section, the empirical UWA channel model in Sect. 2.1 is utilized. The empirical UWA channel model facilitates the generation of pass loss at any propagation distances. Thus, it is ideal to investigate the optimal power allocation and the effect of relay location.

3.5.1.1 System Setup

The maximum transmit power for each node is chosen to be $\mathcal{P}_{M_S} = \mathcal{P}_{M_R} = \mathcal{P}_M = 100\,\text{dB re }\mu\text{Pa}$ over the signal frequency band $10 - 30\,\text{kHz}$. The total number of subcarriers is 1024 with subcarrier spacing 19.5 Hz. We assume full CSI available at the source and the relay. We also consider the DL-UAC system for comparison.

3.5.1.2 Effect of Transmission Distances

With $\mathcal{P}_T = \mathcal{P}_M = 100\,\text{dB re }\mu\text{Pa}$, the system capacities of both AF-based RA-UAC and DL-UAC with the uniform and optimal power allocations are shown in Fig. 3.3. For RA-UAC, we choose $d_1 = d_2$. From Fig. 3.3, as expected, AF-based RA-UAC with the optimal power allocation has higher capacity than AF-based RA-UAC with the uniform power allocation, and the difference between the upper bound and the lower bound is negligible. Since the upper bound and the lower bound are tight, as suggested in Sect. 3.2, we simply use $\mathcal{P}_S^l(f)$ and $\mathcal{P}_R^l(f)$ as the optimal power allocation for AF-based RA-UAC. In addition, AF-based RA-UAC has higher capacity than DL-UAC at long transmission distances for both the uniform and optimal power allocations.

3.5.1.3 Effect of Relay Location and Transmit Power

The relay location affects the end-to-end SNR and further influences the capacity of AF-based RA-UAC and the optimal power allocation between the source and the relay. To facilitate the analysis of the effect of relay location, we define the relay location ratio α_D as the ratio of *S-R* distance d_1 to overall distance $d_1 + d_2$, i.e., $\alpha_D = d_1/(d_1 + d_2)$ and $1 - \alpha_D = d_2/(d_1 + d_2)$. Likewise, the power allocation ratio α_P is defined as the portion of source transmit power $\mathcal{P}_S$ out of total transmit power $\mathcal{P}$, i.e., $\alpha_P = \mathcal{P}_S/\mathcal{P}_T$ and $1 - \alpha_P = \mathcal{P}_R/\mathcal{P}_T$ where $\mathcal{P}_S = \sum_{k=1}^{K} \mathcal{P}_S^l(f_k)$ and $\mathcal{P}_R = \sum_{k=1}^{K} \mathcal{P}_R^l(f_k)$. Total transmit power also plays an important role in the power allocation between the source and the relay. Therefore, it is also investigated.

For a communication distance $d_1 + d_2 = 6\,\text{km}$ and individual transmit power constraint $\mathcal{P}_M = 100\,\text{dB re }\mu\text{Pa}$, we calculate the capacity of AF-based RA-UAC for different relay location ratios and total transmit power $\mathcal{P}_T$. The results are plotted

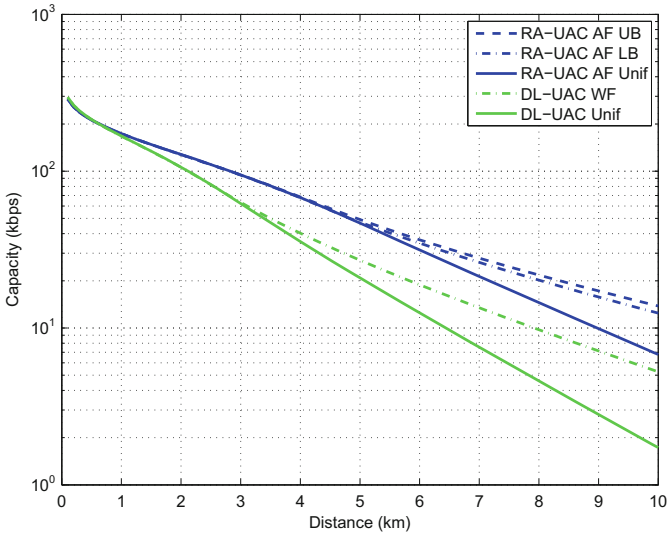

Fig. 3.3 The system capacities of the AF-based RA-UAC systems with different transmission distances $d_1 + d_2$. The system capacities of the DL-UAC systems with the uniform power allocation (Unif) and the optimal power allocation using water-filling (WF) are also provided

in Fig. 3.4. It is found that the RA-UAC system with the optimal power allocation has larger capacity than the system with the uniform power allocation at all α_D, and the highest system capacity is achieved with $\alpha_D = 1/2$. As expected, the capacity of RA-UAC increases with $\mathcal{P}_T$ in Fig. 3.4. This implies the system capacity can be adjusted by changing $\mathcal{P}_T$. In addition, to gain some insights on the optimal power allocation for RA-UAC with different relay locations and total transmit power, we plot the optimal power allocation ratio α_P with respect to α_D in Fig. 3.5. It can be seen that when $\mathcal{P}_T = \mathcal{P}_M$, where the individual power constraints, i.e., (3.5), are always met, the optimal power allocation ratio α_P is an increasing function of the relay location ratio α_D. Notice from (3.1), the end-to-end SNR of an AF relaying system is dominated by the worse SNR between the *S-R* link and the *R-D* link. Thus, the balanced link quality provides the optimal system performance. When $\mathcal{P}_T = 1.5\mathcal{P}_M$, the cutoff is observed when the relay is close to the source or the destination. This is due to the effect of the individual power constraint. Furthermore, when $\mathcal{P}_T = 2\mathcal{P}_M$, to achieve the maximum system capacity, the source and the relay has to transmit using the maximum power $\mathcal{P}_M$. Although transmit power is fixed at each node, as observed in Fig. 3.4, the larger system capacity is achieved through optimal power distribution over subcarriers compared with the uniform power distribution for all α_D.

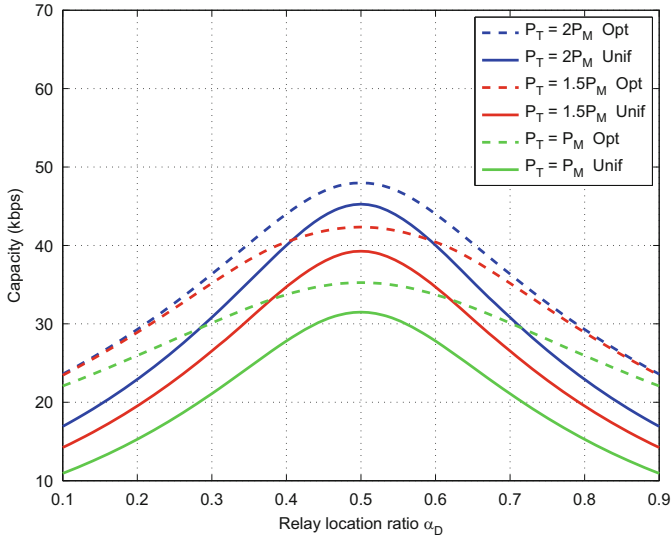

Fig. 3.4 The AF-based RA-UAC system capacities with respect to α_D and $\mathcal{P}_T$ for a transmission distance $d_1 + d_2 = 6\,\text{km}$

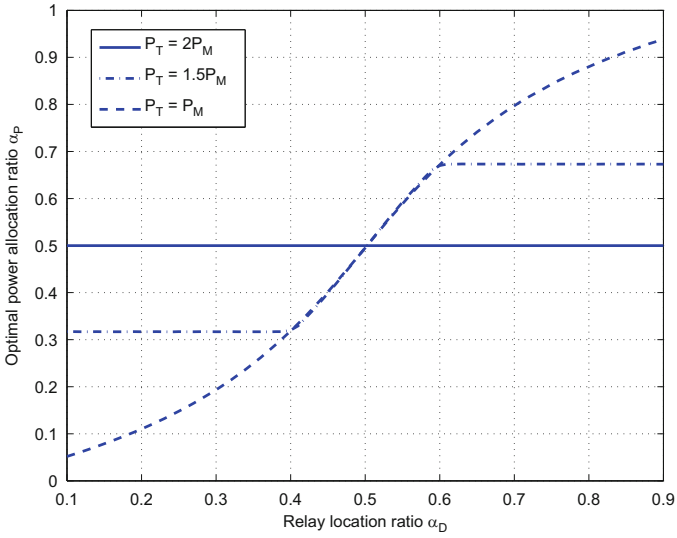

Fig. 3.5 The optimal power allocation ratio α_P with respect to α_D and $\mathcal{P}_T$

3.5.2 *Capacity Analysis for Statistical Time-Varying UWA Channel Model*

The statistical time-varying UWA channel can capture the multipath and time-varying features of UWA channels, and it is suitable for studying the effects of channel prediction and quantization and evaluating overall system performance. Therefore, in this section, the effects of channel prediction and channel quantization and overall system performance at different transmission distances are revealed using the statistical time-varying UWA channel model in Sect. 2.2.

3.5.2.1 System Setup

To model the long-term path loss, the Bellhop software [7] is utilized. It is a publicly available acoustic ray-tracing program. Given a sound profile and the sea geometric description, the Bellhop software produces the amplitude, the phase, and the propagation time of each signal arrival. Based on the TD quantization of the software output, a deterministic discrete-time UWA channel $\bar{\boldsymbol{h}}$ is generated. We use the sound profile from the MACE'10 experiment as the input for the Bellhop software [8].

The basic system parameters are provided in Table 3.1. All generated channel impulse responses are normalized by the DL channel gain at 1500 m. The window size of the RLS adaptive filter is set as $N = 10$. Practically, it is suggested to choose $N = \arg\min_{N_0} \sup_{|n|\geq N_0} [R(T'n, l)/|\bar{h}_l|^2] < \varepsilon$ for a nonzero tap $\tilde{h}_l$ to fully utilize channel correlation information. Without loss of generality of the proposed adaptive RA-UAC system, we assume that the additive noise at each subcarrier is white Gaussian with unit variance. We also assume that the node positions are stable and the channel statistics does not change.

Table 3.1 System parameters

Water depth	110 m
Nodes depth	100 m
Signal bandwidth	12 kHz
Carrier frequency	17 kHz
Number of total subcarriers	2048
Subcarrier spacing	5.88 Hz
OFDM symbol duration	170 ms
Guard interval	80 ms
Maximum Doppler shift	0.3 Hz

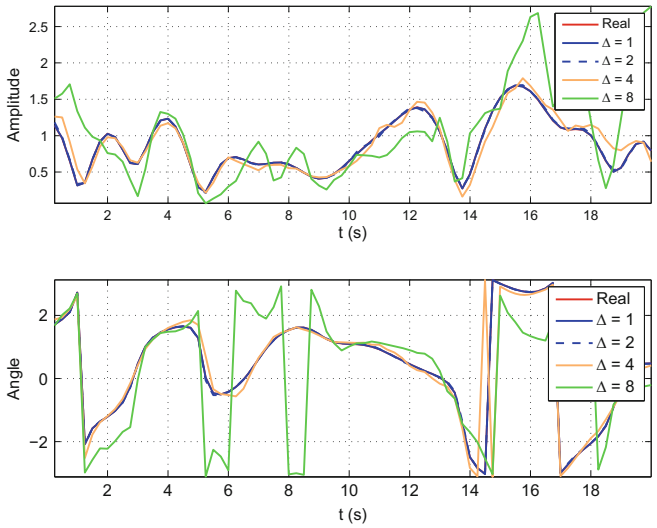

Fig. 3.6 The curve of channel prediction for different values of Δ. $\lambda = 0.75$ and $\sigma_e^2 = 0$

3.5.2.2 Effect of Channel Prediction

Figure 3.6 plots the channel prediction curves in the TD with different values of Δ for a channel tap with unit power. The forgetting factor λ is 0.75, and σ_e^2 is set as 0. The values of Δ, i.e., 1, 2, 4, and 8, correspond to DL transmission distances 188 m, 375 m, 750 m, and 1500 m, respectively. From the figure, it is shown that the RLS adaptive filter gives a good tracking of the channel variation, especially when Δ is small. To quantify the effects of Δ and λ, the MSE with different values of Δ and λ is plotted in Fig. 3.7. We also plot the theoretical MSE using (3.36). From Fig. 3.7, we have the following observations. (1) The MSE curve with $\lambda = 1$ coincides with the theoretical MSE curve. (2) The MSE becomes higher for $\lambda < 1$. This is because with $\lambda < 1$, the older channel samples are weighted less and their channel statistic information is not fully utilized. Therefore, when the channel statistics is stationary, the optimal value of λ is 1. However, for UWA channels, where the channel statistics could change over time, it is suggested to choose λ as $1 - 1/L$. L is the number of OFDM symbols within which the channel tap changing over time can be treated as a stationary process. (3) It can be observed that the MSE with channel prediction is much smaller than the MSE without channel prediction. This confirms the necessity of channel prediction. (4) The MSE increases with Δ. This implies that channel prediction is more accurate for short transmission distances. Moreover, in Fig. 3.8, the effect of σ_e^2, namely, the variance of the channel estimation error, is investigated. It can be observed the MSE increases with σ_e^2, which shows large σ_e^2 harms the performance of channel prediction.

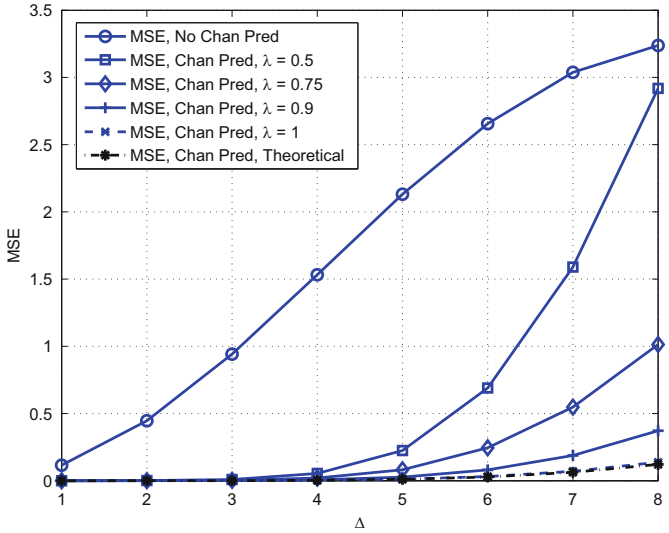

Fig. 3.7 MSE with different values of λ and Δ. $\sigma_e^2 = 0$

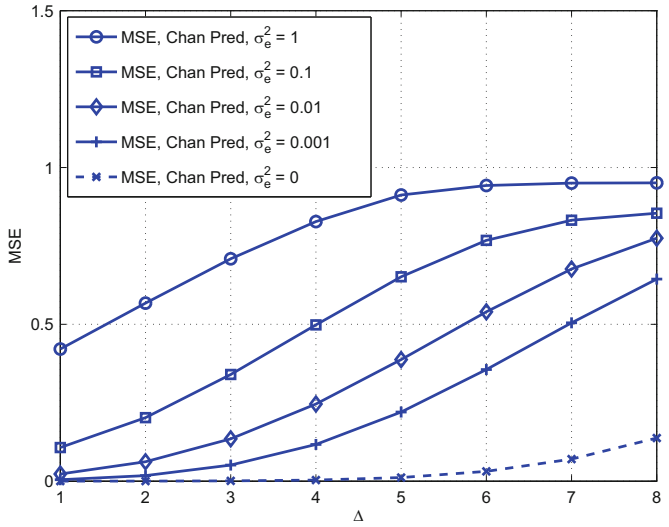

Fig. 3.8 MSE with different values of σ_e^2 and Δ. $\lambda = 1$

3.5.2.3 Effect of Transmission Distances

The system capacities of RA-UAC with distances $d_1 = d_2 = 400\,\text{m}$, 800 m, and 1500 m are illustrated in Figs. 3.9, 3.10, and 3.11, respectively. The system capacity is averaged over 50 s. The system parameters are $\lambda = 0.75$, $t_p = 0$, and $\sigma_e^2 = 0$.

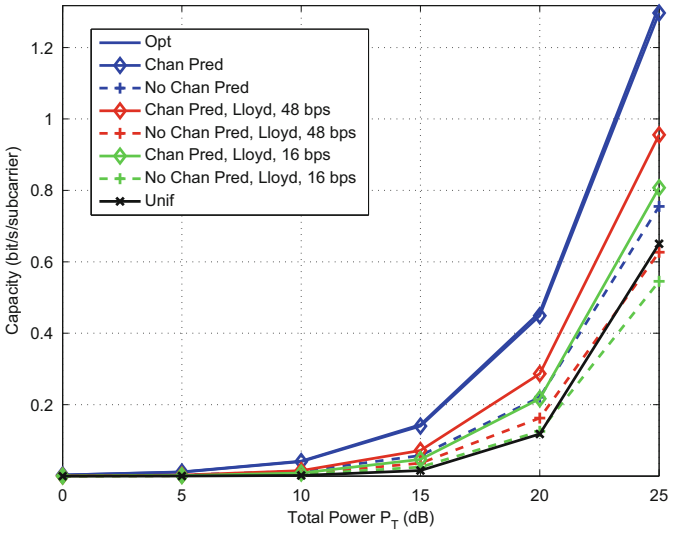

Fig. 3.9 System capacities of RA-UAC systems with transmission distances $d_1 = d_2 = 400\,\text{m}$

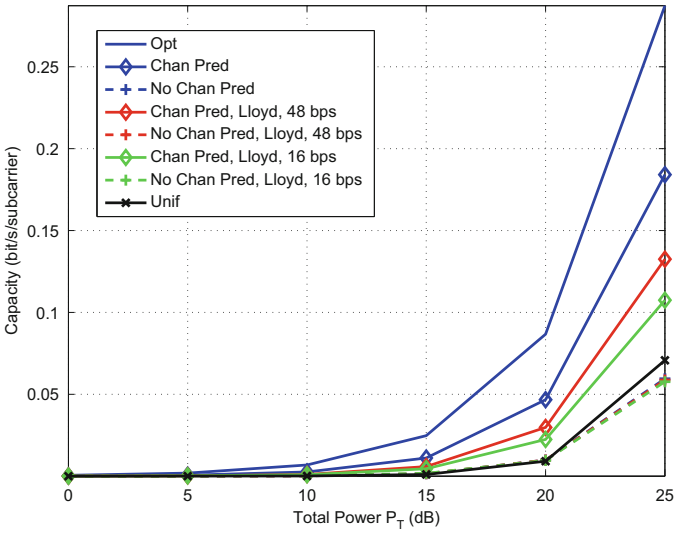

Fig. 3.10 System capacities of RA-UAC systems with transmission distances $d_1 = d_2 = 800\,\text{m}$

In the figures, eight RA-UAC schemes are considered. The first scheme is the ideal case, i.e., the red solid line, where the source and the relay have full future CSI. It is observed that this scheme provides the largest capacity that an adaptive RA-UAC system can achieve. For the second scheme and the third scheme, i.e., the blue solid line and the blue dashed line, the source and the relay obtain their CSI

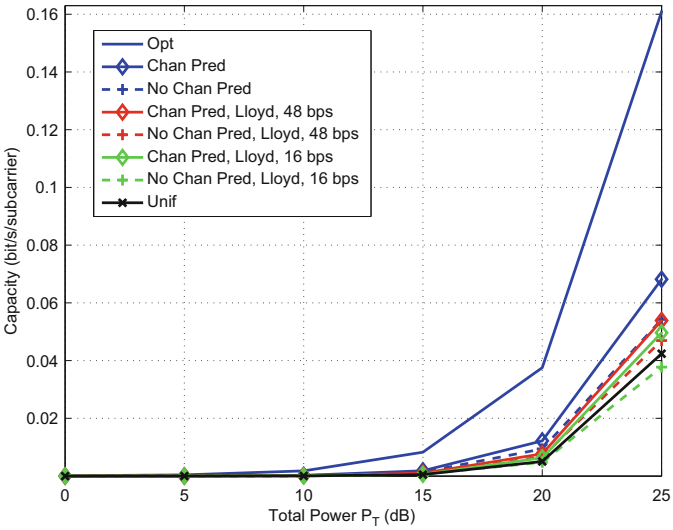

Fig. 3.11 System capacities of RA-UAC systems with transmission distances $d_1 = d_2 = 1500\,\text{m}$

through the perfect channel feedback. Their difference comes from whether channel is predicted or not. It is found that without channel prediction, the performance of the third scheme degrades a lot compared with the first scheme, especially at long transmission distances, i.e., 800 m and 1500 m. This is because without channel prediction, the channel variation makes received CSI outdated, and the power allocation calculated at the source and the relay is not accurate. The second scheme which implements channel prediction has much better performance than the third scheme as the power allocation calculated at the source and the relay is more accurate based on the predicted CSI feedback. The fourth and fifth schemes, i.e., the cyan solid line and the cyan dashed line, implement the Lloyd quantizer with quantization bits number $b = 6$ per OFDM symbol. The corresponding feedback rate is $2 \times b/T' = 48\,\text{bps}$. The sixth and seventh schemes, i.e., the green solid line and the green dashed line, implement the Lloyd quantizer with quantization bits number $b = 2$ per OFDM symbol and the feedback rate is $2 \times b/T' = 16\,\text{bps}$. The last scheme, i.e., the black solid line, is the nonadaptive system with the uniform power allocation as the benchmark. It can be seen that implementing both low-rate Lloyd quantization and channel prediction can realize the benefits of the adaptive RA-UAC system. In addition, we define the system efficiency of a RA-UAC system as $\alpha_{\text{eff}} = \frac{C_{\text{sys}} - C_{\text{unif}}}{C_{\text{opt}} - C_{\text{unif}}}$ to quantify how much portion of the capacity gain of the optimal power allocation over the uniform power allocation is achieved, where C_{opt} and C_{unif} are the system capacities of the first scheme and the last scheme, respectively. The system efficiency of the second, fourth, and sixth schemes with $\mathcal{P} = 20\,\text{dB}$ is plotted in Fig. 3.12. It is found that the adaptive RA-UAC system is more beneficial for the

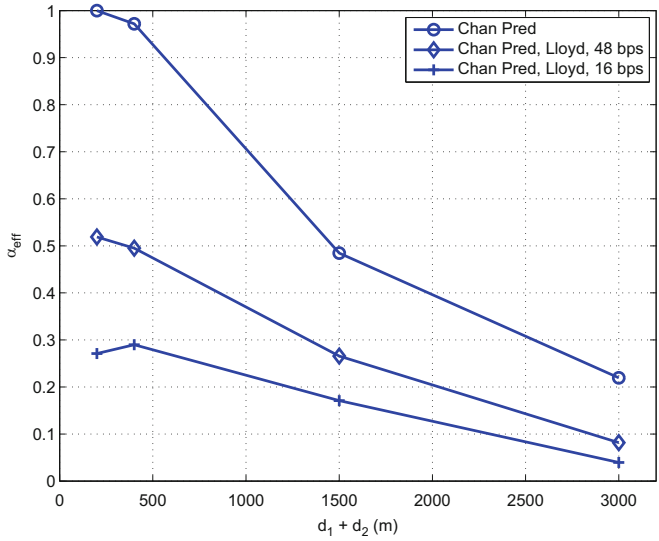

Fig. 3.12 System efficiency

short-range communications due to the channel predictability. For the long-range communications, the benefits of the adaptive system are not obvious, and the uniform power allocation is preferred.

3.6 Summary

In this chapter, we studied the adaptive RA-UAC system to take advantage of the benefits of the optimal power allocation. The key components of our system include the optimal power allocation, channel prediction, and channel quantization. To maximize the system capacity, the optimal power allocation at the source and the relay is derived with individual and total power constraints. The RLS adaptive filter is adopted to predict the future channel impulse response, and its MSE performance is analyzed. To adapt to the band-limited UWA channels, the Lloyd quantizer is utilized to quantize the channel impulse response efficiently. In simulations, the optimal power allocation and the effect of relay location were investigated through the empirical UWA channel model, and the overall performance of the adaptive RA-UAC systems was evaluated through the statistical time-varying UWA channel model. It is found that the performance of the adaptive RA-UAC system without channel prediction degrades a lot compared with the theoretical performance of the optimal power allocation. This is because the calculated power allocation at the source and the relay is not accurate based on the outdated CSI feedback. After implementing channel prediction at the receiving nodes, the calculated power allocation at the source and the relay is more accurate, and the performance of the

adaptive RA-UAC system improves substantially. In addition, it is more beneficial to implement the adaptive system for the short-range transmissions than the long-range transmissions because of the channel predictability.

References

1. R. Cao, F. Qu, L. Yang, On the capacity and system design of relay-aided underwater acoustic communications, in *Proceedings of Wireless Communications and Networking Conference*, Sydney, 18–21 April 2010, pp. 1–6
2. X. Cheng, R. Cao, L. Yang, Relay-aided amplify-and-forward powerline communications. IEEE Trans. Smart Grid **4**(1), 265–272 (2013)
3. E.K.P. Chong, S.H. Zak, *An Introduction to Optimization* (Wiley, New York, 2013)
4. A. Radosevic, R. Ahmed, T.M. Duman, J.G. Proakis, M. Stojanovic, Adaptive OFDM modulation for underwater acoustic communications: design considerations and experimental results. IEEE J. Ocean. Eng. **39**(2), 357–370 (2014)
5. B. Li, S. Zhou, M. Stojanovic, L. Freitag, P. Willett, Multicarrier communication over underwater acoustic channels with nonuniform Doppler shifts. IEEE J. Ocean. Eng. **33**(2), 198–209 (2008)
6. S. Lloyd, Least squares quantization in PCM. IEEE Trans. Inf. Theory **28**(2), 129–137 (1982)
7. M. Porter, Bellhop gaussian beam/finite element beam code. Available in the Acoustics Toolbox (2007), http://oalib.hlsresearch.com/Rays
8. Y.M. Aval, M. Stojanovic, Differentially coherent multichannel detection of acoustic OFDM signals. IEEE J. Ocean. Eng. **40**(2), 251–268 (2014)

Chapter 4
Medium-Long-Range Asynchronous Relay Selection Protocol for RA-UAC

Chapter 3 shows that for short-range UAC, the predicted instantaneous CSI feedback from the receiver to the transmitter can improve system performance considerably. However, as discussed in Sect. 2.3, for medium-long-range UAC, the propagation time of the feedback signal could be much larger than the coherence time and therefore nullify the instantaneous CSI feedback. In this chapter, statistical CSI is considered for the design of the medium-long-range RA-UAC system. We first present the AsAP protocol with instantaneous amplification at the relays and then investigate the power allocation among the source and the relays based on statistical CSI.

4.1 AsAP Protocol

We consider a dual-hop relay system setup with one source node s, R relay nodes $r_i, i \in \{1, \ldots, R\}$, and one destination node d in Fig. 4.1. $\boldsymbol{h}_{i,j}, i, j \in \{s, r, d\}$ represents the zero-padded channel vector between node i and j of length N. The AsAP transmission mainly consists of three stages: source transmitting, relay amplifying and forwarding, and destination decoding. As the instantaneous CSI feedback could be infeasible for medium-long-range UAC, we adopt the uniform power allocation among all the subcarriers for each node.

4.1.1 Source Transmitting

At the source, each generated OFDM symbol $\boldsymbol{x}$ is precoded with grouped linear constellation precoding (GLCP) and then broadcast to the relays and the destination. GLCP consists of two steps: grouping and precoding. The grouping is performed as

X. Cheng et al., *Cooperative OFDM Underwater Acoustic Communications*,
Wireless Networks, DOI 10.1007/978-3-319-33207-9_4

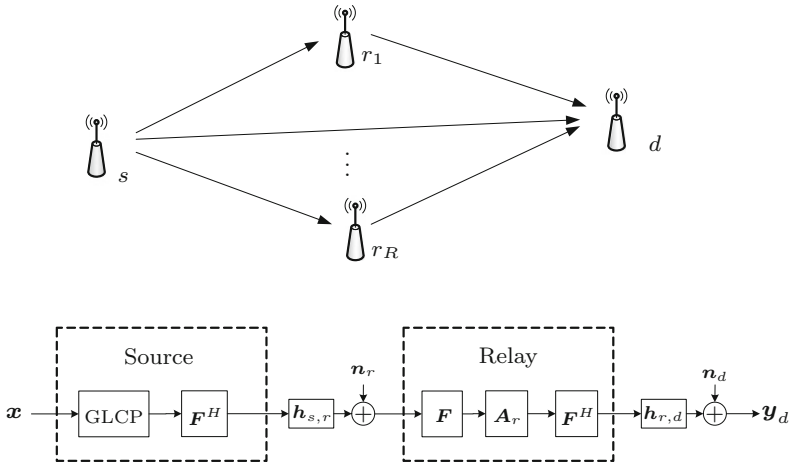

Fig. 4.1 System topology of the AsAP protocol

follows. For a precoding size K, the data symbol $\boldsymbol{x}$ of length $N = K \times M$ with elements chosen from a finite constellation set $\mathcal{A}_N$ is first divided into consecutive K blocks, each of size M, and then the mth ($m \in \{1, \ldots, M\}$) element from each block is selected to form a group, denoted by a vector $\boldsymbol{x}_m$. This procedure can be mathematically represented as $\boldsymbol{x}_m = \boldsymbol{\Psi}_m \boldsymbol{x}$, where $\boldsymbol{\Psi}_m = \boldsymbol{I}_N(\mathcal{S}_m, :)$ is a $K \times N$ selection matrix with K rows chosen from an $N \times N$ identity matrix $\boldsymbol{I}_N$ and the indices of the K rows defined in the set $\mathcal{S}_m$. For optimal grouping, each row set is chosen as $\mathcal{S}_m = \{m, m + M, \cdots, m + (K-1)M\}$. In the second step, each group vector $\boldsymbol{x}_m$ is encoded with the precoder matrix $\boldsymbol{\Theta}$ of size $K \times K$. Then the coded groups are reassembled to form the precoded symbols $\boldsymbol{x}_s$. The entire GLCP process can be presented as

$$\boldsymbol{x}_s = \sum_{m=1}^{M} \boldsymbol{\Psi}_m^T \boldsymbol{\Theta} \boldsymbol{\Psi}_m \boldsymbol{x} = \boldsymbol{\Psi} \boldsymbol{x}, \tag{4.1}$$

where $\boldsymbol{\Psi} = \sum_{m=1}^{M} \boldsymbol{\Psi}_m^T \boldsymbol{\Theta} \boldsymbol{\Psi}_m$.

We choose $\boldsymbol{\Theta}$, which maximizes the multipath diversity and the coding gain [1]:

$$\boldsymbol{\Theta} = \frac{1}{\beta} \begin{bmatrix} 1 & \alpha_1 & \alpha_1^2 & \cdots & \alpha_1^{K-1} \\ 1 & \alpha_2 & \alpha_2^2 & \cdots & \alpha_2^{K-1} \\ \vdots & \vdots & \vdots & \ddots & \vdots \\ 1 & \alpha_K & \alpha_K^2 & \cdots & \alpha_K^{K-1} \end{bmatrix}, \tag{4.2}$$

where β is the normalization factor such that $\mathrm{tr}\{\boldsymbol{\Theta}^H \boldsymbol{\Theta}\} = K$ and the values of $\alpha_1, \cdots, \alpha_K$ are given in [1].

To overcome ISI, a cyclic prefix (CP) is inserted after taking the inverse fast Fourier transform (IFFT) of $\boldsymbol{x}_s$. Then the generated TD symbol is broadcast to the relays and the destination with transmit power $\mathcal{P}_s$ at each subcarrier.

4.1.2 Relay Amplifying and Forwarding

After receiving the signals from the source, each relay removes the major Doppler effect through received signal resampling and CFO compensation. In FD amplification, after normal CP removal and fast Fourier transform (FFT), the FD signals received by relay r_i is represented as

$$\boldsymbol{y}_{r_i} = \boldsymbol{H}_{s,r_i}\sqrt{\mathcal{P}_s}\boldsymbol{x}_s + \boldsymbol{n}_{r_i}, \tag{4.3}$$

where $\boldsymbol{H}_{s,r_i} = \sqrt{N}\text{diag}(\boldsymbol{F}_N\boldsymbol{h}_{s,r_i})$ is the diagonal S-R FD channel matrix and $\boldsymbol{n}_{r_i}$ is the independent and identically distributed (i.i.d.) FD noise vector, i.e., $\boldsymbol{n}_{r_i} \sim \mathcal{CN}(0, \sigma_{r_i}^2\boldsymbol{I}_N)$. $\boldsymbol{F}_N$ is $N \times N$ DFT matrix with $\boldsymbol{F}_N\boldsymbol{F}_N^H = \boldsymbol{I}_N$.

FD amplification is performed as $\boldsymbol{x}_{r_i} = \boldsymbol{A}_{r_i}\boldsymbol{y}_{r_i}$. The amplification factor $\boldsymbol{A}_{r_i}$ is a diagonal matrix with the amplification magnitude for each subcarrier as the diagonal entries. The amplification magnitude values are chosen to assure that the relaying signal power complies with the relay transmit power constraint $\mathcal{P}_{r_i}$. There are two ways of amplification, i.e., fixed amplification and instantaneous amplification. Fixed amplification meets the power constraint in the long-term rather than the short-term and can result in the power overload when the S-R signal is strong. Therefore, to ensure the power constraint in the short-term, instantaneous FD amplification is chosen. Suppose that the power constraint is imposed on each subcarrier k, i.e., $\mathbb{E}|\boldsymbol{A}_{r_i}(k,k)\boldsymbol{y}_{r_i}(k)|^2 = \mathcal{P}_{r_i}$ and $\boldsymbol{H}_{s,r_i}$ is known at the relays through channel estimation. The instantaneous amplification factor is obtained as

$$\boldsymbol{A}_{r_i,\text{inst}} = \sqrt{\frac{\mathcal{P}_{r_i}}{|\boldsymbol{H}_{s,r_i}|^2\mathcal{P}_s + \sigma_{r_i}^2\boldsymbol{I}_N}}. \tag{4.4}$$

After amplification, the TD signal is generated by performing IFFT of $\boldsymbol{A}_{r_i}\boldsymbol{y}_{r_i}$ and inserting CP. All relays forward the signals to the destination asynchronously.

4.1.3 Destination Decoding

At the destination, similar to the relays, the major Doppler effect is removed through received signal resampling and CFO compensation. As elaborated in Sect. 4.3, through careful protocol design, the DL and RL signals are received at different time without interference. After CP removal and FFT, the DL signal received is

represented as

$$\boldsymbol{y}_d^{(1)} = \boldsymbol{H}_{s,d}\sqrt{\mathcal{P}_s}\boldsymbol{x}_s + \boldsymbol{n}_d^{(1)}, \tag{4.5}$$

where $\boldsymbol{H}_{s,d} = \sqrt{N}\text{diag}(\boldsymbol{F}_N\boldsymbol{h}_{s,d})$ is the diagonal source-to-destination (S-D) FD channel matrix and $\boldsymbol{n}_d^{(1)} \sim \mathcal{CN}(0, \boldsymbol{\Delta}_d)$ is the FD noise at the destination with covariance matrix $\boldsymbol{\Delta}_d = \sigma_d^2\boldsymbol{I}_N$. The RL signals received at the destination are superimposed as

$$\begin{aligned}\boldsymbol{y}_d^{(2)} &= \sum_{i=1}^{R}\boldsymbol{H}_{r_i,d}\boldsymbol{A}_{r_i}\boldsymbol{y}_{r_i} + \boldsymbol{n}_d^{(2)} \\ &= \boldsymbol{H}_{\text{eq}}\sqrt{\mathcal{P}_s}\boldsymbol{x}_s + \boldsymbol{n}_{\text{eq}},\end{aligned} \tag{4.6}$$

where $\boldsymbol{H}_{r_i,d} = \sqrt{N}\text{diag}(\boldsymbol{F}_N\boldsymbol{h}_{r_i,d})$ is the diagonal R-D FD channel matrix, $\boldsymbol{n}_d^{(2)} \sim \mathcal{CN}(0, \boldsymbol{\Delta}_d)$ is the FD noise vector at the destination, $\boldsymbol{H}_{\text{eq}}$ is the equivalent end-to-end FD channel matrix computed as $\boldsymbol{H}_{\text{eq}} = \sum_{i=1}^{R}\boldsymbol{H}_{r_i,d}\boldsymbol{A}_{r_i}\boldsymbol{H}_{s,r_i}$, and $\boldsymbol{n}_{\text{eq}}$ is the equivalent FD noise vector computed as $\boldsymbol{n}_{\text{eq}} = \boldsymbol{n}_d^{(2)} + \sum_{i=1}^{R}\boldsymbol{H}_{r_i,d}\boldsymbol{A}_{r_i}\boldsymbol{n}_{r_i}$. In addition, $\boldsymbol{n}_{\text{eq}}$ is colored with covariance matrix $\boldsymbol{\Delta}_{\text{eq}} = \sigma_d^2\boldsymbol{I}_N + \sum_{i=1}^{R}|\sigma_{r_i}\boldsymbol{H}_{r_i,d}\boldsymbol{A}_{r_i}|^2$.

Different from the original AsAP protocol, where $\boldsymbol{y}_d^{(1)}$ and $\boldsymbol{y}_d^{(2)}$ are simply added together, we combine $\boldsymbol{y}_d^{(1)}$ and $\boldsymbol{y}_d^{(2)}$ using MRC to collect delay diversity. Define $\boldsymbol{y}_d = [(\boldsymbol{y}_d^{(1)})^T\ (\boldsymbol{y}_d^{(2)})^T]^T$, $\boldsymbol{\gamma} = \mathcal{P}_s\boldsymbol{H}_{s,d}^H\boldsymbol{\Delta}_d^{-1}\boldsymbol{H}_{s,d} + \mathcal{P}_s\boldsymbol{H}_{\text{eq}}^H\boldsymbol{\Delta}_{\text{eq}}^{-1}\boldsymbol{H}_{\text{eq}}$ whose diagonal entries represent SNR at the subcarriers, and $\boldsymbol{\Lambda} = [(\boldsymbol{H}_{s,d}\sqrt{\mathcal{P}_s})^H\boldsymbol{\Delta}_d^{-1}\ \ (\boldsymbol{H}_{\text{eq}}\sqrt{\mathcal{P}_s})^H\boldsymbol{\Delta}_{\text{eq}}^{-1}]$. Then the combination of $\boldsymbol{y}_d^{(1)}$ and $\boldsymbol{y}_d^{(2)}$ is given as

$$\begin{aligned}\bar{\boldsymbol{y}}_d &= \boldsymbol{\gamma}^{-1/2}\boldsymbol{\Lambda}\boldsymbol{y}_d \\ &= \boldsymbol{\gamma}^{-1/2}(\boldsymbol{H}_{s,d}\sqrt{\mathcal{P}_s})^H\boldsymbol{\Delta}_d^{-1}\boldsymbol{y}_d^{(1)} + \boldsymbol{\gamma}^{-1/2}(\boldsymbol{H}_{\text{eq}}\sqrt{\mathcal{P}_s})^H\boldsymbol{\Delta}_{\text{eq}}^{-1}\boldsymbol{y}_d^{(2)} \\ &= \boldsymbol{\gamma}^{1/2}\boldsymbol{x}_s + \boldsymbol{\gamma}^{-1/2}(\boldsymbol{H}_{s,d}\sqrt{\mathcal{P}_s})^H\boldsymbol{\Delta}_d^{-1}\boldsymbol{n}_d^{(1)} + \boldsymbol{\gamma}^{-1/2}(\boldsymbol{H}_{\text{eq}}\sqrt{\mathcal{P}_s})^H\boldsymbol{\Delta}_{\text{eq}}^{-1}\boldsymbol{n}_{\text{eq}} \\ &= \boldsymbol{\gamma}^{-1/2}\boldsymbol{x}_s + \boldsymbol{n},\end{aligned} \tag{4.7}$$

where $\boldsymbol{n}$ is the normalized noise vector, i.e., $\boldsymbol{n} \sim \mathcal{CN}(0, \boldsymbol{I}_N)$.

The symbol detector at the destination estimates the transmitted data in each group. The K data symbols in group m, $m \in \{1, \ldots, M\}$, are decoded together with the optimal maximum likelihood (ML) criterion:

$$\boldsymbol{x}_m = \arg\min_{\boldsymbol{x}_i \in \mathcal{A}_K} \|\boldsymbol{\Psi}_m\bar{\boldsymbol{y}}_d - \boldsymbol{\Psi}_m\boldsymbol{\gamma}^{1/2}\boldsymbol{\Psi}_m^T\boldsymbol{\Theta}\boldsymbol{x}_i\|^2. \tag{4.8}$$

4.2 Power Allocation Based on Statistical CSI

For the original AsAP protocol, all relays participate in communications, and the transmit power is uniformly allocated among the source and the relays, i.e., $\mathcal{P}_{r_i} = \mathcal{P}_s = P_{\text{tot}}/(R+1)$. Although it has been verified that the AsAP protocol with the uniform power allocation outperforms single-hop communications, its performance can be further improved through the transmit power allocation among the source and the relays. As seen in Sect. 2.3, the instantaneous CSI feedback could be infeasible for UAC. We choose to optimize the average received SNR at the destination based on statistical CSI, which is closely related to the end-to-end performance.

The instantaneous SNR at subcarrier $k, k \in 1, \cdots, N$, is γ_k, where

$$\gamma_k = \frac{\mathcal{P}_s \left| \sum_{i=1}^{R} \frac{\sqrt{\mathcal{P}_{r_i}} \boldsymbol{H}_{s,r_i}(k,k) \boldsymbol{H}_{r_i,d}(k,k)}{\sqrt{|\boldsymbol{H}_{s,r_i}(k,k)|^2 \mathcal{P}_s + \sigma_{r_i}^2}} \right|^2}{\sum_{i=1}^{R} \left| \frac{\sqrt{\mathcal{P}_{r_i}} \boldsymbol{H}_{r_i,d}(k,k)}{\sqrt{|\boldsymbol{H}_{s,r_i}(k,k)|^2 \mathcal{P}_s + \sigma_{r_i}^2}} \right|^2 \sigma_{r_i}^2 + \sigma_d^2} + \frac{\mathcal{P}_s |\boldsymbol{H}_{s,d}(k,k)|^2}{\sigma_d^2}. \tag{4.9}$$

The average SNR can be calculated by averaging the above instantaneous SNR expression over the distribution of the channel gains. However, the closed-form solution of the average SNR using multiple integral is mathematically intractable. Thus, an approximate average SNR expression can be derived by taking the average of the numerator and the denominator of (4.9) separately. As it is a good predictor of the average SNR [2], the approximate average SNR is utilized. The approximate average SNR at subcarrier k is given as

$$\overline{\gamma}_k = \frac{\mathbb{E}\left[\mathcal{P}_s \left| \sum_{i=1}^{R} \frac{\sqrt{\mathcal{P}_{r_i}} \boldsymbol{H}_{s,r_i}(k,k) \boldsymbol{H}_{r_i,d}(k,k)}{\sqrt{|\boldsymbol{H}_{s,r_i}(k,k)|^2 \mathcal{P}_s + \sigma_{r_i}^2}} \right|^2 \right]}{\mathbb{E}\left[\sum_{i=1}^{R} \left| \frac{\sqrt{\mathcal{P}_{r_i}} \boldsymbol{H}_{r_i,d}(k,k)}{\sqrt{|\boldsymbol{H}_{s,r_i}(k,k)|^2 \mathcal{P}_s + \sigma_{r_i}^2}} \right|^2 \sigma_{r_i}^2 + \sigma_d^2 \right]} + \frac{\mathcal{P}_s \mathbb{E}|\boldsymbol{H}_{s,d}(k,k)|^2}{\sigma_d^2}. \tag{4.10}$$

We assume statistical CSI is available at the transmitter side, i.e., $\mathbb{E}[|\boldsymbol{H}_{s,r_i}(k,k)|^2] = \eta^k_{s,r_i}$, $\mathbb{E}[|\boldsymbol{H}_{r_i,d}(k,k)|^2] = \eta^k_{r_i,d}$, and $\mathbb{E}[\boldsymbol{H}_{s,d}(k,k)] = \eta^k_{s,d}$. As each subcarrier has the same channel power on average for Rayleigh fading channels, i.e., $\eta^k_{s,r_i} = \eta_{s,r_i}$, $\eta^k_{r_i,d} = \eta_{r_i,d}$, and $\eta^k_{s,d} = \eta_{s,d}$, the same power allocation result is obtained for each subcarrier. Thus, index k can be removed for presentation brevity. With $\overline{\gamma}_k$, $\boldsymbol{H}_{s,r_i}(k,k)$, $\boldsymbol{H}_{r_i,d}(k,k)$, and $\boldsymbol{H}_{s,d}(k,k)$ replaced by $\overline{\gamma}$, h_{s,r_i}, $h_{r_i,d}$, and $h_{s,d}$, respectively, we obtain

$$\overline{\gamma} = \frac{\mathbb{E}\left[\mathcal{P}_s\left|\sum_{i=1}^{R}\frac{\sqrt{\mathcal{P}_{r_i}}h_{s,r_i}h_{r_i,d}}{\sqrt{|h_{s,r_i}|^2\mathcal{P}_s+\sigma^2_{r_i}}}\right|^2\right]}{\mathbb{E}\left[\sum_{i=1}^{R}\left|\frac{\sqrt{\mathcal{P}_{r_i}}h_{r_i,d}}{\sqrt{|h_{s,r_i}|^2\mathcal{P}_s+\sigma^2_{r_i}}}\right|^2\sigma^2_{r_i}+\sigma^2_d\right]} + \frac{\mathcal{P}_s\mathbb{E}|h_{s,d}|^2}{\sigma^2_d} \tag{4.11}$$

$$= \frac{\mathcal{P}_s\sum_{i=1}^{R}\mathcal{P}_{r_i}\eta_{r_i,d}\mathbb{E}\left[\frac{|h_{s,r_i}|^2}{\mathcal{P}_s|h_{s,r_i}|^2+\sigma^2_{r_i}}\right]}{\sum_{i=1}^{R}\mathcal{P}_{r_i}\eta_{r_i,d}\mathbb{E}\left[\frac{1}{\mathcal{P}_s|h_{s,r_i}|^2+\sigma^2_{r_i}}\right]\sigma^2_{r_i}+\sigma^2_d} + \frac{\mathcal{P}_s\eta_{s,d}}{\sigma^2_d}. \tag{4.12}$$

The optimal $\mathcal{P}_s$ and $\mathcal{P}_{r_i}$ are difficult to obtain by optimizing $\overline{\gamma}$ directly. However, the closed-form suboptimal solution can be found by optimizing the upper bound of $\overline{\gamma}$. Based on Jensen's inequality, $\mathbb{E}\left[\frac{|h_{s,r_i}|^2}{\mathcal{P}_s|h_{s,r_i}|^2+\sigma^2_{r_i}}\right] < \frac{\mathbb{E}|h_{s,r_i}|^2}{\mathcal{P}_s\mathbb{E}|h_{s,r_i}|^2+\sigma^2_{r_i}} = \frac{\eta_{s,r_i}}{\mathcal{P}_s\eta_{s,r_i}+\sigma^2_{r_i}}$ and $\mathbb{E}\left[\frac{1}{\mathcal{P}_s|h_{s,r_i}|^2+\sigma^2_{r_i}}\right] > \frac{1}{\mathcal{P}_s\mathbb{E}|h_{s,r_i}|^2+\sigma^2_{r_i}} = \frac{1}{\mathcal{P}_s\eta_{s,r_i}+\sigma^2_{r_i}}$. Thus, the upper bound of $\overline{\gamma}$ is given as

$$\overline{\gamma}_u = \frac{\mathcal{P}_s\sum_{i=1}^{R}\mathcal{P}_{r_i}\frac{\eta_{r_i,d}\eta_{s,r_i}}{\mathcal{P}_s\eta_{s,r_i}+\sigma^2_{r_i}}}{\sum_{i=1}^{R}\frac{\mathcal{P}_{r_i}\eta_{r_i,d}}{\mathcal{P}_s\eta_{s,r_i}+\sigma^2_{r_i}}\sigma^2_{r_i}+\sigma^2_d} + \frac{\mathcal{P}_s\eta_{s,d}}{\sigma^2_d}. \tag{4.13}$$

The power optimization problem turns out to be:

Problem 4.1.

$$[\mathcal{P}_s,\mathcal{P}_{r_1},\cdots,\mathcal{P}_{r_R}] = \arg\max_{\mathcal{P}_s,\mathcal{P}_{r_1},\cdots,\mathcal{P}_{r_R}}\overline{\gamma}_u, \tag{4.14}$$

$$\text{s.t.}\quad \mathcal{P}_s+\sum_{i=1}^{R}\mathcal{P}_{r_i} = \mathcal{P}_{\text{tot}}, \tag{4.15}$$

$$\mathcal{P}_s,\mathcal{P}_{r_1},\cdots,\mathcal{P}_{r_R} > 0. \tag{4.16}$$

Solving the above power optimization problem gives rise to the following theorem:

Theorem 4.1. *The optimal power allocation of the AsAP protocol according to Problem 4.1 is to allocate power $\mathcal{P}_s^*(i^*)$ to the source node and power $\mathcal{P}_r^*(i^*)$ to the relay node i^*, where*

$$\mathcal{P}_s^*(i^*) = \min\left\{\frac{\frac{\mathcal{P}_{tot}\eta_{s,r_{i^*}}\eta_{r_{i^*},d}}{\sigma_{r_{i^*}}^2\sigma_d^2} + \frac{\mathcal{P}_{tot}\eta_{s,d}\eta_{r_{i^*},d}}{\sigma_d^2\sigma_{r_{i^*}}^2} + \frac{\eta_{s,d}}{\sigma_d^2}}{g(i^*) + \sqrt{\frac{1+\mathcal{P}_{tot}\eta_{s,r_{i^*}}/\sigma_{r_{i^*}}^2}{1+\mathcal{P}_{tot}\eta_{r_{i^*},d}/\sigma_d^2}\frac{\eta_{s,r_{i^*}}\eta_{r_{i^*},d}}{\sigma_{r_{i^*}}^2\sigma_d^2}g(i^*)}}, \mathcal{P}_{tot}\right\} \tag{4.17}$$

and

$$\mathcal{P}_r^*(i^*) = \max\left\{\frac{\frac{\mathcal{P}_{tot}\eta_{s,r_{i^*}}\eta_{r_{i^*},d}}{\sigma_{r_{i^*}}^2\sigma_d^2} - \frac{\mathcal{P}_{tot}\eta_{s,d}\eta_{s,r_{i^*}}}{\sigma_d^2\sigma_{r_{i^*}}^2} - \frac{\eta_{s,d}}{\sigma_d^2}}{g(i^*) + \sqrt{\frac{1+\mathcal{P}_{tot}\eta_{r_{i^*},d}/\sigma_d^2}{1+\mathcal{P}_{tot}\eta_{s,r_{i^*}}/\sigma_{r_{i^*}}^2}\frac{\eta_{s,r_{i^*}}\eta_{r_{i^*},d}}{\sigma_{r_{i^*}}^2\sigma_d^2}g(i^*)}}, 0\right\}, \tag{4.18}$$

where $g(i^*) = \max\left\{\frac{\eta_{s,r_{i^*}}\eta_{r_{i^*},d}}{\sigma_{r_{i^*}}^2\sigma_d^2} + \frac{\eta_{s,d}\eta_{r_{i^*},d}}{\sigma_d^2\sigma_d^2} - \frac{\eta_{s,r_{i^*}}\eta_{s,d}}{\sigma_{r_{i^*}}^2\sigma_d^2}, 0\right\}$.

The relay index i^* is

$$i^* = \arg\max_{i\in\{1,\cdots,R\}} \frac{\overline{\gamma}_{s,r_i}^*\overline{\gamma}_{r_i,d}^*}{\overline{\gamma}_{s,r_i}^* + \overline{\gamma}_{r_i,d}^* + 1} + \overline{\gamma}_{s,d}^*, \tag{4.19}$$

where $\overline{\gamma}_{s,r_i}^* = \mathcal{P}_s^*(i)\eta_{s,r_i}/\sigma_{r_i}^2$, $\overline{\gamma}_{r_i,d}^* = \mathcal{P}_r^*(i)\eta_{r_i,d}/\sigma_d^2$, *and* $\overline{\gamma}_{s,d}^* = \mathcal{P}_s^*(i)\eta_{s,d}/\sigma_d^2$.

Proof. $\overline{\gamma}_u$ in (4.13) is optimized in two steps:

1. Optimization of the power allocation among relays $\mathcal{P}_{r_i}, i \in \{1,\cdots,R\}$ with fixed $\mathcal{P}_s$, namely, maximizing the first part of $\overline{\gamma}_u$ under the power constraint $\sum_{i=1}^R \mathcal{P}_{r_i} = \mathcal{P}_{\text{tot}} - \mathcal{P}_s = \mathcal{P}_r$
2. Optimization of the power allocation between the source and relay(s), $\mathcal{P}_s$ and $\mathcal{P}_r$, subject to $\mathcal{P}_s + \mathcal{P}_r = \mathcal{P}_{\text{tot}}$

In the first step, we begin by reexpressing the first part of $\overline{\gamma}_u$ in matrix format:

$$\frac{\mathcal{P}_s\sum_{i=1}^R \mathcal{P}_{r_i}\frac{\eta_{r_i,d}\eta_{s,r_i}}{\mathcal{P}_s\eta_{s,r_i}+\sigma_{r_i}^2}}{\sum_{i=1}^R \frac{\mathcal{P}_{r_i}\eta_{r_i,d}}{\mathcal{P}_s\eta_{s,r_i}+\sigma_{r_i}^2}\sigma_{r_i}^2 + \sigma_d^2} = \frac{\tilde{\boldsymbol{\alpha}}^T\boldsymbol{\Lambda}\tilde{\boldsymbol{\alpha}}}{\tilde{\boldsymbol{\alpha}}^T(\boldsymbol{\Xi} + \frac{\sigma_d^2}{\mathcal{P}_r}\boldsymbol{I}_R)\tilde{\boldsymbol{\alpha}}}, \tag{4.20}$$

where $\boldsymbol{\Lambda} = \text{diag}[\frac{\mathcal{P}_s\eta_{r_1,d}\eta_{s,r_1}}{\mathcal{P}_s\eta_{s,r_1}+\sigma_{r_1}^2}, \frac{\mathcal{P}_s\eta_{r_2,d}\eta_{s,r_2}}{\mathcal{P}_s\eta_{s,r_2}+\sigma_{r_2}^2}, \cdots, \frac{\mathcal{P}_s\eta_{r_R,d}\eta_{s,r_R}}{\mathcal{P}_s\eta_{s,r_R}+\sigma_{r_R}^2}]$, $\tilde{\boldsymbol{\alpha}} = \boldsymbol{\alpha}/\|\boldsymbol{\alpha}\|$, $\boldsymbol{\alpha} = [\sqrt{\mathcal{P}_{r_1}}, \sqrt{\mathcal{P}_{r_2}}, \cdots, \sqrt{\mathcal{P}_{r_R}}]^T$, and $\boldsymbol{\Xi} = \text{diag}[\frac{\eta_{r_1,d}\sigma_{r_1}^2}{\mathcal{P}_s\eta_{s,r_1}+\sigma_{r_1}^2}, \frac{\eta_{r_2,d}\sigma_{r_2}^2}{\mathcal{P}_s\eta_{s,r_2}+\sigma_{r_2}^2}, \cdots, \frac{\eta_{r_R,d}\sigma_{r_R}^2}{\mathcal{P}_s\eta_{s,r_R}+\sigma_{r_R}^2}]$.

Furthermore, by defining

$$\boldsymbol{u} = \left(\boldsymbol{\Xi} + \frac{\sigma_d^2}{\mathcal{P}_r}\boldsymbol{I}_R\right)^{1/2}\tilde{\boldsymbol{\alpha}}, \tag{4.21}$$

the optimization problem can be represented as

$$\begin{aligned}&\max_{\tilde{\boldsymbol{\alpha}}:\|\tilde{\boldsymbol{\alpha}}\|^2\le 1} \frac{\tilde{\boldsymbol{\alpha}}^T\boldsymbol{\Lambda}\tilde{\boldsymbol{\alpha}}}{\tilde{\boldsymbol{\alpha}}^T(\boldsymbol{\Xi} + \frac{\sigma_d^2}{\mathcal{P}_r}\boldsymbol{I}_R)\tilde{\boldsymbol{\alpha}}}\\ &= \max_{\boldsymbol{u}:\|\boldsymbol{u}\|^2\le 1} \frac{\boldsymbol{u}^T\boldsymbol{D}\boldsymbol{u}}{\|\boldsymbol{u}\|^2}.\end{aligned} \tag{4.22}$$

where $\boldsymbol{D}$ is a diagonal matrix:

$$\begin{aligned}\boldsymbol{D} &= \left(\boldsymbol{\Xi} + \frac{\sigma_d^2}{\mathcal{P}_r}\boldsymbol{I}_R\right)^{-1/2}\boldsymbol{\Lambda}\left(\boldsymbol{\Xi} + \frac{\sigma_d^2}{\mathcal{P}_r}\boldsymbol{I}_R\right)^{-1/2}\\ &= \mathrm{diag}\Big(\frac{\overline{\gamma}_{s,r_1}\overline{\gamma}_{r_1,d}}{\overline{\gamma}_{s,r_1}+\overline{\gamma}_{r_1,d}+1}, \cdots, \frac{\overline{\gamma}_{s,r_R}\overline{\gamma}_{r_R,d}}{\overline{\gamma}_{s,r_R}+\overline{\gamma}_{r_R,d}+1}\Big),\end{aligned} \tag{4.23}$$

$\overline{\gamma}_{s,r_i} = \frac{\mathcal{P}_s\eta_{s,r_i}}{\sigma_{r_i}^2}$, and $\overline{\gamma}_{r_i,d} = \frac{\mathcal{P}_r\eta_{r_i,d}}{\sigma_d^2}$. The maximum of $\boldsymbol{u}^T\boldsymbol{D}\boldsymbol{u}/\|\boldsymbol{u}\|^2$ corresponds to the maximum diagonal element of $\boldsymbol{D}$. Suppose that

$$i^* = \arg\max_i \frac{\overline{\gamma}_{s,r_i}\overline{\gamma}_{r_i,d}}{\overline{\gamma}_{s,r_i}+\overline{\gamma}_{r_i,d}+1} \tag{4.24}$$

is the position that has the maximum diagonal element. Then $\boldsymbol{u}/\|\boldsymbol{u}\|$ is a vector with 1 in the i^*th entry and 0 elsewhere. Thus,

$$\boldsymbol{\alpha} = \sqrt{\mathcal{P}_r}\frac{\boldsymbol{u}}{\|\boldsymbol{u}\|}. \tag{4.25}$$

This result indicates that with statistical CSI, the optimal cooperative strategy is to allocate all relay transmit power $\mathcal{P}_r$ to relay i^* which maximizes $\frac{\overline{\gamma}_{s,r_i}\overline{\gamma}_{r_i,d}}{\overline{\gamma}_{s,r_i}+\overline{\gamma}_{r_i,d}+1}, i \in \{1, \cdots, R\}$.

In the second step, after choosing the relay i^*, the resulting $\overline{\gamma}_u$ in (4.13) is given as

$$\overline{\gamma}_{i^*}(\mathcal{P}_s, \mathcal{P}_r) = \frac{\overline{\gamma}_{s,r_{i^*}}\overline{\gamma}_{r_{i^*},d}}{\overline{\gamma}_{s,r_{i^*}}+\overline{\gamma}_{r_{i^*},d}+1} + \overline{\gamma}_{s,d}. \tag{4.26}$$

Then the optimization problem can be formulated as follows:

$$\max_{\mathcal{P}_s,\mathcal{P}_r} \overline{\gamma}_{i^*}(\mathcal{P}_s,\mathcal{P}_r)$$
$$\text{subject to } \mathcal{P}_s + \mathcal{P}_r = \mathcal{P}_{\text{tot}}.$$

Referring to the solution of a similar problem in [3], the optimal power allocation result is given in (4.17) and (4.18).

When relay i^* is selected, the maximum value of $\overline{\gamma}_{i^*}$ can be computed by substituting $\mathcal{P}_s^*$ and $\mathcal{P}_r^*$ into (4.26)

$$\gamma_{i^*}^{opt} = \overline{\gamma}_{i^*}(\mathcal{P}_s^*, \mathcal{P}_r^*). \tag{4.27}$$

There still remains one issue, i.e., relay selection in the first step depends on the values of $\mathcal{P}_s$ and $\mathcal{P}_r$, while the optimal power allocation between $\mathcal{P}_s$ and $\mathcal{P}_r$ also depends on the selected relay. Observe that the optimization result of the first step suggests single relay transmission for any power combination between $\mathcal{P}_s$ and $\mathcal{P}_r$. Thus, we can perform the optimal power allocation for each relay using (4.17) and (4.18), and the relay which maximizes the value of (4.27) is selected. This gives rise to Theorem 4.1. □

Theorem 4.1 demonstrates that only the relay which maximizes (4.19) transmits, while all other relays keep silent. The relay selection criteria is given as $\frac{\overline{\gamma}_{s,r_i}^* \overline{\gamma}_{r_i,d}^*}{\overline{\gamma}_{s,r_i}^* + \overline{\gamma}_{r_i,d}^* + 1} + \overline{\gamma}_{s,d}^*$, which is called the effective SNR at relay i. It's notable that if $\frac{\eta_{s,r_i}\eta_{r_i,d}}{\sigma_{r_i}^2\sigma_d^2} + \frac{\eta_{s,d}\eta_{r_i,d}}{\sigma_d^2\sigma_d^2} - \frac{\eta_{s,r_i}\eta_{s,d}}{\sigma_{r_i}^2\sigma_d^2} < 0$ or $\frac{\mathcal{P}_{\text{tot}}\eta_{s,r_i}\eta_{r_i,d}}{\sigma_{r_i}^2\sigma_d^2} - \frac{\mathcal{P}_{\text{tot}}\eta_{s,d}\eta_{s,r_i}}{\sigma_d^2\sigma_{r_i}^2} - \frac{\eta_{s,d}}{\sigma_d^2} < 0$, all transmit power is allocated to the source.

In summary, we optimized the power allocation between the source and the relays based on the upper bound of the approximate average SNR. The power allocation results suggest choosing the relay which has the maximum effective SNR to transmit while other relays keeping silent.

4.3 SR-AsAP Protocol

Based on the power optimization results in Sect. 4.2, we propose the following SR-AsAP protocol to enhance system performance of the AsAP protocol. As the asynchronous design is very critical for the protocol feasibility, it is also investigated.

4.3.1 Protocol Description

The SR-AsAP protocol consists of three phases: statistical CSI retrieval, relay selection, and AsAP transmission.

1. Statistical CSI retrieval: assuming the localization service is available. The source first chooses the potential relays $r_i, i \in \{1, \cdots, R\}$, which are located between the source and the destination. Then the source broadcasts the pilot signal together with relay indices. The potential relays and the destination estimate their statistical CSI with respect to the source, i.e., η_{s,r_i} at relay i and $\eta_{s,d}$ at the destination. Then each relay transmits its pilot signal in turn to the destination together with its index. The destination estimates its statistical CSI with respect to each relay, i.e., $\eta_{r_i,d}$ for relay $i, i \in \{1, \ldots, R\}$. Finally, each relay forwards its S-R statistical CSI, i.e., η_{s,r_i}, to the destination. Statistical CSI η can be estimated by averaging the channel power in the TD, as detailed in Sect. 2.2.
2. Relay selection: relay selection and the transmit power allocation are performed by the destination as follows. For a given total transmit power $\mathcal{P}_{\text{tot}}$, the destination computes $\mathcal{P}_s^*$ and $\mathcal{P}_r^*$ with (4.17) and (4.18) for each relay. Following (4.19), the relay with the maximum effective SNR is selected. Then the destination broadcasts the index of the selected relay as well as power allocation information, i.e., $\mathcal{P}_s^*$ and $\mathcal{P}_r^*$, to the source and the relays. Then the selected relay is activated to forward the source signal while other relays keep silent.
3. AsAP transmission: the source generates information symbols modulated by GLCP OFDM with transmit power $\mathcal{P}_s = \mathcal{P}_s^*$ and broadcasts them to the relay and the destination. After receiving the OFDM symbols from the source, the selected relay amplifies the received signal with transmit power $P_r = \mathcal{P}_r^*$. Finally, the destination combines the DL and RL signals using MRC and performs decoding.

It is worth noticing that for the SR-AsAP protocol, it is assumed that node positions are fixed such that the average channel power, i.e., η_{s,r_i}, $\eta_{r_i,d}$, and $\eta_{s,d}$, is unchanged. If the channel power changes substantially, steps 1 and 2 need to be performed again to select the best relay.

4.3.2 Asynchronous Transmission Design

For the terrestrial cooperative AF protocols, the transmissions of the source and the relays are coordinated to avoid interference. However, for medium-long-range UAC, the long and variable signal propagation delay results in difficult time synchronization among the source and the relays. Therefore, it is preferable to adopt asynchronous transmission at the source and the relays. The traditional method to implement the asynchronous transmission is to let the relay simply process the signal from the source and retransmit the signal to the destination immediately [4, 5]. However, as shown in Fig. 4.2, since the AF operation can only be performed after a complete OFDM symbol is received, the delay of the RL signal would be at least one OFDM symbol duration longer than the DL signal at the destination. Therefore, the DL signal could cause severe interference toward the RL signal. To resolve interference between the DL signal and the RL signal, one way is to let the CP length longer than $(N + 2L)t_s$ where t_s is the sampling period and implement the Viterbi

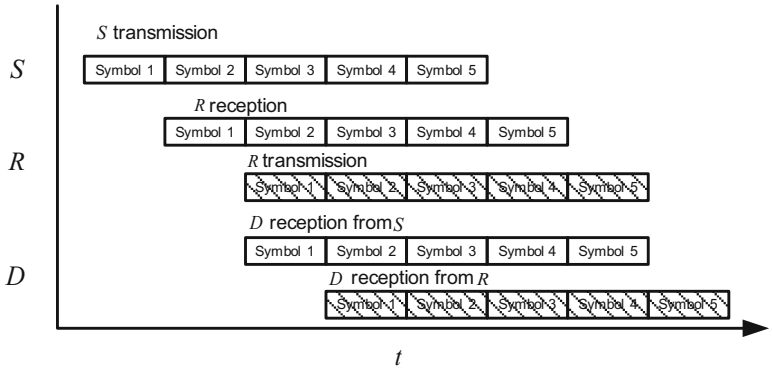

Fig. 4.2 Traditional asynchronous transmission scheme. The signal propagation time from the source to the relay and from the relay to the destination is set to be one OFDM symbol length

decoder to decode the received signal [6]. However, this adds more computational burden toward the receiver. In addition, due to the long CP length, the effective transmission time of the data signal is no more than half of total transmission time.

Thus, to remove interference between the DL and RL signals and avoid increasing computational burden at the destination, we propose a novel asynchronous transmission scheme for our SR-AsAP protocol, as illustrated in Fig. 4.3. First, the source transmits one packet to the selected relay and the destination, which consists of one preamble, N_s OFDM symbols, and one postamble, as shown in Fig. 4.4. Then the relay and the destination correlate the preamble and the postamble with the received signal to retrieve the starting and ending points of the packet, respectively. Figure 4.5 shows one snapshot of the correlation result of the preamble in the Taiwan 2013 sea experiment. Once the relay receives a full packet, it amplifies and forwards each OFDM symbol in the packet to the destination immediately. The preamble and the postamble are attached at the head and the tail of the amplified OFDM symbols, respectively. Finally, the destination correlates the preamble and the postamble with the received signal to get the starting and ending points of the received packets from the relay, respectively. During the decoding phase, the destination combines the received OFDM symbols from the source and the relay. At the same time, the source overhears the signal from the relay. When the relay stops transmission, the source transmits the next packet.

Our proposed asynchronous transmission scheme has three merits. First, the half-duplex mode is adopted at the relay and no self-interference cancellation mechanisms are needed. This simplifies the relay operation. Secondly, the relay starts transmission only when the whole data packet is received. This naturally separates the DL and RL signals at the destination. Therefore, interference is removed, and the destination could combine the DL and RL signals using MRC. Thirdly, the relay and the destination can locate the starting and ending points of the packet by itself without resorting to the common timing reference. Therefore, the transmission is asynchronous.

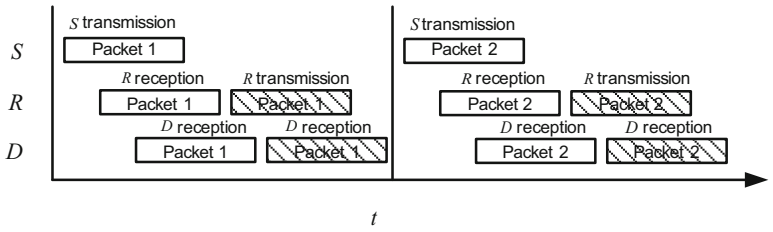

Fig. 4.3 Asynchronous transmission of the SR-AsAP protocol

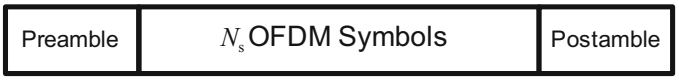

Fig. 4.4 Packet structure

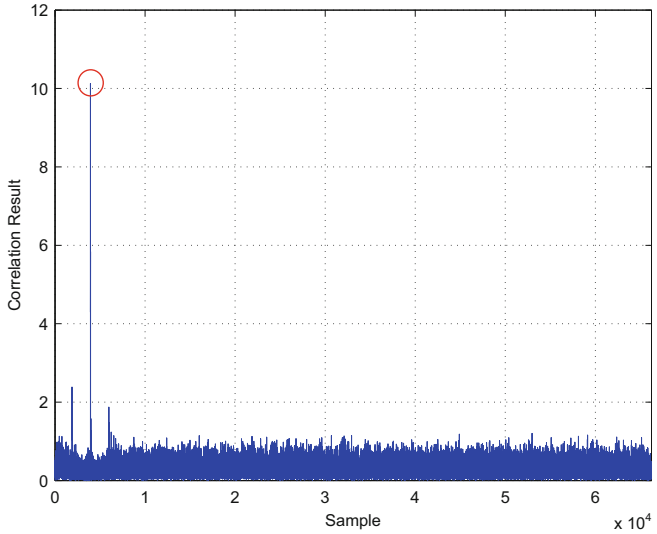

Fig. 4.5 Correlation result of the preamble in the Taiwan 2013 sea experiment. The preamble is correlated with the received signal, and the timing instant with the strongest peak is selected as the starting point of the preamble

4.3.3 Efficiency Analysis

Next, we analyze the transmission efficiency of the SR-AsAP protocol. Assume that the length of the preamble, the postamble, the OFDM symbol (including CP), and the relay processing time equals t_{sym}. For each successful packet transmission, the total transmission time consists of the source transmission time $(N_s + 2)t_{\text{sym}}$, the signal propagation time from the source to the relay $t_{s,r}$, the relay processing time t_{sym}, the relay transmission time $(N_s + 2)t_{\text{sym}}$, and the signal propagation time from

the relay to the destination $t_{r,d}$. The total transmission time t_{total} is given as

$$t_{\text{total}} = t_{s,r} + t_{r,d} + (2N_s + 5)t_{\text{sym}}. \tag{4.28}$$

Thus, the transmission efficiency is defined as

$$\begin{aligned}\eta(N) &= \frac{t_{\text{eff}}}{t_{\text{total}}} \\ &= \frac{N_s t_{\text{sym}}}{t_{s,r} + t_{r,d} + (2N_s + 5)t_{\text{sym}}} \\ &= \frac{N_s}{\alpha + (2N_s + 5)}\end{aligned} \tag{4.29}$$

where $t_{\text{eff}} = N_s t_{\text{sym}}$ is the effective data signal time and $\alpha = (t_{s,r} + t_{r,d})/t_{\text{sym}}$. Notice that for large N_s, the transmission efficiency approaches $1/2$, i.e.,

$$\lim_{N_s \to \infty} \eta(N_s) = \lim_{N_s \to \infty} \frac{N_s}{\alpha + (2N_s + 5)} = \frac{1}{2}. \tag{4.30}$$

The effect of α and N_s is shown in Fig. 4.6. From the figure, it can be observed that the transmission efficiency increases with N_s and decreases with α. This means the transmission efficiency could be improved by increasing the OFDM symbol number in one packet. In addition, to reduce α, we can increase the OFDM

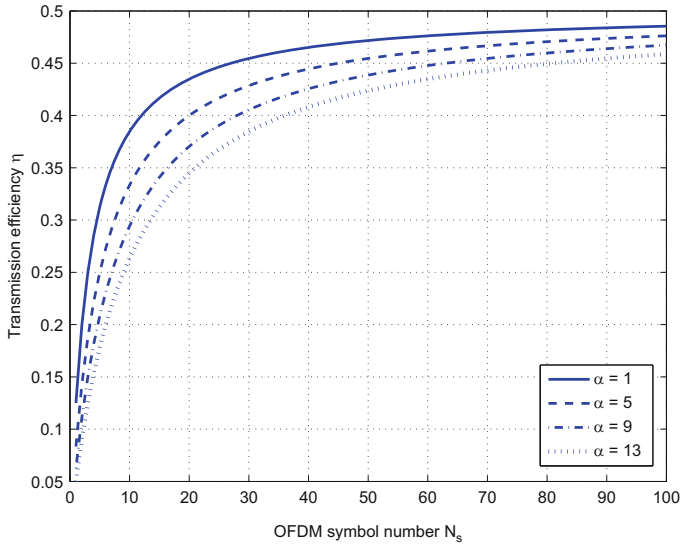

Fig. 4.6 Transmission efficiency with different OFDM symbol number N_s and α

symbol duration t_{sym}. However, for the long OFDM symbol duration, the subcarrier orthogonality is vulnerable to the Doppler effect. This suggests increasing the OFDM symbol number N_s is more effective than reducing α.

4.4 Performance Evaluations

In this section, to demonstrate performance of the proposed SR-AsAP protocol, we obtain the bit error rate (BER) through simulation. By comparing with other protocols, the benefits of our selective relaying design are verified.

The AsAP system has the S-D distance $D = 2000$ m. The water depth is 30 m. All nodes are placed on the sea bottom. Thus, each node can be identified by a two-dimensional coordinate. Figure 4.7 illustrates the selection of potential relays under this setup. The coordinates of the source and the destination are $(0, 0)$ and $(2000, 0)$ respectively. Only the green nodes within the circle are chosen as potential relays, while other nodes outside of the circle are not utilized. The circle is centered at $(1000, 0)$ with radius $D/4 = 500$. Binary phase shift keying (BPSK) signaling is used. The OFDM precoding size is chosen to be $K = 8$, and the OFDM symbol size is $N = 1024$. The carrier frequency is set as $f_c = 17$ kHz with bandwidth $B = 10$ kHz. The noise variances at all receivers are the same, i.e., $\sigma_d^2 = \sigma_{r_1}^2 = \cdots = \sigma_{r_R}^2 = 1$.

In Figs. 4.8 and 4.9, we plot BER performance of the DL-UAC protocol, the AsAP protocol with the uniform power allocation, and the SR-AsAP protocol. Three relays were randomly placed within the circle in Fig. 4.7. For the AsAP protocol with the uniform power allocation, all relays amplify and forward the received signal to the destination, and power is uniformly allocated among the source and the relays.

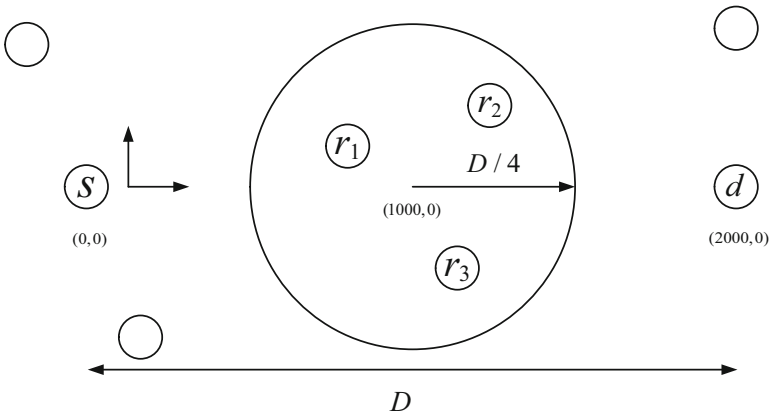

Fig. 4.7 Potential relay selection: the green nodes within the circle are chosen as potential relays, while other nodes outside of the circle are not utilized. The circle is centered at the midpoint between the source and the destination with radius $D/4$

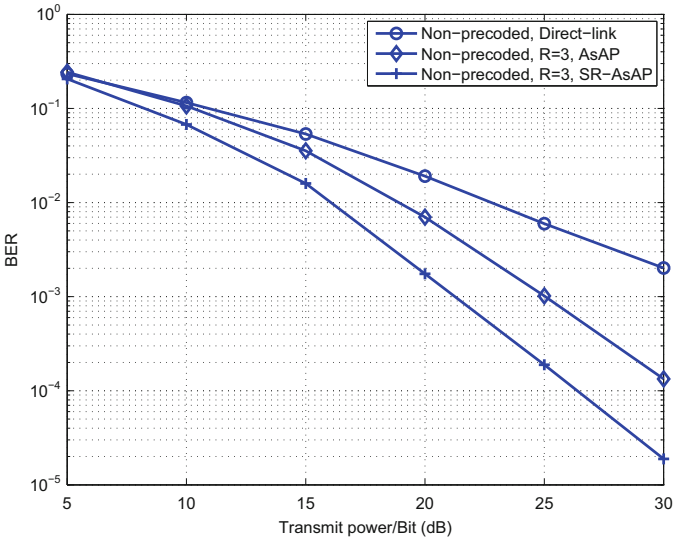

Fig. 4.8 Uncoded BER performance of the DL-UAC protocol, the AsAP protocol with the uniform power allocation, and the SR-AsAP protocol. The water depth is 30 m and the number of potential relays is $R = 3$

For the SR-AsAP protocol, the source selects the best relay. From the two figures, it can be observed that the SR-AsAP protocol outperforms the direct-link protocol and the AsAP protocol with the uniform power allocation for both the precoded and uncoded relay systems. For the SR-AsAP protocol, define the S-R power allocation ratio as $\alpha_p = \mathcal{P}_s/\mathcal{P}_{\text{tot}}$ and the optimal S-R power allocation ratio is $\alpha_p^* = \mathcal{P}_s^*/\mathcal{P}_{\text{tot}}$. In Fig. 4.10, we also compare BER performance of the SR-AsAP protocols with the optimal α_p^* and with $\alpha_p = 0.5$. It can be seen that the SR-AsAP protocol with optimal α_p^* slightly outperforms the SR-AsAP protocol with $\alpha_p = 0.5$.

4.5 Summary

In this chapter, we aimed at the energy-efficient and reliable cooperative protocol design for medium-long-range UAC. First, we adopted the instantaneous power allocation at the relays and MRC at the destination in the AsAP protocol and explored the power allocation among the source and the relays based on statistical CSI. The optimization results give rise to a relay selection scenario that only the relay which has the maximum effective SNR transmits, while all other relays keep silent. Thus, we proposed a SR-AsAP protocol. Second, to avoid interference between the DL and RL signals, the asynchronous transmission was designed for the SR-AsAP protocol. The theoretical analysis shows that the transmission efficiency of the SR-AsAP protocol increases with the OFDM symbol number in

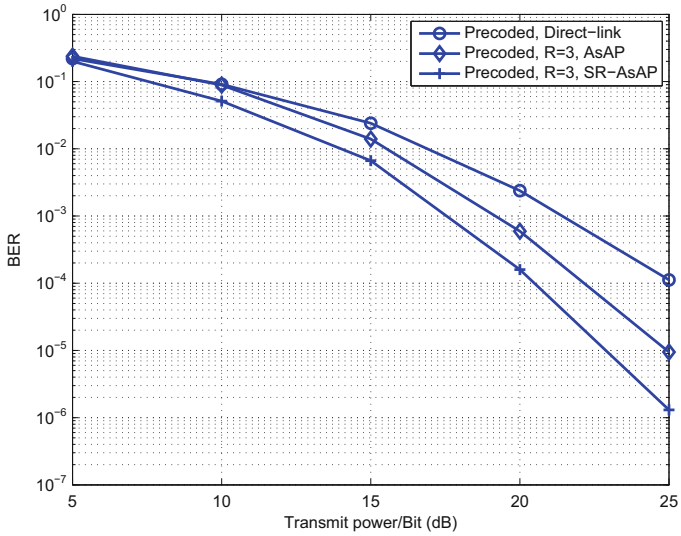

Fig. 4.9 Coded BER performance of the DL-UAC protocol, the AsAP protocol with the uniform power allocation, and the SR-AsAP protocol. The water depth is 30 m and the number of potential relays is $R = 3$

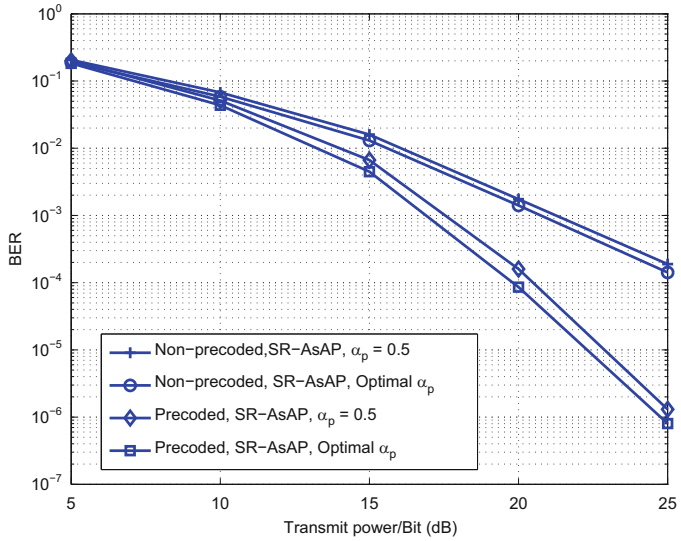

Fig. 4.10 BER performance comparison of SR-AsAP systems with the optimal power allocation α_p^* and with the power allocation ratio $\alpha_p = 0.5$

one data packet as well as the OFDM symbol duration. For large OFDM symbol number in one data packet, the transmission efficiency of the SR-AsAP protocol can approach $1/2$. Finally, performance of our SR-AsAP protocol was simulated. The results reveal that our SR-AsAP protocol outperforms the DL system and the AsAP protocol with all relay transmissions.

References

1. Z. Liu, Y. Xin, G.B. Giannakis, Linear constellation precoding for OFDM with maximum multipath diversity and coding gains. IEEE Trans. Commun. **51**(3), 416–427 (2003)
2. Z. Yi, I.-M. Kim, Joint optimization of relay-precoders and decoders with partial channel side information in cooperative networks. IEEE J. Select. Areas Commun. **25**(2), 447–458 (2007)
3. Z. Jingmei, Z. Qi, S. Chunju, W. Ying, Z. Ping, Z. Zhang, Adaptive optimal transmit power allocation for two-hop non-regenerative wireless relaying system, in *Proceedings of Vehicular Technology Conference*, vol. 2, 17–19 May 2004, pp. 1213–1217
4. R. Cao, F. Qu, L. Yang, On the capacity and system design of relay-aided underwater acoustic communications, in *Proceedings of Wireless Communications and Networking Conference*, Sydney, 18–21 April 2010, pp. 1–6
5. P. Wang, L. Zhang, V.O. Li, Asynchronous cooperative transmission for three-dimensional underwater acoustic networks. IET Commun. **7**(4), 286–294 (2013)
6. M. Rahmati, T.M. Duman, Achieving delay diversity in asynchronous underwater acoustic (UWA) cooperative communication systems. IEEE Trans. Wirel. Commun. **13**(3), 1367–1379 (2014)

Chapter 5
Energy-Efficient Hybrid Decomposed LT Codes for RA-UAC

In this chapter, we design a new type of hybrid DLT codes for dual-hop RA-UAC with improved energy efficiency and accuracy. First, the background of LT codes, DLT codes, and stochastic optimization methods is reviewed. Then, the nonnegative polynomial decomposition algorithm based on the stochastic multistart method is proposed. The motivation, the code construction, and the protocol design of the new hybrid DLT codes are presented at last.

5.1 Background

In this section, the background of LT codes, DLT codes, and stochastic optimization methods is introduced.

5.1.1 LT Codes

Fountain codes are rateless erasure codes with the property that unlimited coded data can be potentially generated from the source data, and from any subsets of the coded data with size equal to or slightly larger than the number of the source data, the source data can be recovered. LT codes [1] are the first practical realization of fountain codes. The corresponding encoding process of the source data containing K input packets consists of two steps:

1. First, the encoder randomly chooses integer $d \in [1, K]$ as the degree of the coded packet according to a DDP $\mu(x) = \sum_{i=1}^{K} \mu_i x^i$ with μ_i representing the probability of choosing degree $d = i$. According to the probability theory, DDP $\mu(x)$ has the following properties: $\mu(1) = 1$ and $\mu_i \geqslant 0,\ i \in \{1, \cdots, K\}$.

X. Cheng et al., *Cooperative OFDM Underwater Acoustic Communications*,
Wireless Networks, DOI 10.1007/978-3-319-33207-9_5

2. Second, d distinct input packets are randomly selected from the K source packets and then XORed together to generate one LT packet.

LT decoding adopts the belief propagation (BP) technique to recover source packets from LT packets. With the encoding degree and packet index information of each LT packet, a bipartite graph is formed. The decoder starts by releasing packets with degree one. Then, all edges connected to the degree one packet(s) are removed. This is done recursively until no degree-one packet is left. If all K input packets are recovered, the decoding is successful; otherwise, a failure is reported. To achieve high decoding success probability, a good encoding degree distribution has to be designed. In [1], Luby designed the RSD as follows:

Definition 5.1. With two parameters $\delta \in [0, 1]$ and $c \geqslant 0$, the RSD can be computed as

$$\mu(x) = \frac{\rho(x) + \tau(x)}{\beta}, \tag{5.1}$$

where $\beta = \rho(1) + \tau(1)$ is the normalizing constant, $\rho(x) = x/K + \sum_{i=2}^{K} x^i/i(i-1)$ is the DDP of the Ideal Soliton distribution (ISD), $\tau(x) = \sum_{i=1}^{K/R-1} Rx^i/iK + R\ln(R/\delta)x^{K/R}/K$, and $R = c\sqrt{K}\ln(K/\delta)$.

The RSD has much smaller BP decoding failure probability compared with the ISD and is used in practice. One important property of the RSD is that with $K + \mathcal{O}(\sqrt{K}\ln^2(K/\delta))$ RSD-encoded packets, the BP decoder can successfully recover all K source packets with the probability of at least $1 - \delta$.

5.1.2 DLT Codes

Different from LT codes, DLT codes generate a packet using two-layer random encoding. For each layer, the encoding process is in the same manner as LT codes, except with a different DDP. DLT encoding can be described as follows:

1. At the first-layer encoder which is implemented at the source, the packets are encoded with the DDP $\theta(x) = \sum_{i=1}^{D_\theta} \theta_i x^i$. The average encoding degree is $\theta'(1) = \sum_{i=1}^{D_\theta} i\theta_i$. The output packets are termed as DLT-1 packets.
2. Then, the DLT-1 packets are input to the second-layer encoder at the relay(s) with another DDP $\omega(x) = \sum_{i=1}^{D_\omega} \omega_i x^i$. The average encoding degree is $\omega'(1) = \sum_{i=1}^{D_\omega} i\omega_i$. The final output packets are called DLT-2 packets with the DDP $\hat{\mu}(x) = \omega(\theta(x))$ [2, 3].

The DLT decoder utilizes the same BP algorithm as the LT decoder. In order to achieve the decoding performance comparable to LT codes, the LT distribution $\mu(x)$ needs to be decomposed into two encoding DDPs $\theta(x)$ and $\omega(x)$ such that $\omega(\theta(x))$ resembles $\mu(x)$. In [3], the nonnegative-range method is proposed.

To guarantee the nonnegativity of the solution of $\omega_i, i \in \{1, \cdots, D_\omega\}$, the ranges of $\theta_i, i \in \{1, \cdots, D_\theta\}$ are obtained first. Then the values of $\theta_i, i \in \{1, \cdots, D_\theta\}$ and $\omega_i, i \in \{1, \cdots, D_\omega\}$ are determined through linear search within the valid ranges. However, there are several drawbacks for this nonnegative-range method. First, the decomposition results cannot guarantee to satisfy both constraints $\sum_{i=1}^{D_\theta} \theta_i = 1$ and $\sum_{i=1}^{D_\omega} \omega_i = 1$. Second, for nonsmooth DDPs, such as the RSD which has one spike at $d = K/R$, the algorithm may not provide a valid decomposition result. Finally, the nonnegative-range method only guarantees exact matches of lower-order terms of the target DDP. Therefore, the decomposed DDPs may have poor match at high-order terms. This leads to suboptimal decomposition and can potentially degrade the decoding performance. In [4], a similar decomposition algorithm is proposed for a modified DLT codes where the DLT decoder can receive both the DLT-1 packets and the DLT-2 packets. However, it also has the same problems as [3]. To address these issues, we propose a novel problem formulation of nonnegative polynomial decomposition which is a constrained nonlinear optimization problem.

5.1.3 Stochastic Optimization Methods

The stochastic optimization methods are very effective to solve nonlinear optimization problem as they can provide a probabilistic guarantee that the global minimum will be found for a sufficiently large sample size [5–7].

The simplest stochastic method is called pure random search, where a large amount of points are drawn from the constraint set, and the point with the smallest function value is chosen as the global minimum point. If the sample points are drawn uniformly over the constraint set and the objective function is continuous, the lowest function value of the sample points will converge to the global minimum with probability 1 as the sample size increases [8, 9]. The pure random search method is seldom used in practice as it is computational inefficient and the proper sample size is difficult to determine.

The multistart method is an extension of the pure random search method to improve the implementation efficiency. It consists of two phases, i.e., the global phase and the local phase. In the global phase, a number of points are randomly drawn from the constraint set following the uniform distribution. In the local phase, local search is performed to generate local minima from the selected samples. One important concept related to the multistart method is the region of attraction. Assume that the local phase always converges to a stationary point which may be the local minimum. Then, the region of attraction of a stationary point $\boldsymbol{x}^*$ is defined as the set of points in the constraint set starting from which the local search will converge to $\boldsymbol{x}^*$. In [10, 11], the Bayesian theory is applied to the multistart method to estimate the total number of stationary points and the relative size of the nonobserved regions of attraction. The main results of the Bayesian analysis are given as follows [10, 11]:

Proposition 5.1. *Suppose that the total number of the stationary points* $\overline{W} \in [1, \infty)$ *follows the uniform distribution, and given* $\overline{W} = W$*, the relative volumes of the regions of attraction for each stationary point also follows a uniform distribution on the unit simplex with dimension* $W - 1$*. If w different stationary points are found from the samples with size n using the multistart method, a Bayesian estimate of the total number of stationary points is*

$$\widehat{W} = \frac{w(n-1)}{n-w-2}, \tag{5.2}$$

and the Bayesian estimate of the portion of the constraint set uncovered by the regions of attraction of the stationary points already found is

$$\hat{r} = \frac{w(w+1)}{n(n-1)}. \tag{5.3}$$

The Bayesian analysis is very powerful as it can provide an optimal Bayesian stopping rule for the multistart algorithm. In the following, we formulate the nonnegative polynomial decomposition as a nonlinear optimization problem and utilize the stochastic multistart algorithm to solve it.

5.2 Nonnegative Polynomial Decomposition Algorithm

The key task of DLT code construction is to find a nonnegative decomposition of the target $\mu(x)$. The decomposed polynomials $\theta(x)$ and $\omega(x)$ need to have the property that their composition $\hat{\mu}(x) = \omega(\theta(x)) = \sum_{i=1}^{K} \hat{\mu}_i x^i$ is close to the target DDP $\mu(x)$. Therefore, we propose an optimal nonnegative polynomial decomposition that minimizes the fitting error $\mathcal{E} = \sum_{i=1}^{K} (\hat{\mu}_i - \mu_i)^2$. The problem statement is given as follows:

Problem 5.1. For a given distribution $\mu(x)$ with maximum order K, the nonnegative polynomial decomposition with orders of D_θ and D_ω can be obtained by solving the following optimization problem:

$$[\theta_1, \cdots, \theta_{D_\theta}, \omega_1, \cdots, \omega_{D_\omega}] = \arg \min_{\theta_1, \cdots, \theta_{D_\theta}, \omega_1, \cdots, \omega_{D_\omega}} \sum_{i=1}^{K} (\hat{\mu}_i - \mu_i)^2 \tag{5.4}$$

$$\begin{aligned} \text{s.t.} \sum_{i=1}^{D_\theta} \theta_i = 1, \ \sum_{i=1}^{D_\omega} \omega_i = 1, \\ \theta_1, \cdots, \theta_{D_\theta}, \omega_1, \cdots, \omega_{D_\omega} \geqslant 0. \end{aligned} \tag{5.5}$$

The new decomposition problem formulation treats all degree orders equally. As $\hat{\mu}_i$ is a nonlinear function of variables $\theta_1, \cdots, \theta_{D_\theta}, \omega_1, \cdots, \omega_{D_\omega}$, this problem belongs to the class of nonlinear least-squares optimization problems with nonnegative linear constraints. The objective function is not convex, and multiple local minima may exist. Thus, finding the global minimum is very difficult. To solve this problem, we utilize the projected gradient method as local search to generate the local minima [12, 13] and the stochastic multistart method to find the global minimum.

5.2.1 Projected Gradient Method

The local search using the projected gradient method mainly consists of four steps, namely, gradient computation, feasible direction calculation, parameters update, and stopping judgment, which are summarized in Algorithm 3.

5.2.1.1 Gradient Derivation

In Algorithm 3, $\nabla\mathcal{E}(\boldsymbol{x}^{(m)}) = \left[\frac{\partial\mathcal{E}}{\partial\theta_1^{(m)}}, \frac{\partial\mathcal{E}}{\partial\theta_2^{(m)}}, \cdots, \frac{\partial\mathcal{E}}{\partial\theta_{D_\theta}^{(m)}}, \frac{\partial\mathcal{E}}{\partial\omega_1^{(m)}}, \frac{\partial\mathcal{E}}{\partial\omega_2^{(m)}}, \cdots, \frac{\partial\mathcal{E}}{\partial\omega_{D_\omega}^{(m)}}\right]^T$ denotes the gradient of the fitting error $\mathcal{E}$. At a point, $\boldsymbol{x} = [\theta_1, \cdots, \theta_{D_\theta}, \omega_1, \cdots, \omega_{D_\omega}]^T$, the components of the gradient $\frac{\partial\mathcal{E}}{\partial\theta_k}, k \in \{1, 2, \cdots, D_\theta\}$ and $\frac{\partial\mathcal{E}}{\partial\omega_k}, k \in \{1, 2, \cdots, D_\omega\}$ can be computed as follows:

Algorithm 3: Projected gradient method

Input: The target DDP $\mu(x) = \sum_{i=1}^{K} \mu_i x^i$
Result: $\boldsymbol{x}^* = [\boldsymbol{\theta}^{*T}\boldsymbol{\omega}^{*T}]^T$, $\boldsymbol{\theta}^* = [\theta_1^*, \cdots, \theta_{D_\theta}^*]^T$, and $\boldsymbol{\omega}^* = [\omega_1^*, \cdots, \omega_{D_\omega}^*]^T$
Initialization: Set the initial values for $\boldsymbol{x}^{(1)} = [\boldsymbol{\theta}^{(1)T}\boldsymbol{\omega}^{(1)T}]^T$, where $\boldsymbol{\theta}^{(1)} = [\theta_1^{(1)}, \cdots, \theta_{D_\theta}^{(1)}]^T$ and $\boldsymbol{\omega}^{(1)} = [\omega_1^{(1)}, \cdots, \omega_{D_\omega}^{(1)}]^T$ such that $\sum_{i=1}^{D_\theta} \theta_i^{(1)} = 1$, $\sum_{i=1}^{D_\omega} \omega_i^{(1)} = 1$, and $\theta_1^{(1)}, \cdots, \theta_{D_\theta}^{(1)}, \omega_1^{(1)}, \cdots, \omega_{D_\omega}^{(1)} \geqslant 0$;
for $m = 1$ *to* M_{max} **do**
  Step 1: Compute the gradient $\nabla\mathcal{E}(\boldsymbol{x}^{(m)})$ according to (5.6) and (5.7);
  Step 2: Obtain the feasible direction $\boldsymbol{d}^{(m)} = [\boldsymbol{x}^{(m)} - s\nabla\mathcal{E}(\boldsymbol{x}^{(m)})]^+ - \boldsymbol{x}^{(m)}$, $s > 0$;
  Step 3: Update the parameters $\boldsymbol{x}^{(m+1)} = \boldsymbol{x}^{(m)} + \alpha^{(m)}\boldsymbol{d}^{(m)}$, where $\alpha^{(m)} = \underset{\alpha\in[0,\beta]}{\arg\min}\, \mathcal{E}(\boldsymbol{x}^{(m+1)} + \alpha\boldsymbol{d}^{(m)})$;
  Step 4: **if** $\|\boldsymbol{d}^{(m)}\| < \varepsilon$ **then** break
end
Output $\boldsymbol{x}^* = \boldsymbol{x}^{(m+1)}$

$$\frac{\partial \mathcal{E}}{\partial \theta_k} = 2 \sum_{i=1}^{K} \sum_{j=1}^{D_\omega} (\hat{\mu}_i - \mu_i) j \omega_j g_{j-1}(i-k), \tag{5.6}$$

and

$$\frac{\partial \mathcal{E}}{\partial \omega_k} = 2 \sum_{i=1}^{K} (\hat{\mu}_i - \mu_i) g_k(i), \tag{5.7}$$

where $g_1(n)$ and $g_j(n)$ are given in (5.10) and (5.11). The derivation of (5.6) and (5.7) is given as follows.

By expanding the polynomial coefficients, $\hat{\mu}(x) = \omega(\theta(x))$ can be written in a matrix form

$$\hat{\boldsymbol{\mu}} = \boldsymbol{\Theta} \boldsymbol{\omega}, \tag{5.8}$$

where $\hat{\boldsymbol{\mu}} = [\hat{\mu}_1, \hat{\mu}_2, \cdots, \hat{\mu}_K]^T$, $\boldsymbol{\omega} = [\omega_1, \omega_2, \cdots, \omega_{D_\omega}]^T$, and $\boldsymbol{\Theta}$ is a $K \times D_\omega$ matrix:

$$\boldsymbol{\Theta} = \begin{bmatrix} g_1(1) & g_2(1) & g_3(1) & \cdots & g_{D_\omega}(1) \\ g_1(2) & g_2(2) & g_3(2) & \cdots & g_{D_\omega}(2) \\ \vdots & \vdots & \vdots & \ddots & \vdots \\ g_1(K) & g_2(K) & g_3(K) & \cdots & g_{D_\omega}(K) \end{bmatrix}. \tag{5.9}$$

In (5.9),

$$g_1(n) = \begin{cases} \theta_n, n = 1, \cdots, D_\theta \\ 0, \text{elsewhere} \end{cases} \tag{5.10}$$

and

$$g_j(n) = g_1(n) \star g_{j-1}(n) = \sum_{k=-\infty}^{+\infty} g_1(k) g_{j-1}(n-k). \tag{5.11}$$

In other words, $g_j(n) = \underbrace{g_1(n) \star g_1(n) \star \cdots \star g_1(n)}_{j}$, where the asterisk $\star$ is the convolutional operator. In addition, to ensure $\hat{\mu}_n = 0$ for $n > K$, $D_\theta \times D_\omega$ has to be equal to or less than K.

The gradient of the fitting error $\mathcal{E}$ at a point $\boldsymbol{x} = [\theta_1, \cdots, \theta_{D_\theta}, \omega_1, \cdots, \omega_{D_\omega}]^T$ is denoted as $\nabla \mathcal{E}(\boldsymbol{x}) = \left[\frac{\partial \mathcal{E}}{\partial \theta_1}, \frac{\partial \mathcal{E}}{\partial \theta_2}, \cdots, \frac{\partial \mathcal{E}}{\partial \theta_{D_\theta}}, \frac{\partial \mathcal{E}}{\partial \omega_1}, \frac{\partial \mathcal{E}}{\partial \omega_2}, \cdots, \frac{\partial \mathcal{E}}{\partial \omega_{D_\omega}} \right]^T$. The gradient consists of two parts $\frac{\partial \mathcal{E}}{\partial \theta_k}, k \in \{1, 2, \cdots, D_\theta\}$ and $\frac{\partial \mathcal{E}}{\partial \omega_k}, k \in \{1, 2, \cdots, D_\omega\}$, which can be readily derived as follows:

$$\frac{\partial \mathcal{E}}{\partial \theta_k} = 2\sum_{i=1}^{K}(\hat{\mu}_i - \mu_i)\frac{\partial \hat{\mu}_i}{\partial \theta_k}, \tag{5.12}$$

and

$$\frac{\partial \mathcal{E}}{\partial \omega_k} = 2\sum_{i=1}^{K}(\hat{\mu}_i - \mu_i)\frac{\partial \hat{\mu}_i}{\partial \omega_k}. \tag{5.13}$$

As $\hat{\mu}_i$ is a linear function of ω_k, i.e., $\hat{\mu}_i = \sum_{j=1}^{D_\omega} g_j(i)\omega_j$, it can be computed as

$$\frac{\partial \hat{\mu}_i}{\partial \omega_k} = g_k(i). \tag{5.14}$$

To obtain $\frac{\partial \hat{\mu}_i}{\partial \theta_k}$, it is worth noting that

$$\begin{aligned}\frac{\partial g_j(i)}{\partial \theta_k} &= j\frac{\partial g_1(i)}{\partial \theta_k} \star g_{j-1}(i) \\ &= j\delta_{i,k} \star g_{j-1}(i) \\ &= j g_{j-1}(i-k),\end{aligned} \tag{5.15}$$

where $\delta_{i,k}$ is the Kronecker delta. Thus,

$$\begin{aligned}\frac{\partial \hat{\mu}_i}{\partial \theta_k} &= \sum_{j=1}^{D_\omega}\frac{\partial g_j(i)}{\partial \theta_k}\omega_j \\ &= \sum_{j=1}^{D_\omega} j\omega_j g_{j-1}(i-k).\end{aligned} \tag{5.16}$$

Finally, by substituting (5.16) and (5.14) into (5.12) and (5.13), the gradient of the fitting error (5.6) and (5.7) can be obtained.

5.2.1.2 Projection Calculation

Define the constraint set as $\boldsymbol{X} = \{\boldsymbol{x} : \sum_{i=1}^{D_\theta} x_i = 1, \sum_{i=1+D_\theta}^{D_\theta+D_\omega} x_i = 1, \text{ and } x_i \geqslant 0, i = 1, \cdots, D_\theta + D_\omega\}$. $[\boldsymbol{x}]^+ = \arg\min_{\boldsymbol{y}\in\boldsymbol{X}} \|\boldsymbol{y} - \boldsymbol{x}\|^2$ is a projection operator. Thus, $[\boldsymbol{x}^{(m)} - s\nabla\mathcal{E}(\boldsymbol{x}^{(m)})]^+$ represents the projection of $\boldsymbol{x}^{(m)} - s\nabla\mathcal{E}(\boldsymbol{x}^{(m)})$ into the constraint set $\boldsymbol{X}$. One important property of the projection operator $[\boldsymbol{x}]^+$ is

$$([\boldsymbol{x}]^+ - \boldsymbol{x})^T(\boldsymbol{y} - [\boldsymbol{x}]^+) \geqslant 0, \forall \boldsymbol{y} \in \boldsymbol{X} \text{ and } [\boldsymbol{x}]^+ \in \boldsymbol{X}, \tag{5.17}$$

which can be readily derived according to the property of convex optimization [13]. It is worth mentioning that the constraint set $\boldsymbol{X}$ is the Cartesian product of two standard simplexes, i.e., $\sum_{i=1}^{D_\theta} \theta_i = 1, \theta_1, \cdots, \theta_{D_\theta} \geqslant 0$, and $\sum_{i=1}^{D_\omega} \omega_i = 1, \omega_1, \cdots, \omega_{D_\omega} \geqslant 0$. Thus, the projection of $\boldsymbol{x}^{(m)} - s\nabla\mathcal{E}(\boldsymbol{x}^{(m)})$ into the constraint set $\boldsymbol{X}$ is equivalent to projecting its first D_θ elements into the simplex $\sum_{i=1}^{D_\theta} \theta_i = 1, \theta_1, \cdots, \theta_{D_\theta} \geqslant 0$, and its last D_ω elements into the simplex $\sum_{i=1}^{D_\omega} \omega_i = 1, \omega_1, \cdots, \omega_{D_\omega} \geqslant 0$, respectively. Solving the KKT condition [14, 15], the projection of a vector $\boldsymbol{y} = [y_1, \cdots, y_{D_\theta}]^T$ into the simplex $\sum_{i=1}^{D_\theta} \theta_i = 1, \theta_1, \cdots, \theta_{D_\theta} \geqslant 0$ is $\boldsymbol{t} = [t_1, \cdots, t_{D_\theta}]^T$, where $t_i = \max\{y_i + \lambda, 0\}$ and λ is chosen such that $\sum_{i=1}^{D_\theta} t_i = 1$. The projection of a vector into the simplex $\sum_{i=1}^{D_\omega} \omega_i = 1, \omega_1, \cdots, \omega_{D_\omega} \geqslant 0$ can be calculated similarly.

5.2.1.3 Convergence Analysis

The convergence of the projected gradient algorithm for Problem Statement 1 is provided in the following proposition:

Proposition 5.2. *For the nonnegative polynomial decomposition problem in Problem Statement* 1*, let* $\{\boldsymbol{x}^{(m)}\}$ *be the sequence generated by the projected gradient method with* $\alpha^{(m)}$ *chosen by the rule* $\alpha^{(m)} = \arg\min_{\alpha\in[0,\beta]} \mathcal{E}(\boldsymbol{x}^{(m)} + \alpha\boldsymbol{d}^{(m)})$*. Then,* $\{\boldsymbol{x}^{(m)}\}$ *converges to a stationary point* $\boldsymbol{x}^*$*, i.e.,* $\nabla\mathcal{E}(\boldsymbol{x}^*)^T(\boldsymbol{x} - \boldsymbol{x}^*) \geqslant 0, \forall \boldsymbol{x} \in \boldsymbol{X}$.

Proof. In the first step, we prove the sequence $\{\mathcal{E}(\boldsymbol{x}^{(m)})\}$ converges. It can be readily derived that

$$\begin{aligned}\nabla\mathcal{E}(\boldsymbol{x}^{(m)})^T\boldsymbol{d}^{(m)} &= \frac{-\|\boldsymbol{d}^{(m)}\|^2}{s} + \frac{[\boldsymbol{x}^{(m)} - s\nabla\mathcal{E}(\boldsymbol{x}^{(m)})]^{+T}\boldsymbol{d}^{(m)}}{s} \\ &\quad - \frac{(\boldsymbol{x}^{(m)} - s\nabla\mathcal{E}(\boldsymbol{x}^{(m)}))^T\boldsymbol{d}^{(m)}}{s} \\ &\leqslant \frac{-\|\boldsymbol{d}^{(m)}\|^2}{s}. \end{aligned} \tag{5.18}$$

which utilizes the property of projection (5.17), i.e.,

$$\left[[\boldsymbol{x}^{(m)} - s\nabla\mathcal{E}(\boldsymbol{x}^{(m)})]^+ - (\boldsymbol{x}^{(m)} - s\nabla\mathcal{E}(\boldsymbol{x}^{(m)}))\right]^T(-\boldsymbol{d}^{(m)}) \geq 0. \tag{5.19}$$

Equation (5.18) means direction $\boldsymbol{d}^{(m)}$ is descent. Define the $\psi_m(\alpha) = \mathcal{E}(\boldsymbol{x}^{(m)} + \alpha\boldsymbol{d}^{(m)})$. Then $\frac{\partial\psi_m(\alpha)}{\partial\alpha}|_{\alpha=0} = \nabla\mathcal{E}(\boldsymbol{x}^{(m)})^T\boldsymbol{d}^{(m)} \leqslant 0$. Thus, there exists $\overline{\alpha} \geqslant 0$ such that $\psi_m(0) \geqslant \psi_m(\alpha)$ for all $\alpha \in [0, \overline{\alpha}]$. As $\alpha^{(m)} = \arg\min_{\alpha\in[0,\beta]} \mathcal{E}(\boldsymbol{x}^{(m)} + \alpha\boldsymbol{d}^{(m)})$, we have $\mathcal{E}(\boldsymbol{x}^{(m+1)}) = \psi_m(\alpha^{(m)}) \leqslant \psi_m(\min(\beta, \overline{\alpha})) \leqslant \psi_m(0) = \mathcal{E}(\boldsymbol{x}^{(m)})$. Since $\{\mathcal{E}(\boldsymbol{x}^{(m)})\}$ is nonincreasing and lower bounded by 0, according to the monotone convergence theorem, the limit of $\{\mathcal{E}(\boldsymbol{x}^{(m)})\}$ exists.

In the second step, we prove that the point of convergence is stationary. Suppose $\boldsymbol{x}^*$ is the point of convergence, namely, $\lim_{m\to\infty} \mathcal{E}(\boldsymbol{x}^{(m)}) = \mathcal{E}(\boldsymbol{x}^*)$. Then $\lim_{m\to\infty} \mathcal{E}(\boldsymbol{x}^{(m+1)}) = \lim_{m\to\infty} \mathcal{E}(\boldsymbol{x}^{(m)})$ implies $\mathcal{E}(\boldsymbol{x}^* + \alpha^*\boldsymbol{d}^*) = \mathcal{E}(\boldsymbol{x}^*)$, where $\boldsymbol{d}^* = [\boldsymbol{x}^* - s\nabla\mathcal{E}(\boldsymbol{x}^*)]^+ - \boldsymbol{x}^*$ and $\alpha^* = \arg\min_{\alpha\in[0,\beta]} \mathcal{E}(\boldsymbol{x}^* + \alpha\boldsymbol{d}^*)$. Thus, $\mathcal{E}(\boldsymbol{x}^* + \alpha\boldsymbol{d}^*) \geqslant \mathcal{E}(\boldsymbol{x}^* + \alpha^*\boldsymbol{d}^*) = \mathcal{E}(\boldsymbol{x}^*)$ for all $\alpha \in [0, \beta]$. This also implies $\lim_{\alpha\to 0} \frac{\mathcal{E}(\boldsymbol{x}^* + \alpha\boldsymbol{d}^*) - \mathcal{E}(\boldsymbol{x}^*)}{\alpha} = \nabla\mathcal{E}(\boldsymbol{x}^*)^T\boldsymbol{d}^* \geqslant 0$. Considering inequality (5.18), $\boldsymbol{d}^*$ has to be 0, i.e.,

$$[\boldsymbol{x}^* - s\nabla\mathcal{E}(\boldsymbol{x}^*)]^+ = \boldsymbol{x}^*. \tag{5.20}$$

According to the property of projection (5.17), $(\boldsymbol{x}^* - (\boldsymbol{x}^* - s\nabla\mathcal{E}(\boldsymbol{x}^*))^T(\boldsymbol{x} - \boldsymbol{x}^*) \geqslant 0, \forall \boldsymbol{x} \in \boldsymbol{X}$, which is equivalent to

$$\nabla\mathcal{E}(\boldsymbol{x}^*)^T(\boldsymbol{x} - \boldsymbol{x}^*) \geqslant 0, \forall \boldsymbol{x} \in \boldsymbol{X}. \tag{5.21}$$

Thus, the point $\boldsymbol{x}^*$ is stationary. □

Proposition 5.2 demonstrates that for the projected gradient algorithm, the point of convergence always exists and is stationary. In addition, a point $\boldsymbol{x}^*$ is stationary if and only if $\boldsymbol{x}^* = [\boldsymbol{x}^* - s\nabla\mathcal{E}(\boldsymbol{x}^*)]^+$ for all $s > 0$. Thus, we stop the algorithm if the norm of $[\boldsymbol{x}^{(m)} - s\nabla\mathcal{E}(\boldsymbol{x}^{(m)})]^+ - \boldsymbol{x}^{(m)}$ is less than a small threshold value. As the local minimum point must be stationary, the minimum point among all the stationary points is the global minimum point. Based on this fact, in the next subsection, the multistart method is utilized to search all the stationary points and treats the point with the minimum value of the objective function as the global minimum point.

5.2.2 *Multistart Method*

The multistart method tries to search all the stationary points by means of implementing the projected gradient method at randomly selected initial points. The procedure of the multistart method is listed in Algorithm 4. The key part of the multistart method is the stopping rule. According to Proposition 5.1, the algorithm will be stopped if the expected number of the stationary points is close to the number of the stationary points already found and the nonobserved regions of $\boldsymbol{X}$ is very small.

Algorithm 4: Multistart method

Input: The target DDP $\mu(x) = \sum_{i=1}^{K} \mu_i x^i$
Result: $\boldsymbol{x}_o = [\boldsymbol{\theta}_o^T \boldsymbol{\omega}_o^T]^T$
Construct a set $\boldsymbol{C}$ which stores the stationary points;
for $n = 1$ *to* N_{max} **do**
  Draw a point randomly over $\boldsymbol{X}$ following the uniform distribution;
  Apply the projected gradient method described in Sect. 5.2.1 to the new sample point and generate a stationary point $\boldsymbol{x}_n^*$;
  if $\boldsymbol{x}_n^* \notin \boldsymbol{C}$ **then** add $\boldsymbol{x}_n^*$ to $\boldsymbol{C}$: Compute w which equals the cardinality of $\boldsymbol{C}$;
  if $\frac{w(n-1)}{n-w-2} - w \leqslant 0.5$ *and* $\frac{w(w+1)}{n(n-1)} \leqslant 0.005$ **then** break
end
Output $\boldsymbol{x}_o = \arg\min_{\boldsymbol{x} \in \boldsymbol{C}} \mathcal{E}(\boldsymbol{x})$;

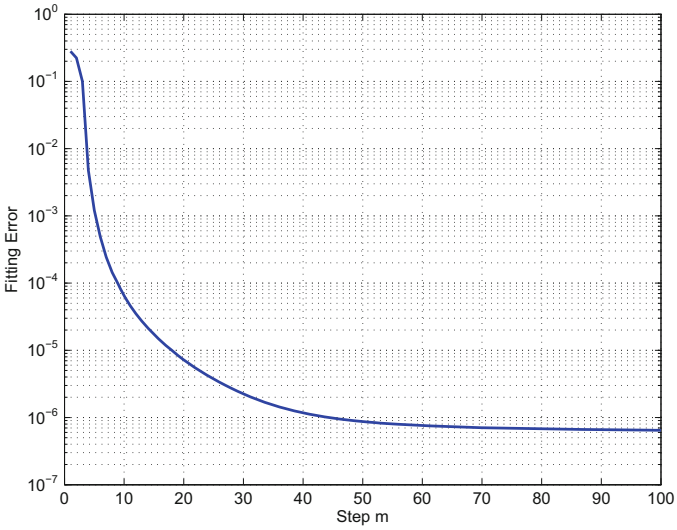

Fig. 5.1 The curve of the fitting error with respect to step m

5.2.3 *Nonnegative Polynomial Decomposition Results*

To evaluate the effectiveness of the proposed algorithm, we provide the decomposition results for both smooth and nonsmooth DDPs. The smooth ISD with $K = 1000$ is considered first. s and β are chosen to be 1. The decomposition results show that multiple stationary points are found during the global phase. Two stationary points $\boldsymbol{x}_i^*$ and $\boldsymbol{x}_j^*$ are treated to be different if the root mean square (RMS) of $\boldsymbol{x}_i^* - \boldsymbol{x}_j^*$ is larger than 10^{-3}. The algorithm stops when nine stationary points are found after searching 192 initial points. Based on this fact, the posterior expected number of stationary points is 9.5, and the posterior expected portion of the uncovered region of attraction is 0.0025, which meet the stopping rule. The fitting error of the nine stationary points

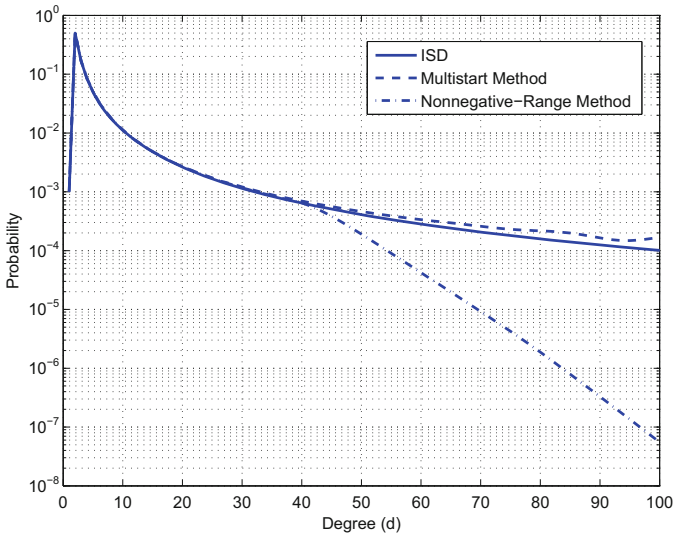

Fig. 5.2 The resultant DDPs obtained from the multistart method using the projected gradient method as the local phase and the nonnegative-range method by decomposing the ISD. The fitting error of the multistart method is 4.64×10^{-7}, which is smaller than the fitting error of the nonnegative-range method 1.13×10^{-4}. The parameters are $K = 1000$, $D_\theta = 25$, and $D_\omega = 40$

Table 5.1 DDP comparison with ISD

Code type	Fidelity	Kolmogorov	Total variation	Kullback–Leibler
Nonnegative-range method	0.9926	0.0191	0.0191	0.3865
Multistart method	0.9972	0.0060	0.0061	0.2027
ISD	1	0	0	0

are 7.54×10^{-7}, 7.04×10^{-7}, 7.11×10^{-7}, 5.85×10^{-7}, 6.76×10^{-7}, 6.01×10^{-7}, 6.25×10^{-7}, 4.64×10^{-7}, and 5.84×10^{-7} which are very close. The stationary point with the lowest fitting error 4.64×10^{-7} is chosen to be the global minimum point. For a randomly selected initial point, the curve of the fitting error $\mathcal{E}$ with respect to step m is plotted in Fig. 5.1. The figure validates that the projected gradient method is effective and the point of convergence exists. Figure 5.2 compares the resultant DDPs obtained from the proposed optimization method and the nonnegative-range method in [3]. It can be observed that the multistart method gives much better approximation toward the ISD compared with the nonnegative-range method for higher-order terms. Table 5.1 shows the results of other metrics to compare the resultant DDPs $\hat{\mu}(x)$ and the target ISD, namely, fidelity $\left(\sum_i \sqrt{\hat{\mu}_i \mu_i}\right)$, Kolmogorov distance $\left(\sup_x |\sum_{i=1}^{x} \hat{\mu}_i - \sum_{i=1}^{x} \mu_i|\right)$, total variation distance $\left(\frac{1}{2}\sum_i |\hat{\mu}_i - \mu_i|\right)$, and Kullback–Leibler divergence $\left(\sum_i \mu_i \log \frac{\mu_i}{\hat{\mu}_i}\right)$, all of which confirm that the multistart method provides more accurate polynomial decomposition.

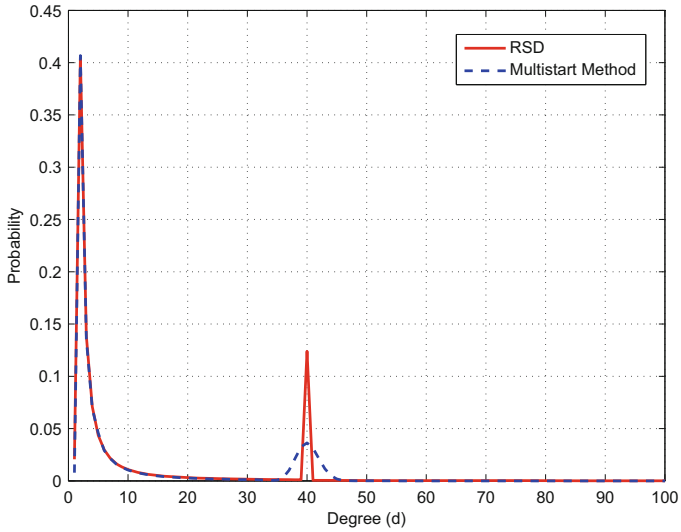

Fig. 5.3 The resultant DDP obtained from the multistart method using the projected gradient method as the local phase by decomposing the RSD

Next, we decompose the nonsmooth RSD which has a spike at the degree K/R. As observed in [3], the nonnegative-range method fails to decompose the RSD as the spike leads to invalid results of range calculation. On the contrary, the multistart method using the projected gradient method as the local phase can provide an optimal decomposition solution for the RSD. The parameters of the target RSD is $K = 1000$, $c = 0.08$, and $\delta = 0.05$. With $D_\theta = 25$ and $D_\omega = 40$, it is found that the algorithm stops after searching 781 initial points, where the total number of stationary points found is 19. Based on this result, the posterior expected number of stationary points is 19.5 and the posterior expected portion of the uncovered region of attraction is 6.24×10^{-4}, which meet the stopping rule. The optimal decomposition result is shown in Fig. 5.3. It is observed that the resultant DDP $\hat{\mu}(x)$ does not fit well at the position of the spike and the higher fitting error $\mathcal{E} = 1.09 \times 10^{-2}$ is incurred.

In summary, the stochastic multistart method using the projected gradient method as the local phase can provide more accurate decomposition results compared with the nonnegative-range method and the linear programming method. The decomposition performance of the multistart method depends on the shape of the given polynomial. For the smooth DDPs such as the ISD, they can be decomposed with small fitter error. However, for the nonsmooth DDPs such as the RSD which are intrinsically indecomposable for the nonnegative-range method, the multistart method can do its best to provide an optimal solution with some higher fitting error.

5.3 h-DLT Codes

To obtain more accurate RSD decomposition and flexible computational cost allocation between the source and the relay(s), h-DLT codes are designed recently by extracting a decomposable part out of the distribution $\mu(x)$ without the spike for two-layer DLT encoding, while the remaining spike distribution remains one-layer LT encoding [3]. The output degree distribution of the h-DLT codes can retain that of the RSD, and thus the decoding performance can be improved over pure DLT codes. However, the second layer of the original h-DLT codes has high average encoding degree. When the h-DLT codes are implemented into dual-hop relay networks, a large number of source packets need to be received at the relay node to generate sufficient h-DLT packets, which implies higher communication cost. In this section, we design a new type of h-DLT codes with improved energy efficiency in dual-hop relay networks. The new h-DLT II codes are constructed based on the new decomposition algorithm proposed in the previous section.

5.3.1 h-DLT I Codes

The original h-DLT codes, namely, h-DLT I, are proposed in [3] with the encoding process given as follows:

(a) At the first-layer encoder, a binary random number generator is adopted to select an encoding mode. With probability η, the encoder will choose the cooperative DLT mode and generate a DLT-1 packet with encoding DDP $\theta_1(x)$; with probability $1-\eta$, the encoder will operate in the direct LT mode, and an LT packet is encoded with encoding DDP $\theta_0(x)$. All coded packets are labeled and sent to the second-layer encoder.
(b) At the second-layer encoder, an encoding degree d is chosen with the DDP $\omega(x)$. Then, d packets are randomly chosen from the inputs. If all the selected packets are labeled as DLT-1, they are XORed together to generate an h-DLT packet; otherwise, one LT packet is output as an h-DLT packet.

With this hybrid encoding scheme, the resultant degree distribution of the second-layer encoder is $\hat{\mu}(x) = \omega(\eta\theta_1(x)) + (1-\omega(\eta))\theta_0(x)$, within which $\mu_1(x) = \omega(\eta\theta_1(x))$ and $\mu_0(x) = (1-\omega(\eta))\theta_0(x)$ are the resultant DDPs of the cooperative DLT mode and the direct LT mode, respectively. The average encoding degrees of the first-layer encoder and the second-layer encoder are $C_1 = \eta\theta_1'(1) + (1-\eta)\theta_0'(1)$ and $C_2 = 1-\omega(\eta) + \eta\omega'(\eta)$, respectively. Define the mode ratio $\gamma = \mu_1(1)/\hat{\mu}(1)$ as the portion of the total distribution assigned to the cooperative DLT mode. For h-DLT I codes, the mode ratio is $\gamma = \omega(\eta)$, which is a nonlinear function of the encoding ratio η. For the RSD with $K = 1000$, $c = 0.08$, and $\delta = 0.05$, the mode ratio and the encoding ratio are listed in Table 5.2 after h-DLT I codes decomposition. It is observed that the h-DLT codes have very high encoding ratios

Table 5.2 Average encoding degree

Code type	η	C_1	C_2	Ratio (C_1/C_2)
h-DLT I ($\gamma = 0.8$)	0.95	2.85	3.47	0.82
h-DLT I ($\gamma = 0.6$)	0.92	2.94	3.06	0.96
h-DLT I ($\gamma = 0.4$)	0.86	3.58	2	1.79
h-DLT II ($\gamma = 0.8$)	0.8	8.93	2.77	3.22
h-DLT II ($\gamma = 0.6$)	0.6	9.61	2.33	4.12
h-DLT II ($\gamma = 0.4$)	0.4	10.29	1.89	5.44
Primitive LT codes	–	11.64	–	–

which are larger than 0.9. This means there is a large probability for the first-layer encoder choosing the DLT mode. As the DDP of the DLT mode has much smaller average encoding degree compared with that of the LT mode which retains the spike of the RSD, i.e., $\theta_1'(1) \ll \theta_0'(1)$, the first-layer encoder has the small average encoding degree, and more encoding cost is placed on the second-layer encoder. The average encoding degrees of the h-DLT I codes are also given in Table 5.2. From the table, it is found that the average encoding degree of the second-layer encoder is around 3. This means on average the relay needs three encoded packets from the source to generate one h-DLT packet.

The h-DLT I codes assisted cooperative communications protocol is proposed in [3]. The source encodes the raw packets according to the first-layer DDP, while the relay encodes with the second-layer DDP. To obtain similar decoding performance as the primitive LT codes, the relay has to combine C_2 packets on average from the source for each generated h-DLT packet. Thus, the average encoding degree (C_2) at the relay implies high communication cost.

The new h-DLT II codes are designed to have smaller average encoding degree at the second-layer encoder. The h-DLT II codes assign higher probability to the LT mode, which increases the average encoding degree of the first-layer encoder considerably and reduces the encoding cost of the second-layer encoder accordingly. In the following, the detailed code design is described.

5.3.2 h-DLT II Codes

5.3.2.1 Encoding Description

The encoding process of h-DLT II codes is also conducted in two steps:

(a) The first step is the same as that of h-DLT I codes.
(b) At the second-layer encoder, for each received packet from the first encoder, if the packet is an LT packet, it is directly output as the h-DLT packet. Otherwise, an encoding degree d is chosen with distribution $\omega(x)$. Then, d DLT-1 packets randomly selected from the inputs are XORed together to generate an h-DLT packet.

5.3.2.2 Resultant Degree Distribution

For an h-DLT II code with a first-layer encoding DDP $\theta(x) = \eta\theta_1(x) + (1-\eta)\theta_0(x)$ and a second-layer DDP $\omega(x)$, the resultant degree distribution $\hat{\mu}(x)$ is computed as

$$\hat{\mu}(x) = \eta\omega(\theta_1(x)) + (1-\eta)\theta_0(x). \tag{5.22}$$

The average encoding degrees of the first-layer encoder (C_1) and the second-layer encoder (C_2) are

$$C_1(\eta) = \theta^{'}(1) = \eta\theta_1^{'}(1) + (1-\eta)\theta_0^{'}(1) \tag{5.23}$$

$$C_2(\eta) = (1-\eta) + \eta\omega^{'}(1) = \eta(\omega^{'}(1) - 1) + 1. \tag{5.24}$$

Differentiating (5.22) and setting $x = 1$, $\theta_0^{'}(1)$ can be computed as

$$\theta_0^{'}(1) = \frac{\mu^{'}(1) - \eta\omega^{'}(1)\theta_1^{'}(1)}{1-\eta}. \tag{5.25}$$

Substituting (5.25) into (5.23), we get

$$C_1(\eta) = \theta_1^{'}(1)(1-\omega^{'}(1))\eta + \mu^{'}(1). \tag{5.26}$$

As $\omega^{'}(1) > 1$, C_1 in (5.26) is a linearly decreasing function of encoding ratio η. Similarly, C_2 in (5.24) is a linearly increasing function of encoding ratio η.

Denote the resultant DDPs of the cooperative DLT mode and the direct LT mode as $\mu_1(x)$ and $\mu_0(x)$. From (5.22), it can be obtained that $\mu_1(x) = \eta\omega(\theta_1(x))$ and $\mu_0(x) = (1-\eta)\theta_0(x)$. h-DLT I codes have limited control of the mode ratio γ, while h-DLT II codes have full control of the mode ratio as $\gamma = \eta$. Thus, h-DLT II codes could flexibly change the average encoding degree, C_1 and C_2 at each layer depending on the requirements.

5.3.3 *Distribution Decomposition for h-DLT II Codes*

In order to facilitate the single-layer BP decoding of the h-DLT packets, a target RSD $\mu(x)$ needs to be decomposed into three distributions: $\theta_1(x)$, $\theta_0(x)$, and $\omega(x)$. Note that only the DLT mode DDP $\mu_1(x)$ needs to be further decomposed. We can determine a proper decomposable $\mu_1(x)$ for the cooperative DLT encoding and decompose it using Algorithm 4. Then, the remaining distribution $\mu(x) - \mu_1(x)$ is assigned to $\theta_0(x)$ for the direct LT mode. This gives rise to the hybrid RSD decomposition algorithm for h-DLT II codes, which is described in Algorithm 5.

Algorithm 5: Hybrid RSD decomposition

Input: The target degree RSD distribution $\mu(x)$ and the desired mode ratio γ_d
Result: The decomposed DDPs $\theta_1(x)$, $\theta_0(x)$, and $\omega(x)$
Initialization: Construct a smooth distribution $\tilde{\mu}(x) = (\rho(x) + \tilde{\tau}(x))/\beta$ with $\tilde{\tau}(x) = \sum_{i=1}^{k/R}(R/ik)x^i$;
(1) Compute $\mu_1(x) = \tilde{\mu}(x)/\tilde{\mu}(1)$;
(2) Decompose $\mu_1(x)$ into $\theta_1(x)$ and $\omega(x)$ using Algorithm 4;
(3) Calculate $\theta_0(x) = (\mu(x) - \gamma_d\omega(\theta_1(x)))/(1 - \gamma_d)$.

One advantage of the hybrid RSD decomposition algorithm for h-DLT II codes is that only one iteration is needed. In contrast, the hybrid RSD decomposition algorithm for h-DLT I codes needs several iterations with each iteration performing a degree distribution decomposition until the exact mode ratio is reached.

5.3.4 h-DLT II Codes Performance

For a target RSD $\mu(x)$ with parameters $K = 1000$, $c = 0.08$, and $\delta = 0.05$, the corresponding h-DLT II distributions $\theta(x)$ and $\omega(x)$ are computed using Algorithm 5, and the resultant distribution $\hat{\mu}(x)$ can be calculated according to (5.22). The fitting error calculation shows that $\mathcal{E}_{\text{h-DLT II}} = 0$ for all γ value, which means the hybrid RSD decomposition algorithm for h-DLT II codes generates exactly the same distribution as the RSD. In Fig. 5.4, we simulate the probability of successful decoding with respect to different decoding overheads for the primitive LT code, the DLT code, and the h-DLT II codes. For the DLT code, we set $D_\theta = 25$ and $D_\omega = 40$ to decompose the target RSD, whose decomposition result has been given in Sect. 5.2.3. It can be observed that the h-DLT II codes achieve similar decoding performance to the primitive LT code, same as h-DLT I codes [3]. The DLT code requires higher overhead compared with the primitive LT codes and the h-DLT II codes because the resultant degree distribution of the DLT code suppresses the spike of the RSD as seen in Fig. 5.3. The mode ratio γ and the encoding ratio η are listed in Table 5.2. It can be seen that the h-DLT II codes have much smaller encoding ratio than the h-DLT I codes for a given mode ratio. Thus, the h-DLT II codes have higher probability to choose the LT mode, resulting in higher average encoding degree at the first-layer encoder and smaller average encoding degree at the second-layer encoder compared with the h-DLT I codes.

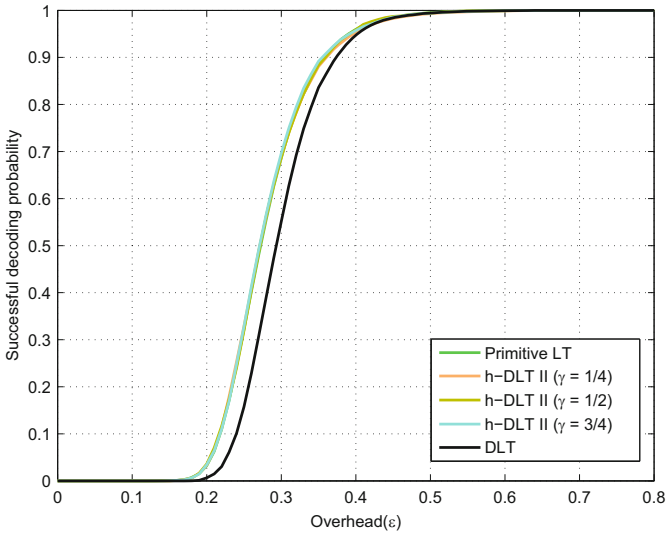

Fig. 5.4 The average recovery ratio with respect to different overhead for the primitive LT code, the DLT code, and the h-DLT II codes

5.4 h-DLT II Codes Assisted Cooperative Communications Protocol

Consider the cooperative communication system as shown in Fig. 5.5, where relay(s) are employed to collaboratively deliver the packet-wise information from the source to the destination. Time division multiple access (TDMA) is adopted as the multiple access method, i.e., the source and the relay(s) transmit packets in turn at different time slots so that the packet transmissions from the source and the relay(s) are interference-free with each other. We assume the source cannot directly communicate with the destination due to the blocking between them and each relay has limited storage capacity to buffer the received packets from the source. Given the mode ratio γ and the RSD, we can obtain the encoding DDPs $\theta_1(x)$, $\theta_0(x)$, and $\omega(x)$ through Algorithm 5. The h-DLT II codes assisted cooperative communications protocol consists of three parts: source encoding and broadcast, relay encoding and forwarding, and destination decoding.

1. *Source encoding and broadcast*: With K data packets to be transmitted, the source generates encoded packets using the first-layer DDP $\theta(x) = \gamma\theta_1(x) + (1 - \gamma)\theta_0(x)$. A mode type ID bit is attached to each encoded packet to indicate its encoding mode: LT (ID $=$ 0) or DLT-1 (ID $=$ 1). The encoded packets are continually generated and broadcast to the relays at the source's transmission time slots until an ACK is received from the relays.

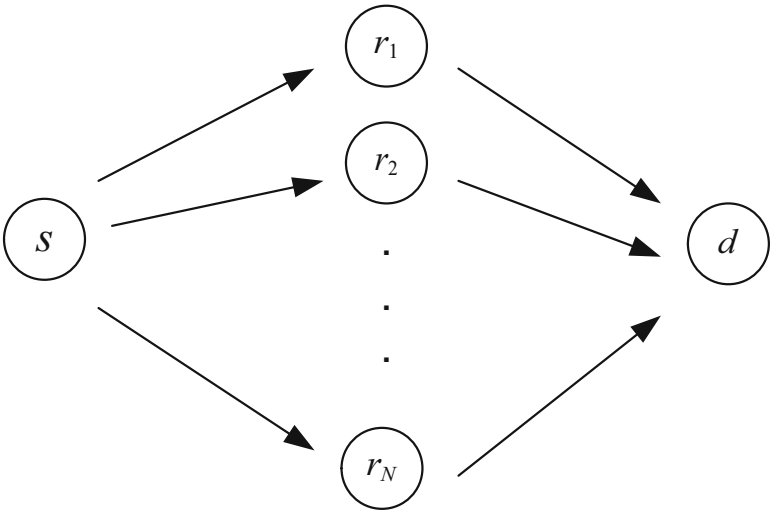

Fig. 5.5 A cooperative relay system with one source, N relays, and one destination

2. *Relay encoding and forwarding*: After receiving the packet from the source, each relay undergoes an error detection process, e.g., cyclic redundancy check (CRC) at the physical layer. If CRC succeeds, the packet is further processed and the packet ID is retrieved: the received packet with ID $= 0$ is treated as the h-DLT packet with ID $= 0$ without storage, while the received packet with ID $= 1$ is stored in the memory, and an h-DLT packet with ID $= 1$ is generated from storage. The generation of the h-DLT packet with ID $= 1$ consists of two steps: First, an encoding degree d is randomly chosen according to distribution $\omega(x)$ and second, d DLT-1 packets from storage are XORed together to generate an h-DLT packet. It is possible that the generated packet has zero encoding degree due to the packet collision. In this case, the above process is repeated until an h-DLT packet with nonzero encoding degree is generated. If CRC fails, the packet is dropped, and an h-DLT packet with ID $= 1$ is generated from storage. Each relay keeps forwarding h-DLT packets attached with their mode type ID bit to the destination in its own time slots until an ACK is received from the destination. The received ACK is also forwarded to the source by the relays.
3. *Destination decoding*: After receiving the packet from the relay(s), the destination undergoes an error detection process similar to the process at the relay(s). Depending on the mode type ID of the received h-DLT packet, the destination chooses the corresponding reception technique. For the h-DLT packet with ID $= 0$, joint decoding is performed at the physical layer, as relays may forward the same packet when the source broadcasts the LT packet. Any cooperative transmission schemes, e.g., MRC, can be adopted to enhance the communication reliability; for each h-DLT packet with ID $= 1$, independent decoding is conducted. After CRC checks, all correctly received packets are forwarded to the

BP decoder to recover the source packets, and all packets with error are deleted. If all K source packets are decoded, an ACK is sent back to the relays.

In practical systems, the relays have limited storage capacity. When the storage space is full, one packet has to be discarded in the storage space to accommodate the newly arrived packet. Here we discuss two storage schemes to handle this scenario. In storage scheme I, the newly arrived packet always replaces the packet which stays longest in the storage space. In the storage scheme II, the packet which is mostly used is replaced. Each packet in the storage space is assigned a counter, and the counter value increases by one, when the packet is selected for encoding. The newly arrived packet replaces the packet with the largest counter value, and the counter is reset to zero for the new packet.

5.5 Performance Evaluations

In this section, we simulate the h-DLT II codes assisted cooperative communications protocol. We assume the source-relay link and the relay-destination link are lossy and have the same packet erasure probability. The performance is evaluated by collecting the average number of transmissions per source packet for full recovery of all data at the destination. The results are compared with those of the h-DLT I codes based schemes to illustrate the benefits of h-DLT II codes. In addition, the effects of different design parameters are also evaluated through simulations.

5.5.1 h-DLT Codes Comparison and Choice of Storage Schemes

In Fig. 5.6, we simulate the communication cost of the cooperative relay communications protocols based on both h-DLT codes with different storage schemes. The communication cost is evaluated by the average number of transmissions per packet with mode ratio $\gamma = 0.5$ and storage size of 50.

The results are plotted in Fig. 5.6. It can be observed that the h-DLT II codes assisted scheme requires less communication cost compared with the h-DLT I codes assisted cooperative communication scheme. As discussed in Sect. 5.3.1, their performance distinction comes from the difference of their second-layer average encoding degree. In addition, the storage scheme II shows better performance than the storage scheme I, especially for h-DLT I codes. When the relay storage space is fully occupied, if storage scheme I is implemented, the oldest packet will be replaced by the incoming packet. However, because of the random encoding at the relay, the replaced packet may not have been chosen for encoding, while some other packets staying in the memory may have been encoded multiple times. This will cause either information loss or collision at the destination. On the other hand, by replacing the

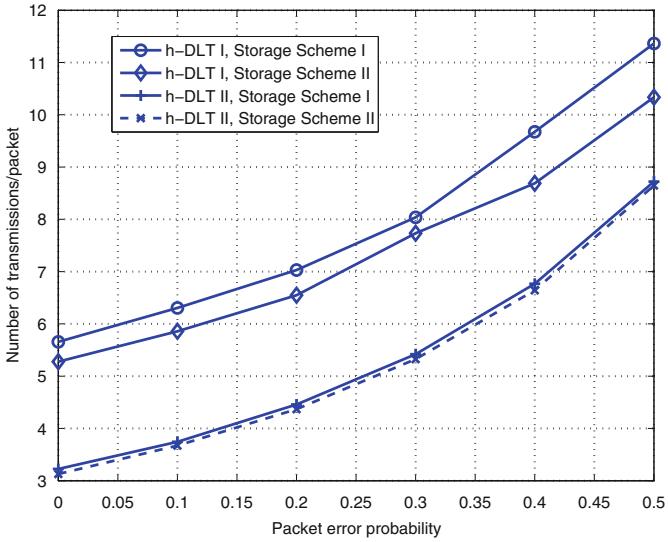

Fig. 5.6 The communication cost for the h-DLT I scheme and the h-DLT II scheme with storage size 50

most used packet, the storage scheme II alleviates this issue and provides better performance.

The storage space is precious for relays. It is found through simulations that the communication cost remains nearly constant with the storage size, which means that the storage size has little influence on the communication cost. Since the storage size cannot be less than the maximum encoding degree of $\omega(x)$, to save the storage space at relays, the best storage size for relays is D_ω.

5.5.2 *Effect of Mode Ratio*

The mode ratio η measures the portion of the cooperative DLT mode in the output distribution. It is notable that $\eta = 0$ corresponds to the primitive LT-based communications protocol with no relay encoding. For the DLT-1 mode, the generated h-DLT packet at the relay can only be obtained by combining the DLT-1 packets in the storage rather than newly generated packets from the source. As a packet in the storage can be selected to generate multiple h-DLT packets, there exists packet redundancy among the generated DLT-encoded packets at the relay, and this could degrade the decoding performance at the destination. Therefore, when the source-relay link is lossless, the large mode ratio results in the degraded performance. On the other hand, for the lossy source-relay link, once the received packet gets erased at the relay(s), a packet encoded by the DLT mode is generated, which means there will be more DLT-encoded packets. Therefore, the large mode ratio can help increase the packet refreshing speed at the relay storage and reduce the

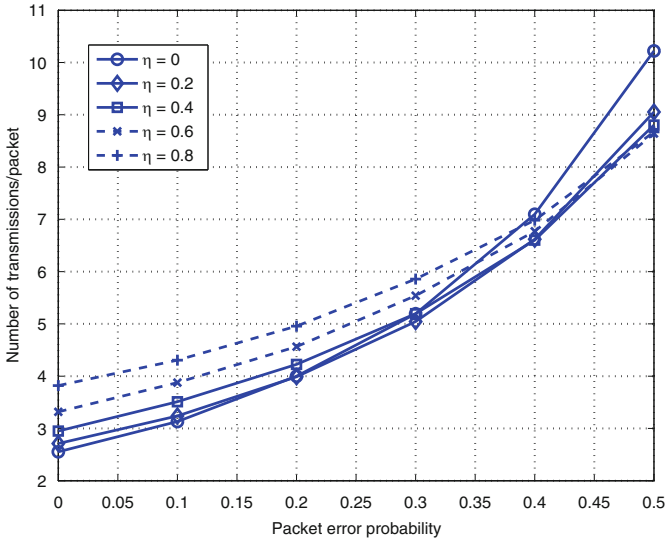

Fig. 5.7 The communication cost of the h-DLT II-based cooperative protocol with different mode ratio η. Storage scheme II is adopted, and the storage size is 50

redundancy among the generated DLT-encoded packet, which can further improve the decoding performance at the destination. In Fig. 5.7, the effect of the mode ratio η is investigated. From the figure, it can be observed that at the lower packet erasure probability, smaller η has lower communication cost, while larger η provides better performance at the high packet erasure probability. This implies that as channel erasure rate increases, more DLT encoding at the relay is beneficial, which confirms h-DLT codes could improve dual-hop reliability by adjusting η.

5.5.3 Effect of Relay Number

In cooperative communications, multiple relays can be implemented to improve the communication reliability. The same setup can be adopted in h-DLT II codes assisted cooperative communication schemes. The source first broadcasts a packet, and then each relay generates and forwards its packet one by one at its own time slot. For the LT mode, the relays forward the same LT packets to the destination, and MRC is implemented at the destination; for the DLT mode, each relay transmits a different encoded packet to the destination, which provides more reliability against channel erasures. As packets forwarded by relays are linear combination of the stored packets from a similar packet storage, there can be redundancy among the packets forwarded by relays. Under good channel condition, the redundancy will degrade the system performance, while under poor channel condition, the redundancy can be utilized to improve the communication reliability.

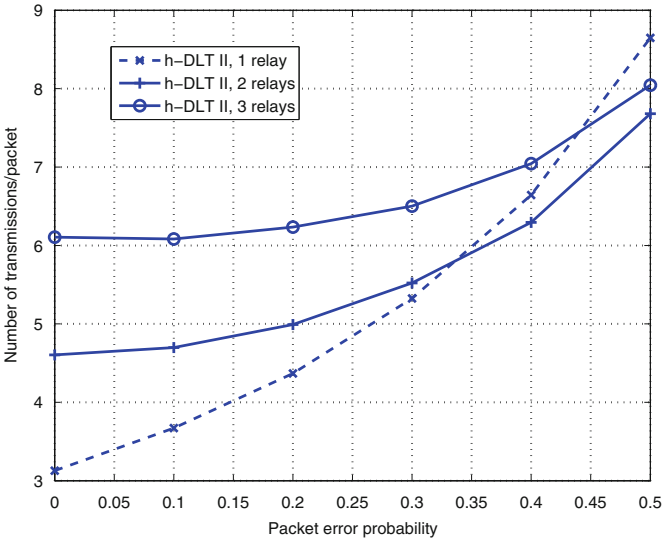

Fig. 5.8 The communication cost of the h-DLT II-based cooperative protocol with different relay numbers

We simulate the MRC operation at the destination as follows. Suppose the BPSK modulation is utilized in the physical-layer transmission and each data bit undergoes independent erasure. With the bit error probability given as $p_b = Q(\sqrt{\gamma})$ where γ is the SNR, the packet erasure probability is $p = 1 - (1 - p_b)^L$, where L is the number of the data bits in the packet. With M LT packets with same information received at the destination, the resultant bit error probability is $\check{p}_b = Q(\sqrt{M\gamma})$ after MRC, and the corresponding packet erasure probability is $\check{p} = 1 - (1 - \check{p}_b)^L$. For example, with $p = 0.1$, $L = 100$, and $M = 2$, the corresponding packet erasure probability after MRC is $\check{p}_b = 6.85 \times 10^{-4}$; with $p = 0.5$, $L = 100$ and $M = 3$, the corresponding packet erasure probability after MRC is $\check{p}_b = 0.001$. Therefore, MRC can reduce the packet erasure probability substantially. With $\gamma = 0.5$ and the storage scheme II, we simulate the performance of the h-DLT II codes assisted cooperative communication systems with different numbers of relay in Fig. 5.8. It can be observed that for small packet erasure probability, the single-relay system provides the best performance, while multi-relay systems have better performance at high packet erasure probability. This confirms that when channel condition gets worse, more relays enhance communication reliability. It is worth noting that the three-relay case has worse performance than the two-relay case at higher packet erasure probability. The degraded performance is caused by much more packet redundancy among the h-DLT packets generated by the relays.

5.6 Summary

In this chapter, we designed a new type of h-DLT codes for cooperative relay communications to improve energy efficiency and accuracy. To facilitate codes construction, a novel nonnegative polynomial decomposition algorithm based on the stochastic multistart method with the projected gradient search as the local phase was proposed for better accuracy and simpler implementation. Our method can also be readily applied to more general polynomial decomposition problem without constraints or with weight. With this decomposition algorithm, the encoding and distribution decomposition schemes for the new type of h-DLT codes, i.e., h-DLT II codes, were presented. Numerical results show that the h-DLT II codes achieve similar performance as the primitive LT codes and simulations reveal that the h-DLT II codes assisted cooperative communications scheme outperforms the h-DLT I codes assisted cooperative communications scheme with much smaller communication cost. In addition, packet storage schemes are investigated, and affecting factor studies indicate that h-DLT II codes assisted cooperative systems are insensitive to the relay storage size and higher mode ratio and larger relay number are beneficial for the cases with large channel erasure rates.

References

1. M. Luby, LT codes, in *Proceedings of 43rd Annual IEEE Symposium on Foundations of Computer Science* (2002), pp. 271–280
2. D. Sejdinovic, R.J. Piechocki, A. Doufexi, AND-OR tree analysis of distributed LT codes, in *Proceedings of IEEE Information Theory Workshop on Networking and Information Theory*, Volos, 10–12 June 2009, pp. 261–265
3. R. Cao, L. Yang, Decomposed LT codes for cooperative relay communications. IEEE J. Select. Areas Commun. **30**(2), 407–414 (2012)
4. K. Zhu, H. Wang, F. Niu, F. Jiang, Decomposed LT codes for cooperative communications. Int. J. Wirel. Inf. Netw. **21**(4), 317–324 (2014)
5. Z.B. Zabinsky, *Stochastic Adaptive Search for Global Optimization*, vol. 72 (Springer, New York, 2003)
6. L. Pál, Global optimization algorithms for bound constrained problems. Ph.D. dissertation, University of Szeged (2011)
7. F. Schoen, Stochastic techniques for global optimization: a survey of recent advances. J. Glob. Optim. **1**(3), 207–228 (1991)
8. R.Y. Rubinstein, D.P. Kroese, *Simulation and the Monte Carlo Method* (Wiley, New York, 2011)
9. L.P. Devroye, Progressive global random search of continuous functions. Math. Program. **15**(1), 330–342 (1978)
10. C.G.E. Boender, The generalized multinomial distribution: a bayesian analysis and applications. Ph.D. dissertation, Erasmus Universiteit Rotterdam (Centrum voor Wiskunde en Informatica, Amsterdam) (1984)
11. A.H.G.R. Kan, G.T. Timmer, Stochastic global optimization methods part I: clustering methods. Math. Program. **39**(1), 27–56 (1987)
12. D.P. Bertsekas, *Nonlinear Programming* (Athena Scientific, Belmont, 1999)
13. E.K.P. Chong, S.H. Zak, *An Introduction to Optimization* (Wiley, New York, 2013)

14. W. Wang, M.A. Carreira-Perpinán, Projection onto the probability simplex: an efficient algorithm with a simple proof, and an application. Technical Report, arXiv preprint. arXiv:1309.1541 (2013)
15. N. Maculan, G.G. de Paula, A linear-time median-finding algorithm for projecting a vector on the simplex of $\mathbb{R}^n$. Oper. Res. Lett. **8**(4), 219–222 (1989)

Chapter 6
Effective ICI Cancellation for OFDM Transmission in RA-UAC

As seen in Chap. 5, the performance of h-DLT codes deteriorates with the packet erasure probability. In UWA channels, large Doppler shifts caused by motion and ocean waves lead to error-prone packet transmissions. To resolve the detrimental effect caused by the Doppler effect, we focus on the effective and low-complexity mirror-mapping-based OFDM transceiver design in this chapter.

6.1 Properties of ICI Coefficients

In this section, the ICI coefficients of the plain OFDM system are investigated in order to guide our proposed ICI cancellation schemes. Assume the multipath Rayleigh fading channels are given by $\boldsymbol{h} = [h_0, h_1, \cdots, h_{L-1}]^T$, where L is the number of channel taps. Each tap is subject to independent Rayleigh fading with $h_l \sim \mathcal{CN}(0, \sigma_l^2)$ for $l \in \{0, 1, \cdots, L-1\}$, where $\mathbb{E}\{|h_l|^2\} = \sigma_l^2$ and $\mathbb{E}\{|h_l|^4\} = 2\sigma_l^4$. When $L = 1$, the multipath Rayleigh fading channel is reduced to the flat fading channel. We also assume that in the rest of this chapter, the major Doppler effect has been removed through received signal resampling and only residual CFO exists [1].

In multipath Rayleigh fading channels, the received baseband signals in the TD are given by

$$y_n = \frac{1}{N} \sum_{k=0}^{N-1} H_k X_k e^{j2\pi n(k+\varepsilon)/N} + \omega_n, \quad n = 0, 1, \cdots, N-1, \tag{6.1}$$

where H_k is the CFR at subcarrier k, ω_n is the noise, and ε is the CFO.

X. Cheng et al., *Cooperative OFDM Underwater Acoustic Communications*,
Wireless Networks, DOI 10.1007/978-3-319-33207-9_6

After FFT, the received signals in the FD can be expressed as

$$Y_m = S_0 H_m X_m + \sum_{k=0, k\neq m}^{N-1} S_{k-m} H_k X_k + W_m, m = 0, 1, \cdots, N-1, \tag{6.2}$$

where W_m is the noise in the FD and

$$S_k = \frac{\sin(\pi\varepsilon)}{N \sin(\pi(k+\varepsilon)/N)} e^{j\left(\pi\varepsilon\left(1-\frac{1}{N}\right)-\frac{\pi k}{N}\right)} \tag{6.3}$$

is the ICI coefficient [2, 3].

The ICI coefficient S_k is a periodic function with period N. The amplitude and the phase of S_k are plotted in Figs. 6.1 and 6.2 with $\varepsilon = 0.1$ and $N = 1000$. It can be observed that for large values of $|k|$, $|S_k|$ goes to 0. This means ICI mainly comes from neighboring subcarriers. The phase of S_k is $\angle S_k = \pi\left[\varepsilon\left(1-\frac{1}{N}\right) - \frac{k\%N}{N}\right]$ for $0 < \varepsilon < 1$. Thus, for small values of $|k|$, $\angle S_k \approx \pi\varepsilon$ and $\angle S_{-k} \approx \pi\varepsilon - \pi$. This implies $S_k + S_{-k} \approx 0$. In addition, for small values of ε, $\angle S_k \approx 0$ and $\angle S_{-k} \approx -\pi$. This means $S_k + S_{-k}^* \approx 0$. It is worth noting that $S_k + S_{-k} \approx 0$ is a more accurate approximation than $S_k + S_{-k}^* \approx 0$. As we will see in the next sections, the mirror-mapping-based schemes are designed on the basis of the aforementioned properties.

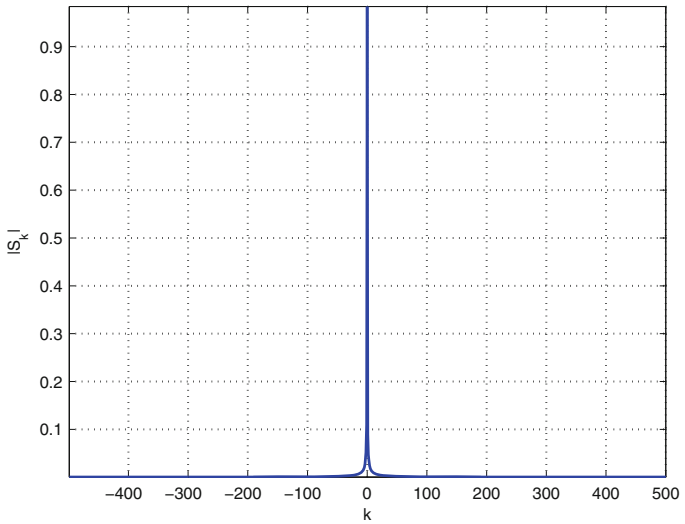

Fig. 6.1 The amplitude of S_k

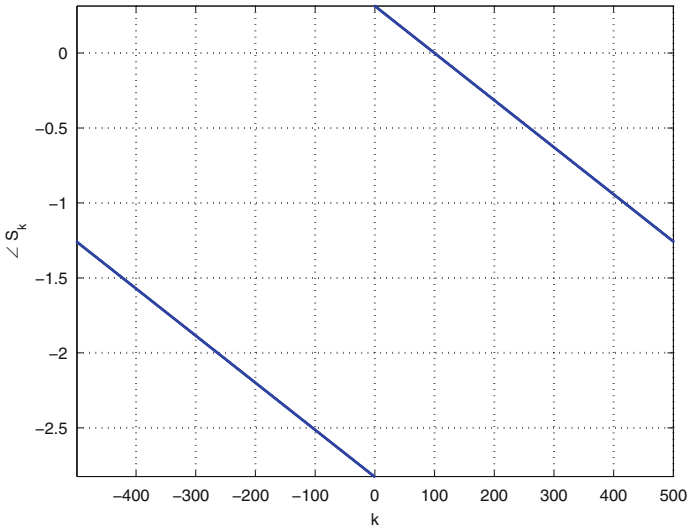

Fig. 6.2 The phase of S_k

6.2 Proposed ICI Cancellation Schemes

This section introduces two methods to cancel ICI, namely, ICI self-cancellation with mirror-mapping and ICI two-path cancellation with mirror-mapping.

6.2.1 ICI Self-Cancellation with Mirror-Mapping

Figure 6.3 depicts the system architecture of the ICI self-cancellation schemes with mirror-mapping. Compared with the plain OFDM, the ICI self-cancellation schemes have two additional modules, i.e., the ICI self-canceling modulation before the IFFT operation at the transmitter and the ICI self-canceling demodulation after the FFT operation at the receiver.

For the ICI self-canceling modulation, the input-modulated data symbols are first grouped into transmit blocks. Each block consists of $(N/2-1)$ modulated data symbols $\{X\}_{k=1}^{N/2-1}$, which are then mapped onto N subcarriers using the one-to-two mirror-mapping rule as follows:

$$\widetilde{X}_k = \begin{cases} 0, & k = 0, N/2 \\ X_k, & k = 1, 2, \ldots, N/2-1 \\ \mathcal{M}(X_{N-k}), & k = N/2+1, \ldots, N-1, \end{cases} \tag{6.4}$$

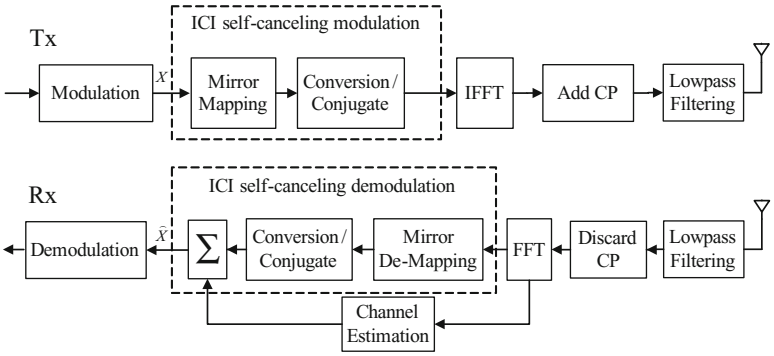

Fig. 6.3 Block diagram of an OFDM transceiver with the ICI self-cancellation modules using mirror-mapping in the baseband

where $\{\widetilde{X}_k\}_{k=0}^{N-1}$ are the actual transmitted data symbols on the OFDM subcarriers. $\mathcal{M}(x)$ is defined as the mapping operation which reflects the relationship between the two modulated data symbols with the same information. It is worth noting that $\widetilde{X}_{N-k} = \mathcal{M}(\widetilde{X}_k), k = 1, 2, \ldots, N/2-1$ represents mirror-mapping. The conversion operation and the conjugate operation can be represented as $\mathcal{M}(x) = -x$ and $\mathcal{M}(x) = x^*$, respectively. The 0th and $N/2$th subcarriers are vacant in order to meet the opposite polarity condition. Thus, we have the MSR scheme and the MCSR scheme, corresponding to the conversion operation and the conjugate operation, respectively.

After the ICI self-canceling demodulation, the received signals on subcarrier $m, m \in \{1, 2, \ldots N/2-1\}$ and its corresponding mapped subcarrier pair ($m' = N - m$) will carry the same data information. This signal redundancy renders it possible to improve the ICI mitigation performance through a coherent combining technique:

$$\widehat{X}_m = \frac{H_m^* Y_m + \mathcal{M}\left(H_{N-m}^* Y_{N-m}\right)}{|H_m|^2 + |H_{N-m}|^2}, \tag{6.5}$$

where H_m, H_{N-m}, Y_m, and Y_{N-m} are the CFR and the received signals at subcarrier m and its corresponding subcarrier pair ($m' = N - m$), respectively. Note that (6.5) is essentially MRC.

6.2.2 ICI Two-Path Cancellation with Mirror-Mapping

Figure 6.4 depicts the system architecture of the ICI two-path cancellation schemes with mirror-mapping. The two-path cancellation schemes transmit the input-modulated data symbols in two consecutive OFDM symbols, which are usually

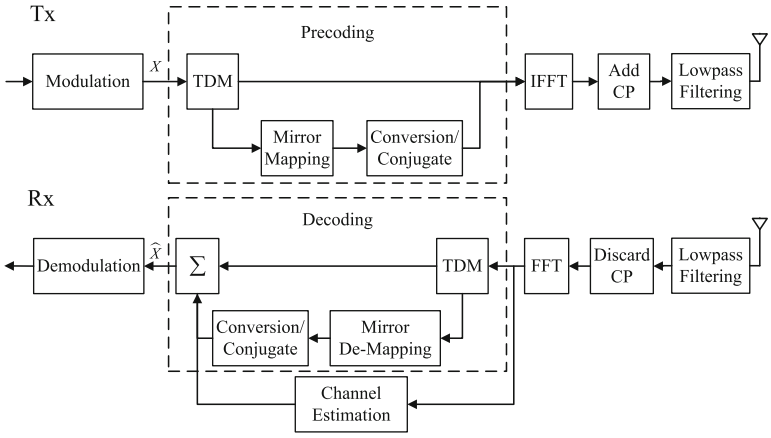

Fig. 6.4 Block diagram of an OFDM transceiver with the ICI two-path cancellation modules using mirror-mapping in the baseband

referred to as two independent paths separated by time division multiplexing (TDM). Evidently, the main additional operations due to the introduction of two-path cancellation schemes are integrated inside the precoding and decoding modules.

In general, for the two-path cancellation schemes with mirror-mapping, at the precoding module, one OFDM symbol input $\{X_k\}_{k=0}^{N-1}$ will become two OFDM symbol outputs $\{\overline{X}_k^{(1)}\}_{k=0}^{N-1}$ and $\{\overline{X}_k^{(2)}\}_{k=0}^{N-1}$, where the first OFDM symbol $\{\overline{X}_k^{(1)}\}_{k=0}^{N-1}$ is identical to the input OFDM symbol, i.e., $\overline{X}_k^{(1)} = X_k$, and the second OFDM symbol $\{\overline{X}_k^{(2)}\}_{k=0}^{N-1}$ obeys the subcarrier mirror-mapping rule and can be obtained as $\overline{X}_k^{(2)} = \mathcal{M}(X_{N-k}), k = \{0, \ldots, N-1\}$. For ease of exposition, if the conversion operation is utilized for the mapping operation, i.e., $\mathcal{M}(x) = -x$, we refer to it as the MCVT scheme, and if the conjugate operation is used, i.e., $\mathcal{M}(x) = x^*$, we call it the MCJT scheme.

After the deliberate design of the transmitted signal in the precoding module, the received signals at the mth subcarrier and the $(N-m)$th subcarrier of the first OFDM symbol and the second OFDM symbol, respectively, will carry the same data information. Therefore, at the decoding module, it is reasonable to use MRC for decoding, yielding

$$\widehat{X}_m = \frac{H_m^* \overline{Y}_m^{(1)} + \mathcal{M}\left\{H_{N-m}^* \overline{Y}_{N-m}^{(2)}\right\}}{|H_m|^2 + |H_{N-m}|^2}, \tag{6.6}$$

where H_m is the CFR at subcarrier m and $\overline{Y}_m^{(i)}$ is the received signals in the FD corresponding to the ith transmitted OFDM symbol ($i \in \{1, 2\}$).

6.3 CIR Evaluation

CIR is a widely used metric for evaluating the system ICI power level without considering the noise power. In this section, we derive the CIRs of the plain OFDM and the proposed mirror-mapping-based schemes for performance comparisons.

6.3.1 Plain OFDM

Suppose that the transmitted data symbols are mutually independent. According to (6.2), the instantaneous CIR of the plain OFDM can be readily derived as

$$\mathrm{CIR}_{\mathrm{OFDM,\,Inst}} = \frac{|S_0 H_m|^2}{\sum\limits_{k=0,k\neq m}^{N-1} |S_{k-m} H_k|^2}. \tag{6.7}$$

The average CIR can be calculated by averaging the above instantaneous CIR expression over the distribution of the channel gains. However, the calculation of the average CIR using multiple integral is overly complicated. Thus, an approximate average CIR expression can be derived by taking the average of the numerator and the denominator of (6.7) separately. As it is a good predictor of the average CIR and simple enough to compare different schemes [4], the approximate average CIR is utilized for the CIR derivation in this chapter. Then, the CIR of the plain OFDM is

$$\mathrm{CIR}_{\mathrm{OFDM}} = \frac{|S_0|^2\, \mathbb{E}\left\{|H_m|^2\right\}}{\sum\limits_{k=0,k\neq m}^{N-1} |S_{k-m}|^2\, \mathbb{E}\left\{|H_k|^2\right\}}. \tag{6.8}$$

As $\mathbb{E}\{|H_k|^2\} = \mathbb{E}\{|H_m|^2\} = \eta$,

$$\mathrm{CIR}_{\mathrm{OFDM}} = \frac{|S_0|^2}{\sum\limits_{k=1,k\neq m}^{N-1} |S_k|^2}. \tag{6.9}$$

6.3.2 MSR

For the MSR scheme, the conversion operation is adopted. The transmitted data symbols in the FD after the ICI self-canceling modulation are $\widetilde{X}_1 = -\widetilde{X}_{N-1} = X_1$,

$\widetilde{X}_2 = -\widetilde{X}_{N-2} = X_2, \ldots, \widetilde{X}_{N/2-1} = -\widetilde{X}_{N/2+1} = X_{N/2-1}$, and $\widetilde{X}_0 = \widetilde{X}_{N/2} = 0$. According to (6.5), the decision variable at the mth subcarrier ($m \in \{1, \cdots, N/2-1\}$) becomes

$$\begin{aligned}\widehat{X}_m &= H_m^* Y_m - H_{N-m}^* Y_{N-m} \\ &= (S_0 |H_m|^2 + S_0 |H_{N-m}|^2 - S_{-2m} H_m^* H_{N-m} - S_{2m} H_{N-m}^* H_m) X_m \\ &+ \sum_{k=1, k\neq m}^{N/2-1} (S_{k-m} H_m^* H_k + S_{m-k} H_{N-m}^* H_{N-k} - S_{-k-m} H_m^* H_{N-k} - S_{m+k} H_{N-m}^* H_k) X_k \\ &+ H_m^* W_m - H_{N-m}^* W_{N-m}.\end{aligned}$$

The factor $1/(|H_m|^2 + |H_{N-m}|^2)$ is removed from the decision variable expression, as it does not affect the CIR value. The CIR at the mth subcarrier is expressed as

$$\mathrm{CIR}_{\mathrm{MSR}}(m) = \frac{\mathbb{E}\left\{\left|S_0(|H_m|^2 + |H_{N-m}|^2) - S_{-2m} H_m^* H_{N-m} - S_{2m} H_{N-m}^* H_m\right|^2\right\}}{\sum_{k=1, k\neq m}^{N/2-1} \mathbb{E}\left\{\left|S_{k-m} H_m^* H_k + S_{m-k} H_{N-m}^* H_{N-k} - S_{-k-m} H_m^* H_{N-k} - S_{m+k} H_{N-m}^* H_k\right|^2\right\}}.$$

For the multipath Rayleigh fading channels, the CIR of the MSR scheme at the mth subcarrier is given by

$$\mathrm{CIR}_{\mathrm{MSR}}(m) = \frac{\sum_{l=0}^{L-1} \sigma_l^4 \left|2S_0 - S_{-2m} e^{j\frac{4\pi}{N} lm} - S_{2m} e^{-j\frac{4\pi}{N} lm}\right|^2}{\sum_{k=1, k\neq m}^{N/2-1} \sum_{l=0}^{L-1} \sigma_l^4 \left|S_{k-m} e^{-j\frac{2\pi}{N}(k-m)l} + S_{m-k} e^{j\frac{2\pi}{N}(k-m)l} - S_{-k-m} e^{j\frac{2\pi}{N}(k+m)l} - S_{k+m} e^{-j\frac{2\pi}{N}(k+m)l}\right|^2} \tag{6.10}$$

and the derivation is given in Sect. 6.3.2.1.

For the flat fading channel, i.e., $L = 1$, the CIR becomes

$$\mathrm{CIR}_{\mathrm{MSR}}(m) = \frac{|2S_0 - S_{2m} - S_{-2m}|^2}{\sum_{k=1, k\neq m}^{N/2-1} \left|S_{k-m} + S_{-(k-m)} - S_{k+m} - S_{-(k+m)}\right|^2}. \tag{6.11}$$

As $S_k + S_{-k} \approx 0$, the CIR of the MSR scheme can be markedly improved.

The average CIR of the MSR scheme is then given by

$$\mathrm{CIR}_{\mathrm{MSR}} = \frac{2}{N-2} \sum_{m=1}^{N/2-1} \mathrm{CIR}_{\mathrm{MSR}}(m). \tag{6.12}$$

6.3.2.1 Derivation of CIR of MSR

The channel response at subcarrier m is given by $H_m = \sum_{l=0}^{L-1} h_l e^{-j\frac{2\pi}{N}ml}$. Accordingly,

$$S_0(|H_m|^2+|H_{N-m}|^2)-S_{-2m}H_m^*H_{N-m}-S_{2m}H_{N-m}^*H_m = \sum_{a=0}^{L-1}\sum_{b=0}^{L-1} h_a^* h_b F_1(a,b),$$

where $F_1(a,b) = S_0 e^{-j\frac{2\pi}{N}(b-a)m} + S_0 e^{j\frac{2\pi}{N}(b-a)m} - S_{-2m}e^{j\frac{2\pi}{N}(a+b)m} - S_{2m}e^{-j\frac{2\pi}{N}(a+b)m}$. Then,

$$\begin{aligned}&\left|S_0(|H_m|^2+|H_{N-m}|^2)-S_{-2m}H_m^*H_{N-m}-S_{2m}H_{N-m}^*H_m\right|^2\\ =&\sum_{a=0}^{L-1}\sum_{b=0}^{L-1}\sum_{c=0}^{L-1}\sum_{d=0}^{L-1} h_a^* h_b h_c h_d^* F_1(a,b)F_1^*(c,d).\end{aligned}$$

The multipath Rayleigh fading channels have the following property:

$$\mathbb{E}\left\{h_a h_b^* h_c h_d^*\right\} = \begin{cases}\mathbb{E}\left\{|h_a|^4\right\}, & a=b=c=d\\ 0, & \text{else.}\end{cases}$$

Based on this property, we can obtain

$$\begin{aligned}&\mathbb{E}\left\{\left|S_0(|H_m|^2+|H_{N-m}|^2)-S_{-2m}H_m^*H_{N-m}-S_{2m}H_{N-m}^*H_m\right|^2\right\}\\ =&\sum_{l=0}^{L-1}\mathbb{E}\left\{|h_l|^4\right\}|F_1(l,l)|^2\\ =&\sum_{l=0}^{L-1}2\sigma_l^4\left|2S_0 - S_{-2m}e^{j\frac{4\pi}{N}lm} - S_{2m}e^{-j\frac{4\pi}{N}lm}\right|^2.\end{aligned}$$

In a similar way,

$$\begin{aligned}&S_{k-m}H_m^*H_k+S_{m-k}H_{N-m}^*H_{N-k}-S_{-k-m}H_m^*H_{N-k}-S_{m+k}H_{N-m}^*H_k\\ =&\sum_{a=0}^{L-1}\sum_{b=0}^{L-1} h_a^* h_b F_2(a,b),\end{aligned}$$

where $F_2(a,b) = S_{k-m}e^{-j\frac{2\pi}{N}(kb-ma)} + S_{m-k}e^{j\frac{2\pi}{N}(kb-ma)} - S_{-k-m}e^{j\frac{2\pi}{N}(kb+ma)} - S_{k+m}e^{-j\frac{2\pi}{N}(kb+ma)}$. Then,

$$\mathbb{E}\left\{\left|S_{k-m}H_m^*H_k+S_{m-k}H_{N-m}^*H_{N-k}-S_{-k-m}H_m^*H_{N-k}-S_{m+k}H_{N-m}^*H_k\right|^2\right\}$$
$$=\sum_{l=0}^{L-1}\mathbb{E}\left\{|h_l|^4\right\}|F_2(l,l)|^2$$

Thus, $\mathrm{CIR}_{\mathrm{MSR}}$ in (6.10) can be obtained.

6.3.3 MCSR

Similarly, for the MCSR scheme, the conjugate operation is adopted. Accordingly, we have $\widetilde{X}_1 = \widetilde{X}_{N-1}^* = X_1, \widetilde{X}_2 = \widetilde{X}_{N-2}^* = X_2, \ldots, \widetilde{X}_{N/2-1} = \widetilde{X}_{N/2+1}^* = X_{N/2-1}$, and $\widetilde{X}_0 = \widetilde{X}_{N/2} = 0$. From (6.5), the decision variable at the mth subcarrier is given by

$$\begin{aligned}\widehat{X}_m &= H_m^*Y_m + H_{N-m}Y_{N-m}^*\\ &= (S_0|H_m|^2+S_0^*|H_{N-m}|^2)X_m+\sum_{k=1,k\neq m}^{N/2-1}(S_{k-m}H_m^*H_k+S_{m-k}^*H_{N-m}H_{N-k}^*)X_k\\ &+\sum_{k=N/2+1}^{N-1}(S_{k-m}H_m^*H_k+S_{m-k}^*H_{N-m}H_{N-k}^*)X_{N-k}^*+H_m^*W_m+H_{N-m}W_{N-m}^*.\end{aligned}$$

Then, the CIR of the MCSR scheme can be expressed as

$$\mathrm{CIR}_{\mathrm{MCSR}}(m) = \frac{\mathbb{E}\left\{\left|S_0|H_m|^2+S_0^*|H_{N-m}|^2\right|^2\right\}}{\sum_{k=1,k\notin\{m,N/2\}}^{N-1}\mathbb{E}\left\{\left|S_{k-m}H_m^*H_k+S_{m-k}^*H_{N-m}H_{N-k}^*\right|^2\right\}}. \tag{6.13}$$

For the multipath Rayleigh fading channels, the CIR of the MCSR scheme is

$$\mathrm{CIR}_{\mathrm{MCSR}}(m) = \frac{4\Re\{S_0\}^2}{\sum_{k=1,k\notin\{N/2-m,N-m\}}^{N-1}|S_k+S_{-k}^*|^2}. \tag{6.14}$$

See Sect. 6.3.3.1 for the detailed derivation. As $S_k + S_{-k}^* \approx 0$, the CIR of the MCSR scheme is improved compared with that of the plain OFDM. Note that the CIR of the MCSR scheme is not affected by the channel length L.

Accordingly, the average CIR of the MCSR scheme is given by

$$\mathrm{CIR}_{\mathrm{MCSR}} = \frac{2}{N-2} \sum_{m=1}^{N/2-1} \mathrm{CIR}_{\mathrm{MCSR}}(m). \tag{6.15}$$

6.3.3.1 Derivation of CIR of MCSR

It can be shown that

$$\begin{aligned} S_0 \left|H_m\right|^2 + S_0^* \left|H_{N-m}^2\right| &= \sum_{a=0}^{L-1} \sum_{b=0}^{L-1} h_a h_b^* (S_0 e^{-j\frac{2\pi}{N}(a-b)m} + S_0^* e^{j\frac{2\pi}{N}(a-b)m}) \\ &= \sum_{a=0}^{L-1} \sum_{b=0}^{L-1} 2h_a h_b^* \Re\left\{S_0 e^{-j\frac{2\pi}{N}(a-b)m}\right\} \end{aligned}$$

and

$$\begin{aligned} \left|S_0 \left|H_m\right|^2 + S_0^* \left|H_{N-m}^2\right|\right|^2 = &\sum_{a=0}^{L-1} \sum_{b=0}^{L-1} \sum_{c=0}^{L-1} \sum_{d=0}^{L-1} 4h_a h_b^* h_c^* h_d \Re\left\{S_0 e^{-j\frac{2\pi}{N}(a-b)m}\right\} \\ &\times \Re\left\{S_0 e^{-j\frac{2\pi}{N}(c-d)m}\right\}. \end{aligned}$$

Thus, for the multipath Rayleigh fading channels, we have

$$\mathbb{E}\left\{(S_0 \left|H_m\right|^2 + S_0^* \left|H_{N-m}^2\right|)^2\right\} = 4\Re\left\{S_0\right\}^2 \sum_{l=0}^{L-1} \mathbb{E}\left\{\left|h_l\right|^4\right\}.$$

In a similar way,

$$S_{k-m} H_m^* H_k + S_{m-k}^* H_{N-m} H_{N-k}^* = \sum_{a=0}^{L-1} \sum_{b=0}^{L-1} e^{-j\frac{2\pi}{N}(kb-ma)} (S_{k-m} h_a^* h_b + S_{m-k}^* h_a h_b^*)$$

and

$$\begin{aligned} \left|S_{k-m} H_m^* H_k + S_{m-k}^* H_{N-m} H_{N-k}^*\right|^2 = &\sum_{a=0}^{L-1} \sum_{b=0}^{L-1} \sum_{c=0}^{L-1} \sum_{d=0}^{L-1} e^{-j\frac{2\pi}{N}[(kb-ma)-(kd-mc)]} \\ &\times (S_{k-m} h_a^* h_b + S_{m-k}^* h_a h_b^*) \\ &\times (S_{k-m}^* h_c h_d^* + S_{m-k} h_c^* h_d). \end{aligned}$$

For the multipath Rayleigh fading channels, we have

$$\begin{aligned}\mathbb{E}\left\{\left|S_{k-m}H_m^*H_k+S_{m-k}^*H_{N-m}H_{N-k}^*\right|^2\right\} &= \sum_{l=0}^{L-1}\mathbb{E}\left\{|h_l|^4\right\}\left(|S_{k-m}|^2+S_{k-m}S_{m-k}\right.\\ &\quad\left.+S_{m-k}^*S_{k-m}^*+|S_{m-k}|^2\right)\\ &= \sum_{l=0}^{L-1}\mathbb{E}\left\{|h_l|^4\right\}\left|S_{k-m}+S_{m-k}^*\right|^2.\end{aligned}$$

Thus, $\mathrm{CIR}_{\mathrm{MCVT}}$ in (6.14) can be obtained.

6.3.4 MCVT

For the MCVT scheme, the conversion operation is adopted. The two consecutive transmitted OFDM symbols are of the form $\overline{X}^{(1)} = [X_0, X_1, \ldots, X_{N-1}]$ and $\overline{X}^{(2)} = [-X_0, -X_{N-1}, \ldots, -X_1]$. From (6.6), the decision variable at the mth subcarrier $(m = 0, \ldots, N-1)$ is given by

$$\begin{aligned}\widehat{X}_m &= H_m^*\overline{Y}_m^{(1)} - H_{N-m}^*\overline{Y}_{N-m}^{(2)} \qquad (6.16)\\ &= \left[S_0(\varepsilon)\left|H_m\right|^2 + S_0(\varepsilon+\Delta\varepsilon)\left|H_{N-m}\right|^2\right]X_m\\ &\quad+\sum_{k=0,k\neq m}^{N-1}\left[S_{k-m}(\varepsilon)H_m^*H_k + S_{m-k}(\varepsilon+\Delta\varepsilon)H_{N-m}^*H_{N-k}\right]X_k\\ &\quad+H_m^*W_m^{(1)} - H_{N-m}^*W_{N-m}^{(2)}, \qquad (6.17)\end{aligned}$$

where the CFO of the first symbol is ε, the CFO of the second symbol is $\varepsilon+\Delta\varepsilon$, and $W_m^{(p)}$ $(p = 1, 2)$ is the noise at the mth subcarrier of the pth path.

According to (6.16), the CIR of the MCVT scheme can be expressed as

$$\mathrm{CIR}_{\mathrm{MCVT}} = \frac{\mathbb{E}\left\{\left|S_0(\varepsilon)\left|H_m\right|^2 + S_0(\varepsilon+\Delta\varepsilon)\left|H_{N-m}\right|^2\right|^2\right\}}{\sum_{k=0,k\neq m}^{N-1}\mathbb{E}\left\{\left|S_{k-m}(\varepsilon)H_m^*H_k + S_{m-k}(\varepsilon+\Delta\varepsilon)H_{N-m}^*H_{N-k}\right|^2\right\}}. \qquad (6.18)$$

For the multipath Rayleigh fading channels, the CIR of the MCVT scheme is

$$\mathrm{CIR}_{\mathrm{MCVT}} = \frac{\left|S_0(\varepsilon)+S_0(\varepsilon+\Delta\varepsilon)\right|^2\sum_{l=0}^{L-1}\sigma_l^4}{\sum_{k=1}^{N-1}\sum_{l=0}^{L-1}\sigma_l^4\left|S_k(\varepsilon)e^{-j\frac{2\pi}{N}kl}+S_{-k}(\varepsilon+\Delta\varepsilon)e^{j\frac{2\pi}{N}kl}\right|^2}. \qquad (6.19)$$

The derivation is given in Sect. 6.3.4.1. Notice that for $kl \ll N$, $S_k e^{-j\frac{2\pi}{N}kl} + S_{-k}e^{j\frac{2\pi}{N}kl} \approx S_k + S_{-k} \approx 0$. Thus, significant CIR improvement can be expected for a small channel length L.

For the flat fading channel, i.e., $L = 1$, the CIR of the MCVT scheme becomes

$$\mathrm{CIR}_{\mathrm{MCVT}} = \frac{|S_0(\varepsilon) + S_0(\varepsilon+\Delta\varepsilon)|^2}{\sum_{k=1}^{N-1} |S_k(\varepsilon) + S_{-k}(\varepsilon+\Delta\varepsilon)|^2}. \tag{6.20}$$

6.3.4.1 Derivation of CIR of MCVT

Since

$$\begin{aligned} &S_0(\varepsilon)\,|H_m|^2 + S_0(\varepsilon+\Delta\varepsilon)\,|H_{N-m}|^2 \\ &= \sum_{a=0}^{L-1}\sum_{b=0}^{L-1} h_a h_b^* \left[S_0(\varepsilon)e^{-j\frac{2\pi}{N}m(a-b)} + S_0(\varepsilon+\Delta\varepsilon)e^{j\frac{2\pi}{N}m(a-b)}\right], \end{aligned}$$

it can be derived that

$$\begin{aligned} \left|S_0(\varepsilon)\,|H_m|^2 + S_0(\varepsilon+\Delta\varepsilon)\,|H_{N-m}|^2\right|^2 &= \sum_{a=0}^{L-1}\sum_{b=0}^{L-1}\sum_{c=0}^{L-1}\sum_{d=0}^{L-1} h_a h_b^* h_c^* h_d \\ &\times \left[S_0(\varepsilon)e^{-j\frac{2\pi}{N}m(a-b)} + S_0(\varepsilon+\Delta\varepsilon)e^{j\frac{2\pi}{N}m(a-b)}\right] \\ &\times \left[S_0^*(\varepsilon)e^{j\frac{2\pi}{N}m(a-b)} + S_0^*(\varepsilon+\Delta\varepsilon)e^{-j\frac{2\pi}{N}m(a-b)}\right]. \end{aligned}$$

For the multipath Rayleigh fading channels, we have

$$\mathbb{E}\left\{\left|S_0(\varepsilon)\,|H_m|^2 + S_0(\varepsilon+\Delta\varepsilon)\,|H_{N-m}|^2\right|^2\right\} = \sum_{l=0}^{L-1}\mathbb{E}\left\{|h_l|^4\right\}|S_0(\varepsilon) + S_0(\varepsilon+\Delta\varepsilon)|^2.$$

In the same way,

$$\begin{aligned} &S_{k-m}(\varepsilon)H_m^* H_k + S_{m-k}(\varepsilon+\Delta\varepsilon)H_{N-m}^* H_{N-k} \\ &= \sum_{a=0}^{L-1}\sum_{b=0}^{L-1} h_a^* h_b \left[S_{k-m}(\varepsilon)e^{-j\frac{2\pi}{N}(kb-ma)} + S_{m-k}(\varepsilon+\Delta\varepsilon)e^{j\frac{2\pi}{N}(kb-ma)}\right] \end{aligned}$$

and

$$\begin{aligned}
&\left|S_{k-m}(\varepsilon)H_m^*H_k + S_{m-k}(\varepsilon+\Delta\varepsilon)H_{N-m}^*H_{N-k}\right|^2 \\
=&\sum_{a=0}^{L-1}\sum_{b=0}^{L-1}\sum_{c=0}^{L-1}\sum_{d=0}^{L-1} h_a^*h_bh_ch_d^* \\
\times&\left[S_{k-m}(\varepsilon)e^{-j\frac{2\pi}{N}(kb-ma)} + S_{m-k}(\varepsilon+\Delta\varepsilon)e^{j\frac{2\pi}{N}(kb-ma)}\right] \\
\times&\left[S_{k-m}^*(\varepsilon)e^{j\frac{2\pi}{N}(kd-mc)} + S_{m-k}^*(\varepsilon+\Delta\varepsilon)e^{-j\frac{2\pi}{N}(kd-mc)}\right].
\end{aligned}$$

For the multipath Rayleigh fading channels, we have

$$\begin{aligned}
&\mathbb{E}\left\{\left|S_{k-m}(\varepsilon)H_m^*H_k + S_{m-k}(\varepsilon+\Delta\varepsilon)H_{N-m}^*H_{N-k}\right|^2\right\} \\
=&\sum_{l=0}^{L-1}\mathbb{E}\left\{|h_l|^4\right\}\left|S_{k-m}(\varepsilon)e^{-j\frac{2\pi}{N}(k-m)l} + S_{m-k}(\varepsilon+\Delta\varepsilon)e^{j\frac{2\pi}{N}(k-m)l}\right|^2.
\end{aligned}$$

Thus, $\mathrm{CIR}_{\mathrm{MCVT}}$ in (6.19) can be obtained.

6.3.5 MCJT

When the conjugate operation is adopted, we obtain the MCJT scheme. In this case, the two consecutive transmitted OFDM symbols are given by $\overline{X}^{(1)} = [X_0, X_1, \ldots, X_{N-1}]$ and $\overline{X}^{(2)} = \left[X_0^*, X_{N-1}^*, \ldots, X_1^*\right]$. According to (6.6), the decision variable at the mth ($m \in \{0, 1, \cdots, N-1\}$) subcarrier is given by

$$\begin{aligned}
\widehat{X}_m &= H_m^*\overline{Y}_m^{(1)} + H_{N-m}\overline{Y}_{N-m}^{(2)*} \\
&= \left[S_0(\varepsilon)\left|H_m\right|^2 + S_0^*(\varepsilon+\Delta\varepsilon)\left|H_{N-m}\right|^2\right]X_m \\
&+ \sum_{k=0,k\neq m}^{N-1}\left[S_{k-m}(\varepsilon)H_m^*H_k + S_{m-k}^*(\varepsilon+\Delta\varepsilon)H_{N-m}H_{N-k}^*\right]X_k \\
&+ H_m^*W_m^{(1)} + H_{N-m}W_{N-m}^{(2)*}.
\end{aligned} \tag{6.21}$$

According to (6.21), the CIR of the MCVT scheme can be expressed as

$$\mathrm{CIR}_{\mathrm{MCJT}} = \frac{\mathbb{E}\left\{\left|S_0(\varepsilon)\left|H_m\right|^2 + S_0^*(\varepsilon+\Delta\varepsilon)\left|H_{N-m}\right|^2\right|^2\right\}}{\sum_{k=0,k\neq m}^{N-1}\mathbb{E}\left\{\left|S_{k-m}(\varepsilon)H_m^*H_k + S_{m-k}^*(\varepsilon+\Delta\varepsilon)H_{N-m}H_{N-k}^*\right|^2\right\}}. \tag{6.22}$$

For the multipath Rayleigh fading channels, the CIR of the MCJT scheme is given by

$$\mathrm{CIR}_{\mathrm{MCJT}} = \frac{\left|S_0(\varepsilon) + S_0^*(\varepsilon+\Delta\varepsilon)\right|^2}{\sum_{k=1}^{N-1}\left|S_k(\varepsilon) + S_{-k}^*(\varepsilon+\Delta\varepsilon)\right|^2}, \tag{6.23}$$

which is derived in Sect. 6.3.5.1. Also, it is worth noting that the CIR of the MCJT scheme is not affected by the channel length L.

Similarly to MCSR, we see here that the denominator in the CIR expression is the summation over $S_k(\varepsilon) + S_{-k}^*(\varepsilon+\Delta\varepsilon)$, which is approximately zero for $k \neq 0$ and small $\Delta\varepsilon$. In addition, by comparing with (6.14), it can be found $\mathrm{CIR}_{\mathrm{MCJT}} \approx \mathrm{CIR}_{\mathrm{MCSR}}$ when $\Delta\varepsilon = 0$.

Finally, it is worth noting that in flat fading channels, the CFRs at all subcarriers are the same, and the CFR coefficients are inherently cancelled in the CIR expression. Thus, the CIR of each scheme, namely, (6.9), (6.11), (6.14), (6.20), and (6.23), has exactly the same expression as that in AWGN channels.

6.3.5.1 Derivation of CIR of MCJT

It can be readily derived that

$$S_0(\varepsilon)\left|H_m\right|^2 + S_0^*(\varepsilon+\Delta\varepsilon)\left|H_{N-m}^2\right| = \sum_{a=0}^{L-1}\sum_{b=0}^{L-1} h_a h_b^* \left[S_0(\varepsilon)e^{-j\frac{2\pi}{N}(a-b)m} + S_0^*(\varepsilon+\Delta\varepsilon)e^{j\frac{2\pi}{N}(a-b)m}\right]$$

and

$$\begin{aligned}\left|S_0(\varepsilon)\left|H_m\right|^2 + S_0^*(\varepsilon+\Delta\varepsilon)\left|H_{N-m}^2\right|\right|^2 = &\sum_{a=0}^{L-1}\sum_{b=0}^{L-1}\sum_{c=0}^{L-1}\sum_{d=0}^{L-1} h_a h_b^* h_c^* h_d \\ &\times \left[S_0(\varepsilon)e^{-j\frac{2\pi}{N}(a-b)m} + S_0^*(\varepsilon+\Delta\varepsilon)e^{j\frac{2\pi}{N}(a-b)m}\right] \\ &\times \left[S_0^*(\varepsilon)e^{j\frac{2\pi}{N}(c-d)m} + S_0(\varepsilon+\Delta\varepsilon)e^{-j\frac{2\pi}{N}(c-d)m}\right].\end{aligned}$$

Thus, for the multipath Rayleigh fading channels, we have

$$\mathbb{E}\left\{(S_0(\varepsilon)\left|H_m\right|^2 + S_0^*(\varepsilon+\Delta\varepsilon)\left|H_{N-m}^2\right|)^2\right\} = \left|S_0(\varepsilon) + S_0^*(\varepsilon+\Delta\varepsilon)\right|^2 \sum_{l=0}^{L-1}\mathbb{E}\left\{\left|h_l\right|^4\right\}.$$

In a similar way,

$$\begin{aligned} & S_{k-m}(\varepsilon)H_m^*H_k + S_{m-k}^*(\varepsilon+\Delta\varepsilon)H_{N-m}H_{N-k}^* \\ &= \sum_{a=0}^{L-1}\sum_{b=0}^{L-1} e^{-j\frac{2\pi}{N}(kb-ma)}(S_{k-m}(\varepsilon)h_a^*h_b + S_{m-k}^*(\varepsilon+\Delta\varepsilon)h_ah_b^*) \end{aligned}$$

and

$$\begin{aligned} \left|S_{k-m}(\varepsilon)H_m^*H_k+S_{m-k}^*(\varepsilon+\Delta\varepsilon)H_{N-m}H_{N-k}^*\right|^2 = & \sum_{a=0}^{L-1}\sum_{b=0}^{L-1}\sum_{c=0}^{L-1}\sum_{d=0}^{L-1} e^{-j\frac{2\pi}{N}[(kb-ma)-(kd-mc)]} \\ & \times (S_{k-m}(\varepsilon)h_a^*h_b+S_{m-k}^*(\varepsilon+\Delta\varepsilon)h_ah_b^*) \\ & \times (S_{k-m}^*(\varepsilon)h_ch_d^*+S_{m-k}(\varepsilon+\Delta\varepsilon)h_c^*h_d). \end{aligned}$$

For the multipath Rayleigh fading channels, we have

$$\mathbb{E}\left\{\left|S_{k-m}(\varepsilon)H_m^*H_k+S_{m-k}^*(\varepsilon+\Delta\varepsilon)H_{N-m}H_{N-k}^*\right|^2\right\} = \sum_{l=0}^{L-1}\mathbb{E}\left\{|h_l|^4\right\}\left|S_{k-m}+S_{m-k}^*\right|^2.$$

Accordingly, $\mathrm{CIR}_{\mathrm{MCVT}}$ in (6.23) can be obtained.

6.3.6 CIR Comparison

To compare the CIR performance among the plain OFDM, the adjacent-mapping-based schemes, and the mirror-mapping-based schemes, an OFDM system with $N = 1024$ subcarriers is considered. Figure 6.5 presents the CIR results of flat fading channels, i.e., $L = 1$. For the ICI two-path cancellation schemes, the CIR results with $\Delta\varepsilon = 0$ and $\Delta\varepsilon = 0.03$ are presented. From the figure, the following facts can be observed: (1) All mirror-mapping-based schemes express much better CIR performance than the plain OFDM. (2) MSR and MCSR outperform ASR and ACSR, respectively. This shows that the mirror-mapping rule has better ICI suppression capability than the adjacent-mapping rule. The main reason is that for the mirror-mapping-based schemes, the interference from neighbor subcarriers is sufficiently suppressed, while there is still some residual interference from neighbor subcarriers for the adjacent-mapping-based schemes. (3) With $\Delta\varepsilon = 0$, the CIR curves of the MCSR scheme and the MCJT scheme coincide, and the CIR of the MSR scheme is close to that of the MCVT scheme. This is because the same operation is adopted for both schemes. (4) With $\Delta\varepsilon = 0$, the CIR performance of the conversion-based schemes, namely, MSR and MCVT, is better than that of the conjugate-based schemes, namely, MCSR and MCJT. This is because in their

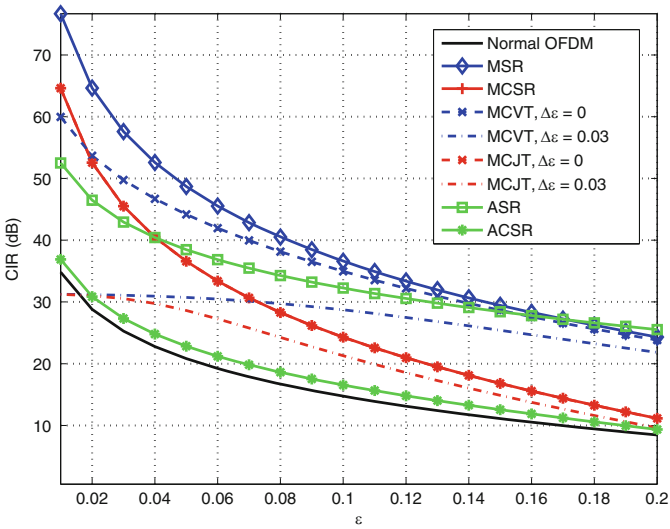

Fig. 6.5 CIR comparison among the plain OFDM, the adjacent-mapping-based schemes, and the mirror-mapping-based schemes for different values of ε over flat fading channels

CIR expressions $S_k + S^*_{-k} \approx 0$ is a rougher approximation than $S_k + S_{-k} \approx 0$. (5) With $\Delta\varepsilon = 0.03$, the CIR performance of the MCVT scheme and the MCJT scheme is degraded due to the CFO deviation between the first OFDM symbol and the second OFDM symbol.

Figures 6.6 and 6.7 present the CIR results of multipath Rayleigh fading channels. Assume each channel tap has the same power, i.e., $\sigma_0^2 = \sigma_1^2 = \cdots = \sigma_{L-1}^2$. The effect of the channel length L is investigated. From the figure, it can be observed that for the multipath Rayleigh fading channels, the mirror-mapping-based schemes have better CIR performance compared with that of the plain OFDM. The CIR performance of the plain OFDM and the conjugate-based schemes, namely, MCSR and MCJT, is not affected by the channel length L. For the conversion-based schemes, namely, MSR and MCVT, the CIR performance is degraded with the channel length L.

In summary, based on the CIR results of flat fading channels and multipath Rayleigh fading channels, we conclude that our proposed mirror-mapping-based schemes can effectively mitigate ICI.

6.4 Sea Experimental Results

Up to now, we have shown theoretically the effectiveness of the mirror-mapping-based schemes in multipath Rayleigh fading channels with simple CFO. In this section, we verify the applicability of our proposed schemes in UWA communications by sea experiments.

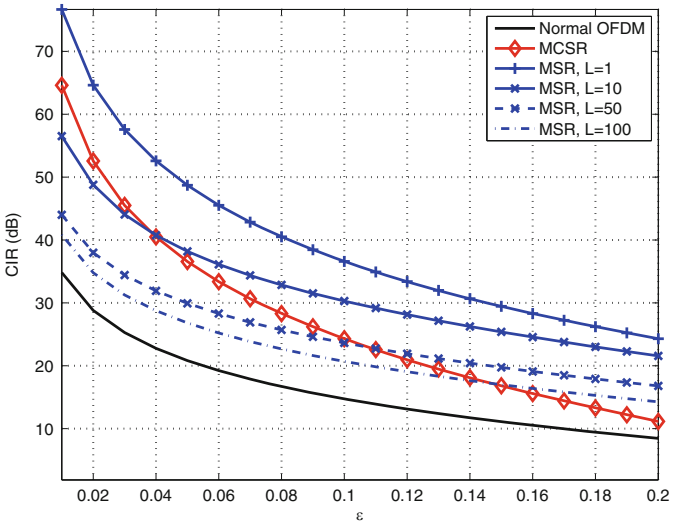

Fig. 6.6 CIR comparison among the plain OFDM, the MSR scheme, and the MCSR scheme for different values of ε over multipath Rayleigh fading channels

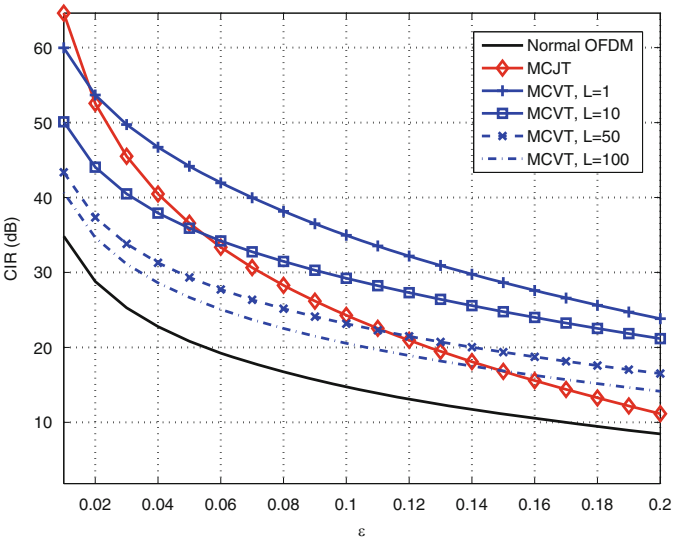

Fig. 6.7 CIR comparison among the plain OFDM, the MCVT scheme, and the MCJT scheme for different values of ε over multipath Rayleigh fading channels

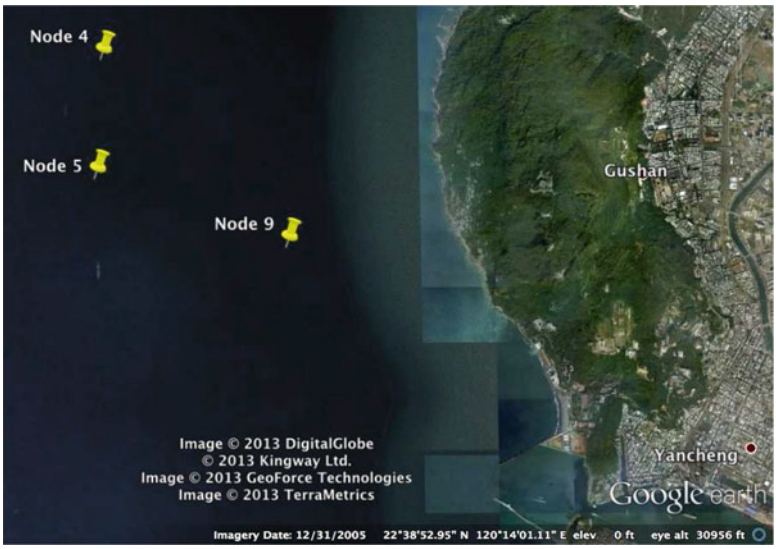

Fig. 6.8 Geographical locations of transceiver nodes. The GPS coordinates of nodes 4, 5, and 9 are (N22.66038, E120.21450), (N22.64844, E120.21405), and (N22.64169, E120.23450), respectively. Their relative distances are 1549.58 m (from node 4 to node 5), 2187.60 m (from node 5 to node 9), and 3377.72 m (from node 9 to node 4)

6.4.1 Experimental Settings

The experiment was conducted in a sea area about 3 km east of Gushan, Taiwan, in May 21–22, 2013, which is illustrated in Fig. 6.8. Three nodes were deployed, i.e., node 4, node 5, and node 9, each of which consisted of one transducer and four hydrophones. The sea depth is around 20 m and the node depth is around 10 m. The transducer and the hydrophones may drift due to waves. During the sea test, the nodes transmitted with each other and the received data packets were recorded.

The basic system parameters are provided in Table 6.1. The bandwidth of the system is 5.36 kHz. The total number of subcarriers is 1600, within which there are 1278 data subcarriers, 214 pilot subcarriers, and 108 null subcarriers. The guard interval has a length of 50 ms, which is much longer than the maximum channel delay spread. The pilot subcarriers are used for channel estimation. For the ICI two-path cancellation schemes, the pilots are uniformly inserted among the data subcarriers. However, for the ICI self-cancellation schemes, to avoid loss of spectral efficiency, the mirror-mapped pilot structure has to be adopted. Thus, the ICI self-cancellation schemes do not facilitate the OFDM system standardization. In addition, QPSK modulation is adopted for the mirror-mapping-based schemes.

To demonstrate the performance of the mirror-mapping-based schemes, there are two benchmark candidates, both of which have the same spectral efficiency as the mirror-mapping-based schemes. The first one is the plain OFDM with BPSK

Table 6.1 System parameters

Sampling rate at the transmitter	48 kHz
Sampling rate at the receiver	48 kHz
Signal bandwidth	5.36 kHz
Carrier frequency	17 kHz
Number of total subcarriers	1600
Number of data subcarriers	1278
Number of pilot subcarriers	214
Number of null subcarriers	108
Subcarrier spacing	3.35 Hz
OFDM symbol duration	299 ms
Guard interval	50 ms
Number of hydrophones	4

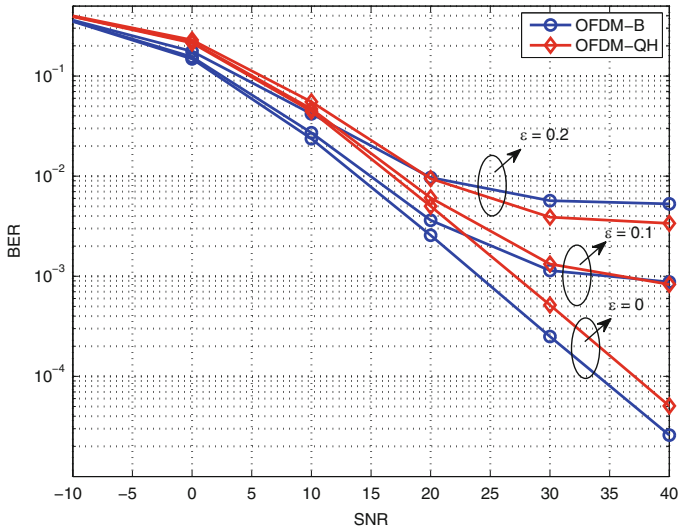

Fig. 6.9 BER performance comparison between OFDM-QH and OFDM-B for CFOs $\varepsilon = 0, 0.1, 0.2$. The total subcarrier number is $N = 1024$, the bandwidth is 6 kHz, and the channel spread length is 9 ms. For OFDM-QH, Gray code is adopted for QPSK modulation

modulation (OFDM-B). The second one is the OFDM scheme with half of total subcarriers occupied by QPSK data symbols and each of data symbols surrounded by two null subcarriers (OFDM-QH). For OFDM-QH, the ICI from direct neighbors is removed. Figure 6.9 compares the BER performance of OFDM-B and OFDM-QH under different CFOs. It is found that OFDM-B has lower BER than OFDM-QH in low-medium SNR range (SNR$<$ 20, BER$>$ 10^{-3}). This is because of the higher symbol detection error for QPSK modulation. Considering high signal attenuation of UWA channels and relatively low SNR at the receive hydrophones, OFDM-B, the one with better BER, is chosen as the benchmark in the sea experiment.

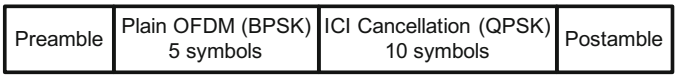

Fig. 6.10 Frame structure

The frame structure for transmission is given in Fig. 6.10. The transmitted frame consists of a preamble, transmitted OFDM data symbols and a postamble. We allocate five OFDM symbols with BPSK modulation for the plain OFDM and ten OFDM symbols with QPSK modulation for either the ICI self-cancellation schemes or the two-path cancellation schemes. Therefore, 17 OFDM symbols are involved in each frame in the experiment. In addition, Gray code is adopted for QPSK modulation. Depending on the ICI cancellation structure at the last ten OFDM symbols, there are four different frames, implementing the MSR scheme, the MCSR scheme, the MCVT scheme, and the MCJT scheme, respectively. In the experiment, ignoring preamble and CP overhead, the data rate of mirror-mapping-based schemes and OFDM-B is 4.27 kbps.

6.4.2 Time Synchronization and Resampling

For time synchronization, the received signal is correlated with the preamble and the postamble to obtain the starting and ending time of the received data frame. Then, the resampling factor is calculated by comparing the received signal length and the transmitted signal length. Finally, to remove the major Doppler effect, the received signal is resampled according to the resampling factor [1].

6.4.3 Channel Estimation

The CFR of each subcarrier can be estimated via the received signals on the pilot subcarriers. The CFRs on the pilot subcarriers are estimated first. Then the CFRs on the data subcarriers can be obtained through the piecewise cubic spline interpolation. To combat the time-varying feature of UWA channels, channel estimation is done for each OFDM symbol.

6.4.4 Experimental Results

To obtain the BER results and enable the fair comparison of different schemes, the packages with indices “M0000043.DAT,” “M0000044.DAT,” “M0000046.DAT,” “M0000047.DAT,” “M0000049.DAT,” “M0000050.DAT,” “M0000052.DAT,” and

Table 6.2 Packet information

Packet index	Scheme	Effective SNR	Transmit time	T-R Pair
M0000043.DAT	MCJT	12.47	18:16:00 05/21/13	N5-N9
M0000044.DAT	MCJT	12.55	18:16:25 05/21/13	N5-N9
M0000046.DAT	MCSR	12.27	18:16:55 05/21/13	N5-N9
M0000047.DAT	MCSR	12.15	18:17:21 05/21/13	N5-N9
M0000049.DAT	MSR	12.21	18:17:51 05/21/13	N5-N9
M0000050.DAT	MSR	12.29	18:18:16 05/21/13	N5-N9
M0000052.DAT	MCVT	12.31	18:18:46 05/21/13	N5-N9
M0000053.DAT	MCVT	12.36	18:19:11 05/21/13	N5-N9

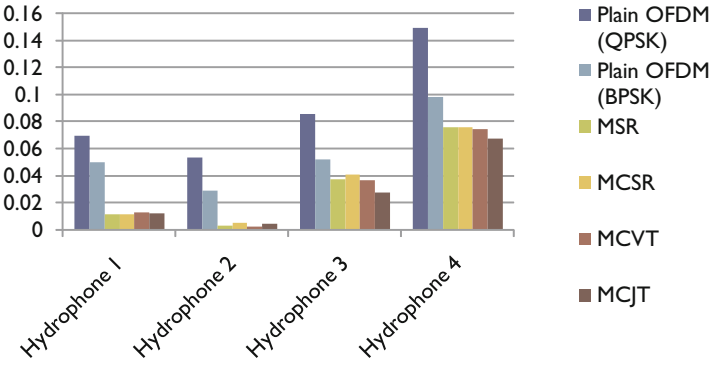

Fig. 6.11 BER performance of the plain OFDM and the mirror-mapping-based schemes. For each hydrophone, the *bars* from left to right represent the OFDM-Q scheme, the OFDM-B scheme, the MSR scheme, the MCSR scheme, the MCVT scheme, and the MCJT scheme, respectively

"M0000053.DAT" are utilized with their information provided in Table 6.2. They are transmitted consecutively with similar receive SNR levels and through the same transmitter-receiver (T-R) pair. Figure 6.11 illustrates the BER performance of OFDM-B, the mirror-mapping-based ICI cancellation schemes, and the plain OFDM with QPSK modulation (OFDM-Q). The BER of OFDM-Q is calculated by means of directly decoding the mirror-mapping-based schemes without combining data subcarrier pairs, and thus ICI is not suppressed. As expected, all mirror-mapping-based schemes have lower BER than OFDM-B and OFDM-Q for all hydrophones. This confirms that the mirror-mapping-based schemes can achieve superior ICI mitigation in OFDM UWA communications.

6.5 Summary

In this chapter, to mitigate the detrimental effect of ICI in OFDM UWA communications, we have proposed four effective low-complexity mirror-mapping-based ICI cancellation schemes without explicitly estimating ICI coefficients or CFO and

derived their CIRs in multipath Rayleigh fading channels. From the theoretical analyses and numerical results, it has been revealed that the mirror-mapping-based schemes outperform the plain OFDM and the adjacent-mapping-based schemes. By comparing the ICI self-cancellation schemes and the ICI two-path cancellation schemes, the ICI self-cancellation schemes, namely, MSR and MCSR, are robust against the CFO deviation between the first OFDM symbol and the second OFDM symbol. However, they require the mirror-mapped pilot structure, which does not facilitate the OFDM system standardization. In addition, compared with the conjugate-based schemes, the conversion-based schemes, namely, MSR and MCVT, have better CIR performance. However, their CIR performance degraded for multipath Rayleigh fading channels with large channel length. Thus, the scheme selection depends on the actual system requirement and channel conditions. Finally, all mirror-mapping-based schemes have been tested in a recent sea experiment conducted in Taiwan in May 2013. Decoding results have shown that the proposed mirror-mapping-based schemes provide much lower BER than the plain OFDM. This confirms that the mirror-mapping-based schemes are very effective for ICI mitigation in OFDM UWA communications.

References

1. B. Li, S. Zhou, M. Stojanovic, L. Freitag, P. Willett, Multicarrier communication over underwater acoustic channels with nonuniform Doppler shifts. IEEE J. Ocean. Eng. **33**(2), 198–209 (2008)
2. P.H. Moose, A technique for orthogonal frequency division multiplexing frequency offset correction. IEEE Trans. Commun. **42**(10), 2908–2914 (1994)
3. Y. Zhao, S.-G. Haggman, Intercarrier interference self-cancellation scheme for OFDM mobile communication systems. IEEE Trans. Commun. **49**(7), 1185–1191 (2001)
4. J. Lee, H.-L. Lou, D. Toumpakaris, J.M. Cioffi, SNR analysis of OFDM systems in the presence of carrier frequency offset for fading channels. IEEE Trans. Wirel. Commun. **5**(12), 3360–3364 (2006)

Chapter 7
Conclusions and Future Directions

7.1 Conclusions

In this monograph, we designed the energy-efficient and reliable dual-hop RA-UAC protocols from three aspects, namely, power allocation, decomposed fountain codes design, and packet transmission reliability.

First, we investigated the power allocation issues in two scenarios, namely, short-range RA-UAC and medium-long-range RA-UAC. For the short-range RA-UAC, the source and the relay compute their optimal power allocation and distribution over all OFDM subcarriers based on received CSI feedback. Channel prediction is implemented at the receiving nodes to compensate the channel variation during the feedback signal propagation. Due to the band-limited feature of UAC channels, the Lloyd quantizer is used to quantize CSI efficiently. For the medium-long-range RA-UAC, due to the overlong propagation delay, CSI feedback could be nullified even if Doppler compensation and channel prediction are implemented at the receiving nodes. Under this circumstance, statistical CSI can be utilized when calculating the power allocation between the source and the relay(s). According to the power allocation results, we proposed a practical asynchronous relay selection protocol to let the relay with the best channel condition statistically transmit, while other relays keep silent. To avoid links interference, the asynchronous transmission was carefully designed such that the DL signal and the RL signal arrive at the destination at different time periods, and MRC is implemented at the destination to collect delay diversity. It has been verified that both of the short-range adaptive RA-UAC system and the long-range RA-UAC system with selective relaying outperform the traditional RA-UAC system with the uniform power allocation.

Secondly, we designed a new type of hybrid DLT codes for dual-hop RA-UAC to improve energy efficiency and accuracy. To facilitate codes construction, a novel nonnegative polynomial decomposition algorithm was proposed for better accuracy and simpler implementation. Then the encoding and distribution decomposition schemes for the new type of h-DLT codes, i.e., h-DLT II codes, were presented.

X. Cheng et al., *Cooperative OFDM Underwater Acoustic Communications*,
Wireless Networks, DOI 10.1007/978-3-319-33207-9_7

Numerical results show that the h-DLT II codes achieve similar performance as the primitive LT codes, and simulations reveal that the h-DLT II codes assisted cooperative communications scheme outperforms the original h-DLT codes assisted cooperative communications scheme with much smaller communication cost.

Finally, to ensure the packet transmission reliability in RA-UAC, we proposed four effective low-complexity mirror-mapping-based ICI cancellation schemes to suppress the ICI power level caused by the Doppler effect in UWA channels. All mirror-mapping-based schemes have been tested in a recent sea experiment conducted in Taiwan in May 2013. Decoding results have shown that the proposed mirror-mapping-based schemes provide much lower BER than the plain OFDM under the same spectral efficiency. This confirms that the mirror-mapping-based schemes are more reliable than the plain OFDM in UAC.

7.2 Future Directions

In this monograph, we mainly studied three techniques in dual-hop RA-UAC to improve its reliability and energy-efficiency. However, their potential in UWASNs has not been fully explored. There are still many open problems regarding their applications to UWASN.

First, only the dual-hop RA-UAC is considered, where there exists only one source, one destination, and one/multiple relay(s). However, in UWASN, multi-hop communications is more common and general. The techniques such as power allocation calculation, the adaptive system design, etc. have to be reinvestigated when applying these techniques to the general scenario.

Secondly, the hybrid DLT codes in the multi-user system are worth investigating, where the relay could receive multiple packets from different sources and transmit encoded packets to the destination. For this scenario, it is interesting to investigate the DDP design, the storage scheme, and TDMA transmission scheduling between the sources and the relay.

Thirdly, we only consider single transmitting/receiving antenna at all nodes. Multiple-input multiple-output (MIMO) techniques allow multiple data streams to coexist over the band-limited UWA channels. Integrating MIMO techniques into RA-UAC could boost the data rate. Some research problems brought by MIMO techniques include the power allocation and the adaptive system design in MIMO-based RA-UAC. In addition, the mirror-mapping-based ICI cancellation techniques are promising in MIMO systems. This is because for MIMO systems, each data stream has different Doppler shifts. Explicitly compensating Doppler shifts or estimating ICI coefficients all together is difficult. The mirror-mapping-based ICI cancellation techniques can suppress the ICI power level caused by each Doppler shift all together implicitly. Therefore, it has the potential to combat the Doppler effect in MIMO UAC effectively with the low receiver complexity.